Winter 3-3-2018

Engineering Tools to Further Neuroscientific Investigation

Jessica L. Scoggin

ENGINEERING TOOLS TO FURTHER NEUROSCIENTIFIC INVESTIGATION

by

Jessica LeeAnn Scoggin, B.L.S., M.S.

A Dissertation Presented in Partial Fulfillment

Of the Requirements of the Degree

Doctor of Philosophy

COLLEGE OF ENGINEERING AND SCIENCE

LOUISIANA TECH UNIVERSITY

March 2018

Gsform13a

ABSTRACT

Custom equipment is often necessary in the laboratory. However, costs for such equipment can be high and efficient systems with lower cost are an advantage. In this work, we showed that a cellular environment to keep cells healthy and viable for five hours on a microscope could be created using FDM printing (Chapter 3). Design criteria were that it maintained correct temperature, high humidity and proper pH to control the environment as discussed in Chapter 2. Results indicated that cells would maintain viability for up to five hours, but redesigns needed to be made for extending viability past five hours.

An imaging enhancement termed PICS (Planar Imaging of Curved Surfaces) was also introduced (Chapter 5). For this project, design criteria were that the device stabilized the tissue for imaging while allowing fluid flow around the tissue and facilitate rotation of the naturally curved tissue with respect to the microscope objective lens. Three further considerations of the PICS device were: (1) that it should not add undue shear stresses to the sample tissue, (2) that there should be no unintentional translation, (3) that it should attach to a standard microscope temperature controller in such a way that it does not interfere with temperature controls and does not move unintentionally. Results indicate successful movement of tissue with respect to imaging plane to facilitate productive image capture.

Finally, in Chapter 7, a microelectrochemical array was used to explore differences between glioma and normal astrocyte glutamate levels. Results showed that

glioma and normal astrocyte glutamate uptake can be tracked in real-time and compared using the probe. The distinction between glioma cells and astrocytes relies on three indicators: (1) a signal more stepped like in appearance, closer to that of a calibration curve, coming to a steady baseline faster and having a shorter FDHM, is a first indication of impaired uptake; (2) a signal showing a lower k constant, indicating a slower overall clearance rate, (3) faster rise times corresponding with a slower maximum elimination rate. These corresponding factors together indicate impaired uptake in glioma cells versus normal astrocyte glutamate uptake.

approval for scholarly dissemination here

DEDICATION

This work would not have been possible without the support of my parents, my husband, and God, who has always seen me through.

TABLE OF CONTENTS

LIST OF TABLES

LIST OF FIGURES

ACKNOWLEDGEMENTS

Thanks to Vladislav Voziyanov for use of his TRIO system design, which is the base design for the Stage-Top incubator of Chapter 3. Further thanks according to that project goes to Louisiana Tech University for the use of their MakerBot® 3D printers. The Louisiana Tech Thingery provided printing pedagogy for that project, and François Decuir taught me how to take apart and put back together MakerBots®.

Thanks to Daniel Rivera for his initial work on the PICS design found in Chapter 5. Dr. Francis Szele also brought the curved imaging impediment to our attention, encouraging us to work on that project.

Special thanks goes to the Center for Biomedical Engineering and Rehabilitation Sciences and NeuroNEM for their support of these projects.

CHAPTER 1

INTRODUCTION

In April of 2013, President Barack Obama announced the BRAIN (Brain Research through Advancing Innovative Neurotechnologies) Initiative [1]. This 21st century "Grand Challenge" was designed to put federal and private monies into research laboratories studying the brain in order to "Develop new technologies to explore how the brain's cells and circuits interact at the speed of thought," with one of the key goals being to advance the development and application of new neurotechnologies [2].

In agreement with this initiative, The National Academy of Engineering also issued 14 Grand Challenges for Engineering in the 21st century, including the challenges: "Reverse Engineer the Brain" and "Engineer the Tools of Scientific Discovery" [3]. These challenges call for engineers, seen as the driving force to advance civilization, to pursue solutions to problems that affect "all society's members." Specifically listed in the 14th Grand Challenge was "new biochemical methods of probing the body's cellular and molecular machinations" [3].

Both of these events express, at the highest levels of national sentiment, the need for increased knowledge in neuroscientific study and the desire to be able to accomplish it through new machinery and mechanisms that expand our current toolboxes. Presented in this cumulative work are a few methods designed to address some small parts of this much larger whole. Tools for neuroscientific research advancement have been designed

and developed using models incorporating *in vitro* neuro-culture and *ex vivo* neuro-explants.

A total of three projects overseeing three distinct devices are presented. Chapter 3 explores a 3D-printed stage-top incubation device to advance common scientific community laboratory equipment. Chapter 5 examines a planar imaging enhancement device for curved surfaces, PICS, designed to explore the cytoarchitecture of the subventricular zone. Finally, Chapter 7 details analysis of an electrochemical probe for monitoring glutamate levels in real time.

While each chapter focuses on the aspects of the project, the preceding chapter incorporates a review of knowledge necessary for understanding the details of that project. Thus, Chapter 2 reviews additive manufacturing and cell culture environment requirements as prerequisite knowledge for the stage-top incubator found in Chapter 3. Chapter 4 reviews stem cell knowledge for Chapter 5. Additionally, Chapter 6 reviews glutamate transport kinetics and microelectrode advancement for Chapter 7.

The common thread through each of these projects is the operational performance and analysis of newly engineered tools. The first two tools presented are designed from conception and emphasize creative solutions to common problems associated with research. The final chapters cover a commercialized tool that has been applied to probing biochemical signals in brain cells. Though each of these projects use different sets of neural tissue for testing, overall, facilitating neuroscientific research advancement through new tool development can be seen as the clear goal.

The first tool addressed in Chapters 2 and 3 comes from the in house need of our own laboratory. We asked the question, “Can we develop a low-cost and efficient *in vitro*

incubation device for our research aims?" Though there are already commercial stage-top incubators on the market, the cost of a commercial stage-top incubator was beyond the resources we had available for a project, as it was a preliminary study. We also believed the question had relevant implications for the overall scientific community.

As 3D printing machines have grown in popularity, their use in the laboratory has also grown. So much so that the NIH (National Institutes of Health) now has an open-source website dedicated to sharing printable models, called the NIH 3D Print Exchange [4]. It was believed that if we could answer this question and that a stage-top incubation device could be printed, then it could be made available through the NIH 3D Print Exchange and become useful to researchers who also needed such a device.

Through Chapter 3, we will show that a low-cost, custom made *in vitro* stage-top incubator for studies up to five hours is possible using a FDM™ printing machine. New and useful laboratory equipment such as this one can be created and collaboratively shared with the scientific community on open source websites like the NIH 3D Print Exchange.

The second research need, addressed in Chapters 4 and 5, came out of a collaborative laboratory. Their desire was for a device which would make imaging their curved sample easier. They asked us "How to hold a sample to enable quick repositioning of a curved tissue sample for the best imaging results?" Live images of three-dimensional tissue can be difficult to acquire, especially in high resolution over a large field of view. Details of such tissues, like lateral ventricular wall wholemounts, are necessary to study cytoarchitecture of areas in the brain, as well the dynamics of other

tissues. The design of the planar imaging of curved surfaces (PICS) device allows for more efficient imaging of such tissue.

Finally, as discussed in Chapters 6 and 7, glutamate, which is the most prominent excitatory neurotransmitter in the mammalian CNS, is detected with the use of a manually coated R1 probe from CenMeT. Real time detection of glutamate in neural tissues is advantageous for advancement of glutamate dynamics in systems. This neurotransmitter is relevant to research on brain disorders such as epilepsy due to its excitotoxicity in high concentrations.

CHAPTER 2

REVIEW OF ADDITIVE MANUFACTURING AND CULTURE ENVIRONMENT REQUIREMENTS

2.1 *In Vitro* and *Ex Vivo* Environment Needs

As it stands, cell culture cannot fully replicate the *in vivo* environment, meaning that cells and tissue must adapt to artificial conditions when they are extracted from the original organism, or they die. Cell viability depends on several factors: temperature, physiological salt solution content, osmotic pressure, pH, gas concentrations, and humidity. These factors are all controlled in the *in vitro* and *ex vivo* environment in order to replicate as many *in vivo* conditions as practical, keeping cells and tissue alive longer for study.

Most of the above factors can be controlled by correct use of cell media. That is, salt solution content, growth factors, nutrients, hormones, osmotic pressure and pH are all dependent on the media. Since necessary conditions differ between cell types, the choice of media for that cell line is very important, and often relies on work done in previous labs with that cell type.

Though correct pH is formulated in media content, pH and gas concentrations go hand in hand, as pH increases without proper O_2/CO_2 concentration. This relationship is the consequence of sodium bicarbonate ($NaHCO_3$) buffer found in most media. $NaHCO_3$ raises the pH of liquids and is often used to that end in pools and spas. In media, sodium

bicarbonate breaks down into Na^+, H_2CO_3 (carbonic acid), and HO^- [5]. Since the carbonic acid is in chemical equilibrium with CO_2 in aqueous solutions, gaseous CO_2 can be added to the surrounding air to maintain equilibrium. This prevents dissociation of carbonic acid into the bicarbonate and carbonate ions, which cause the rise in pH. The typical pH is 7.4 for mammalian cell line growth [6], and most media is buffered for a pH range of 7.0-7.7 [5].

Mammalian cells survive best in the temperature range of their host's body temperature, typically 36-37˚C [6]. Though they can survive in slightly higher temperatures, manuals state that overheating is more of an issue than underheating, so it is better to be slightly under 37˚C than over on average. Reports also suggest that mildly hypothermic cultures, typically in the range of 30-33˚C, can be used to increase specific productivity of recombinant proteins, although they slow growth rate [7].

Maintaining a high humidity is also important for cell culture environments. Since most incubators are open systems, the cultures are in ambient, heated air. If the vapor pressure of ambient air is lower than that of the media, evaporation occurs, causing an imbalance of the osmotic pressure kept by the media. Imbalances in osmotic pressure cause both a slower growth rate, possible toxicity, and accelerated death phase in cells [8]. Thus, humidity is kept within the range of 85-95% for most incubation systems, normally achieved through a pan of water placed in the incubator.

Keeping cells healthy and viable in an *in vitro* or *ex vivo* environment is necessary to perform any experiment using these models. Though correct use of media controls many aspects of cell culture needs, other environmental factors that need to be carefully

controlled are temperature, humidity, and pH. Any attempt to create a cell model environment should rely heavily on maintaining and regulating these factors.

Chapter 3 will detail how we created a cellular environment to keep cells healthy and viable for five hours on a microscope. Design criteria were that it maintained correct temperature, high humidity and proper pH to control the environment as discussed here. To do this, we used 3D printing technology.

2.2 Rapid Prototyping Technology

First developed in the 1980s, rapid prototyping (RP) is the original name for techniques that create a custom system, part, or part representation in a quick manner before commercialization. RP development is closely tied to the development of computer-aided design (CAD) [9] as RP systems use CAD software for modelling and code fabrication. Over time, as RP systems developed and the technology grew, the term became almost synonymous with systems using additive manufacturing, even though this was not the original meaning. Additive manufacturing (AM) is the process of creating an object through a layer-by-layer approach; that is, each object is divided into many "thin cross-section[s] of the part derived from the original CAD data" [10] with cross-sections, or layers, manufactured one at a time and built onto each other.

Today, AM is the recognized term for what used to be RP [11], since the scope of products created by these systems goes beyond prototyping with intent at later commercialization [9], [10]. However, the popular name for AM remains 3D printing, which is indicative of the wide spread use of home-based hobbyist machines rather than the broad range of technologies that collectively make up AM. The seven general categories of technologies include: "binder jetting, material jetting, direct energy

deposition, sheet laminations, material extrusion, powder bed fusion, and vat photo-polymerization" [12]. The two types of AM described in this work are material extrusion, used in Chapters 3 and 4, and vat photopolymerization, or stereolithography, mentioned briefly in Chapter 4. For this reason, extrusion-based AM and RP will be the main focus of this chapter.

2.2.1 Extrusion-based Systems

Material extrusion systems are the most popular of the AM systems because they are easy to use and can be inexpensive. Thus, their existence in domestic and hobbyist settings is becoming more commonplace worldwide. Fuse deposition modelling (FDM) is the original term trademarked by Stratasys Inc. when these systems first became commercially available in the early 90s. FDM™ was originally designed by S. Scot Crump, who later founded and became CEO of Stratasys, Inc. FDM™ is also known as FFF, or fused filament fabrication, an acronym introduced by the RepRap Project, to describe FDM™ to its followers since FDM™ was trademarked by Stratasys.

RepRap, short for replicating rapid-prototyper [13], also advanced the popularity of FDM™ since its concept was to use a FDM™ system to "print a copy" or "print itself." That is, an original printing system creates most of the parts needed to build another FDM™ printing system. This greatly reduced the price of FDM™ systems at the time. Since its inception in 2004, RepRap has also adhered to a policy of open source software, a series of software guidelines written by Bruce Perens in the late 1990s. Their open source license, the GNU General Public License, allows the RepRap community to access necessary printing software at "no cost" [13]. Figure 2-1, reprinted from the RepRap site [14], describes the FDM™ process.

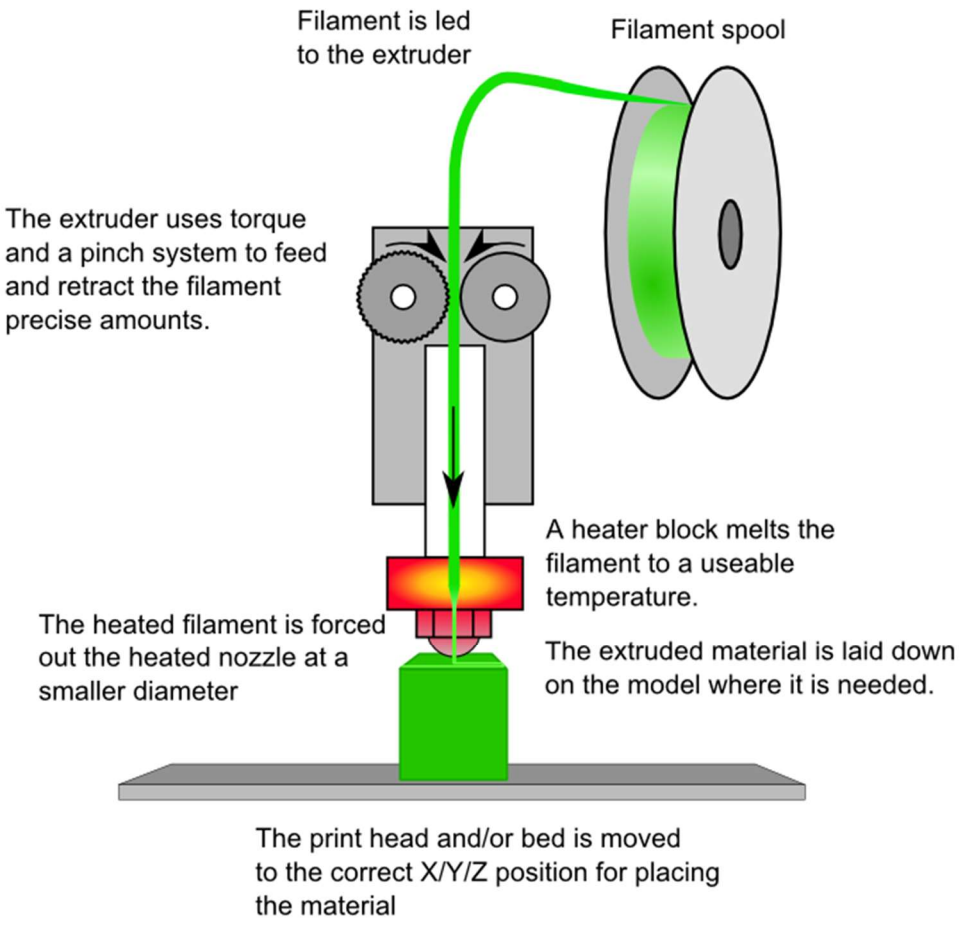

Figure 2-1: Description of FDM™, or FFF, reprinted from http://reprap.org/wiki/File:FFF.png [14].

As Figure 2-1 depicts, FDM™ works by feeding the material, also called filament since it is usually spooled and thread-like, into a thermally controlled nozzle at constant pressure and speed. Common 3D printing materials consist of thermoplastics, plastics that melt at a certain temperature then harden when brought back to room temperature.

Thermoplastics are advantageous in that they can be reheated and reshaped repeatedly. This allows companies to melt large quantities of polymer into the threads known as filaments which can then be re-melted and formed into the desired 3D printed product. If a printed product does not adhere to desired outcomes, failed prints can also

then be re-melted, remade into filament with the proper tools, and reprinted, allowing for a recyclable creation.

Common thermoplastics used in FDM™ are acrylonitrile butadiene styrene (ABS) and polylactic acid (PLA), making up 70% of the 3D printing market in 2015 [15]. ABS is an oil-based polymer, mixed using differing proportions of acrylonitrile, butadiene, and styrene to enhance desired properties such as gloss, hardness, toughness, and resistance. Applications range from "commodity plastics to higher performance engineering thermoplastics" [16], which makes ABS the "largest selling engineering thermoplastic" [16]. ABS is the FDM™ material of choice for structural integrity, although printing requires a heated bed due to its tendency to warp upon rapid cooling.

PLA is a plant-derived synthetic polymer produced through carbohydrate fermentation, mostly obtained from corn or sugar cane [17]. It is biodegradable, bioabsorbable, and biocompatible, resulting in its use in many biomedical applications, such as plates and screws for bone fracture [18]–[20]. PLA is also extremely easy to print with using FDM™ [21], making it a favorite material among hobbyists.

2.2.2 Creating a 3D Printable Object

Creating a custom 3D printable part is a five-step process. First, an object, or model, is created using a CAD program. Depending on the CAD program, tests can be run on the model to ensure its ability to fit the intended design. Running such tests before production is important so that time and materials are not wasted when moving forward in constructing the object.

Once the model is complete and desired tests are run for optimization of performance, the model is then saved as an STL, or stereolithography, file. The STL file

format was established in 1987, specifically to move data from CAD programs to stereolithography machines for 3D Systems, Inc., the first stereolithography, also known as resin printing, business in the United States. The STL file defines the model surface into a series of corresponding triangles, allowing for the model to be encoded as a polyhedron, which forms a 3D volume. Size and shape of the polyhedron (model) does not matter as long as it is fully enclosed, that is all triangle ends connect and two of each individual triangle's vertices are connected to its neighboring triangle.

Once encoded as an STL file, the model can then be put into a slicer program, which produces thin, horizontal layers in the Z plane, or "slices," of the polyhedron. Figure 2-2 is an example of how a slicer program slices an object. Thinner slices are preferable for fine definition. The two-centimeter slices in Figure 2-2 are large producing less definition around the nose, chin, and finely curved areas.

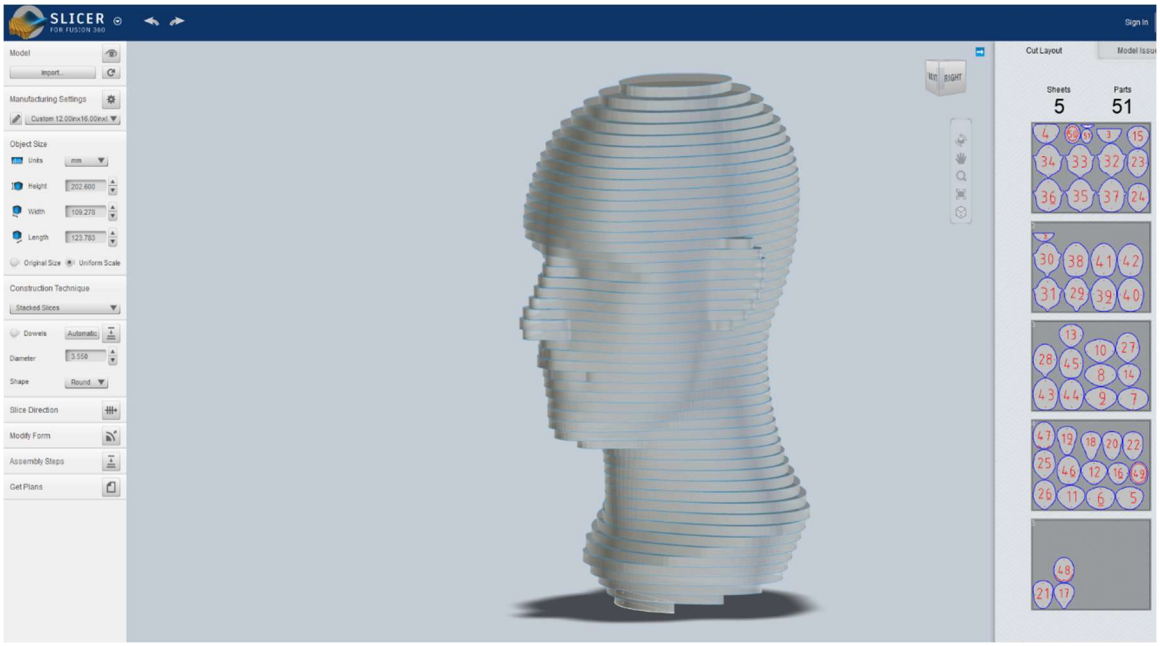

Figure 2-2: Example Sliced Object. Slicer for Fusion 360; right panel consists of numbered slices.

After the object has been sliced, the encoded information can then be passed to the 3D printer, which prints the object using the additive layer by layer process previously mentioned. Though this sounds very simple, there are many minor techniques that can add to or subtract from the quality of a 3D printed part. For instance, material heating temperatures may vary from printer to printer, producing better products at either the mid or higher end of that material's melting range. Thus, it is important to realize extra time may be spent in optimizing the process while learning a printer, material, or shape's individual peculiarities.

Common techniques to ensure proper print structure are using rafts and supports. A raft is a two to three-layer horizontal plane printed from the same material as the desired object at the bottom of the print. This layer is used because the majority of failures occur within the first couple layers of printing due to improper adherence to the print bed, an unleveled print bed, or warping of the printed part. A raft is also built slightly larger than the print. This gives a structure to the print that is more easily detachable from the print bed.

The quality of many curved or branching objects depends on supports. Supports are printed structures designed to enable or "support" sites of desired configuration where strings of filament across a wide-open space would fall, causing the print to fail. Supports are also designed to easily break away from the desired structure so that they do not become undesirable additions to the object. However, supports made of the same material as the print do not always break away easily, so it is suggested either to use a dissolvable support filament or fine-tooth pliers and sand paper to remove them. If the designer is

unsure when to use rafts or supports, it is better to enable this feature in the slicing software which will add supports where needed.

Finally, mechanical or chemical finishing steps are typically needed once the object has been printed. Mechanical finishing may include removing extra supports or a raft, sanding the print in areas, or cutting parts that may not have printed at exact margins. Chemical finishing may include using cyanoacrylate, or super glue, to connect parts. Dissolution in d-Limonene may be necessary if working with a dissolvable support filament, such as High Impact Polystyrene (HIPS).

When the prototype has been finished, it is ready to be tested. If tests do not meet expectations, either further finishing steps or a redesign of the part may be required. A redesign of the original model begins back in the CAD program and follows through necessary prototyping steps again. While this takes additional time, the material costs are usually minimal.

CHAPTER 3

THREE-DIMENSIONAL ADDITIVE PRINTING FOR MANUFACTURING CUSTOM STAGE-TOP INCUBATORS

Three-dimensional printing has become a useful tool for the laboratory, where engineers and scientists can create much needed small prototype parts. Useful items like replacement parts for research equipment can also be made using existing designs [1,2,3]. With many common laboratory tools such as pipettors or mini centrifuges being created for availability in open source websites like Thingiverse or the NIH 3D Print Exchange, new and useful laboratory equipment can be created and collaboratively shared with the scientific community.

Design of a part or prototype from scratch involves creating the object in a 3D CAD program, such as SolidWorks®, putting the file into a slicer program, loading filament into the printer, and some mechanical and/or chemical finishing steps. Design revisions are often required, but printing takes comparatively little time, usually less than a day. Thus, from conception to finish, parts can be made quickly in comparison to molding or machining.

Maintaining healthy cells *in vitro* is dependent upon a stable environment. The common laboratory incubator maintains temperature, humidity, and gas concentrations

relevant to keeping pH balance. Often, cells are grown for live cell imaging of dynamic processes, also called *in vitro* imaging. As *in vitro* imaging experiments lengthen, cells become unstable, exhibit different characteristics or morphology, alter their function, and die without the proper conditions. Thus, stage-top incubators are necessary for experiments using long-term imaging. Yet, most of these are large and/or expensive.

Long-term cell experiments can range from two hours to over 24 hours, depending on the experiment [2]. For our purposes, a stage-top incubator was required for experiments that would last up to five hours on the microscope. To reduce the size of the incubator and keep the cost of the system low, a home-built system was designed with parts produced on a 3D printer. This system is described here.

3.1 Stage-Top Incubator Design

3.1.1 Original Design

The design for the cell culture dish warming system came from an existing animal warming device constructed in our laboratory [22]. The original device, also produced using 3D printing, allows pumped, 35˚C water to flow in a serpentine fashion, which ensures an even heat distribution underneath the mouse, Figure 3-1, A. Components (Figure 3-1, B, C, E, F) were created in SolidWorks®.

For some cell imaging applications, condenser illumination is required; thus, holes were incorporated for light to pass through the bottom (Figure 3-1, B). An additional warm water jacket (Figure 3-1, C) positioned above the serpentine water channel (Figure 3-1, B) provides a two-tier system for improved heat transfer (Figure 3-1, D). Two 35mm dishes can be placed in the incubator. One side has three mounting posts for probes in order to have one dish serve as a monitoring dish for temperature (Figure

3-1, E). Finally, the CO_2/O_2 covering (Figure 3-1, F) is designed to fit snugly over the entire heating system, ensuring minimal gas usage and optimal retention of heat.

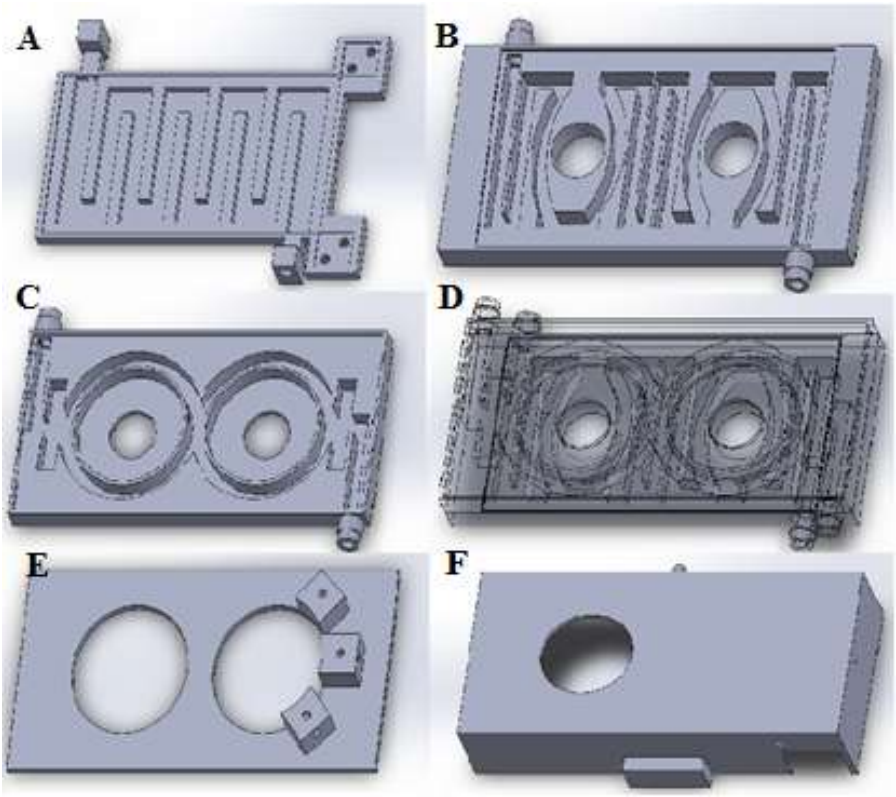

Figure 3-1: Original SolidWorks® Warming Device Design. A. Original animal warming design from our laboratory. B. Original design with condenser illumination. C. Dish housing part. D. Combined heating designs. E. Top, including pegs for wiring. F. CO_2/O_2 covering.

3.1.2 Redesign

Upon extended study of cell viability for this design, it was determined that pumping forces were causing a slight vibration in the device, as the channels cause a turbulent flow. This vibration produced a shearing effect on the cells. To address this, the serpentine channeled part (Figure 3-1, B) was transferred from the bottom of the device to the covering, where it could radiate heat downward to the culture dish. The channels of

both the serpentine and water jacket parts (Figure 3-1, B and C) were widened to allow for slower flow intended to reduce turbulence, providing less force on the culture dishes. Other redesign considerations were to widen the openings through which the condenser illumination could pass so that an inverted microscope could also be used if necessary.

Figure 3-2 elucidates changes from the original design to the redesign. Part B from Figure 3-1 is part C in Figure 3-2. The new design has fewer channels which have been widened to reduce vibration and still allow enough water into the part to maintain temperature. Though it is not explicitly noted in Figure 3-2, the serpentine channeled part is now connected directly to the covering (Figure 3-2, D). The condenser illumination holes have also been made wider to match the hole in the covering, allowing for an upright microscope objective to enter through this aperture.

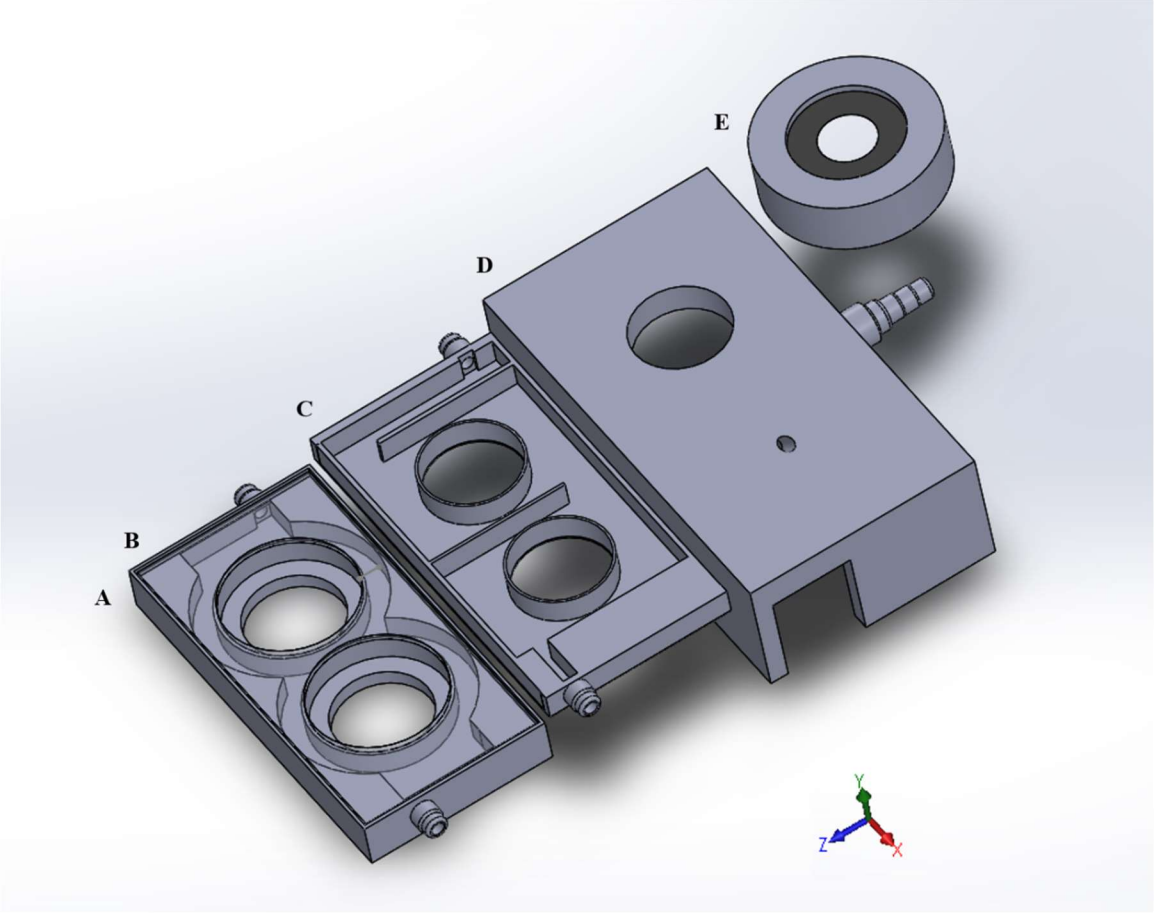

Figure 3-2: SolidWorks® Redesign. A. Original dish housing part, converted to bottom. B. Cover of Part A, outline only. C. Original serpentine channel part, now radiating heat from covering. D. Covering. E. Covering dome with aperture for inserting upright microscope objective lens.

Part A in Figure 3-2 is the original dish housing part (Figure 3-1, C), also called the dish-jacketed part. The dish-jacketed part is now the bottom of the warming system and has been thickened on the bottom to retain heat just as Part B from Figure 3-1 had a 4 mm bottom extension. As Figure 3-2 displays, the channels for this piece have also been widened to allow for less forceful flow. The illumination openings have been widened enough to allow for an inverted microscope objective lens to fit into the warmer to acquire images. Part A is still topped with a two-millimeter layer, Figure 3-2, B, which is

outlined for visualization of the channels in Part A. This piece is similar to Figure 3-1, E, except that the probe housings have been removed.

In preliminary tests of the original system, the culture media noticeably evaporated from the system over the five-hour period. Since the system was originally designed for an upright microscope, an objective dome (Figure 3-2, E) was added to the system to seal off the covering, effectively sealing in gas concentrations and preventing media evaporation. This dome is also 3D printed with only a thin piece of rubber sheeting (shown in black in Figure 3-2) added to enclose the objective. When performing heat tests on an inverted microscope or on the bench, the culture dish cap was simply placed over the top of the hole to prevent gas escape.

3.2 Materials and Methods

The design was saved as individual STL files and transferred to the MakerBot Desktop for Makerware slicing. MakerBot Replicator 2X 3D printers were used for all prints. All prints were defined with a 30% infill, a 0.20 mm infill layer height, and two shells.

Originally, two systems were built, one with PLA and the other with ABS, and were examined for print completion. PLA was printed at 220˚ C with a 70˚ C heated bed. Since the Replicator™ 2X has dual print heads, High Impact Polystyrene (HIPS) was selected as the support filament; HIPS prints best at 220˚ C with a 110˚ C heated bed. Due to this temperature difference, only the supported mid-heater (Figure 3-1, C) part was printed with a HIPS raft. HIPS supports were dissolved in d-Limonene overnight.

ABS was printed at 240˚ C with a 110˚ C heated bed, with the exception of the mid-heater piece (Figure 3-1, C) which was printed at 245˚ C with a 125˚ C heated bed to

ensure flat edges for the ABS supports. Since some ABS can dissolve in d-Limonene, parts were printed with ABS supports instead of HIPS. No rafts were used with ABS prints. Post processing for ABS parts included removing ABS supports with needle nose plyers, a razor blade, and tweezers. A small amount of acetone was applied with a cotton swab to soften difficult areas.

Once all four prints were acquired (Figure 3-1: B, C, E, F) the bottoms of the mid-heater (Figure 3-1, C) and heater cover (Figure 3-1, E) were covered in a thin layer of aquarium-safe silicone. Heater parts were then joined with cyanoacrylate adhesive. The pump connection tubes were attached to the water connector fittings (Figure 3-1: B-C) also with cyanoacrylate adhesive. Once the three pieces of the heater and the pump connection tubes were joined, the entire heat system was covered in silicone to prevent leaks. Styrofoam (one centimeter thick) was placed on the top and bottom of the system for insulation, which can be seen in Figure 3-3, A.

Figure 3-3 displays the progression of the device from the original (A) through an intermediate design (B) through the complete redesign (C). During the redesign, all parts were printed in PLA according to the methods previously described. HIPS was not used as a support filament since supports were only required for the covering and could be easily removed with plyers. Heater parts were joined with cyanoacrylate adhesive as previously mentioned and the heat system was covered in aquarium-safe silicone to prevent leaks. Styrofoam was not deemed necessary for insulation with this configuration, and was not used.

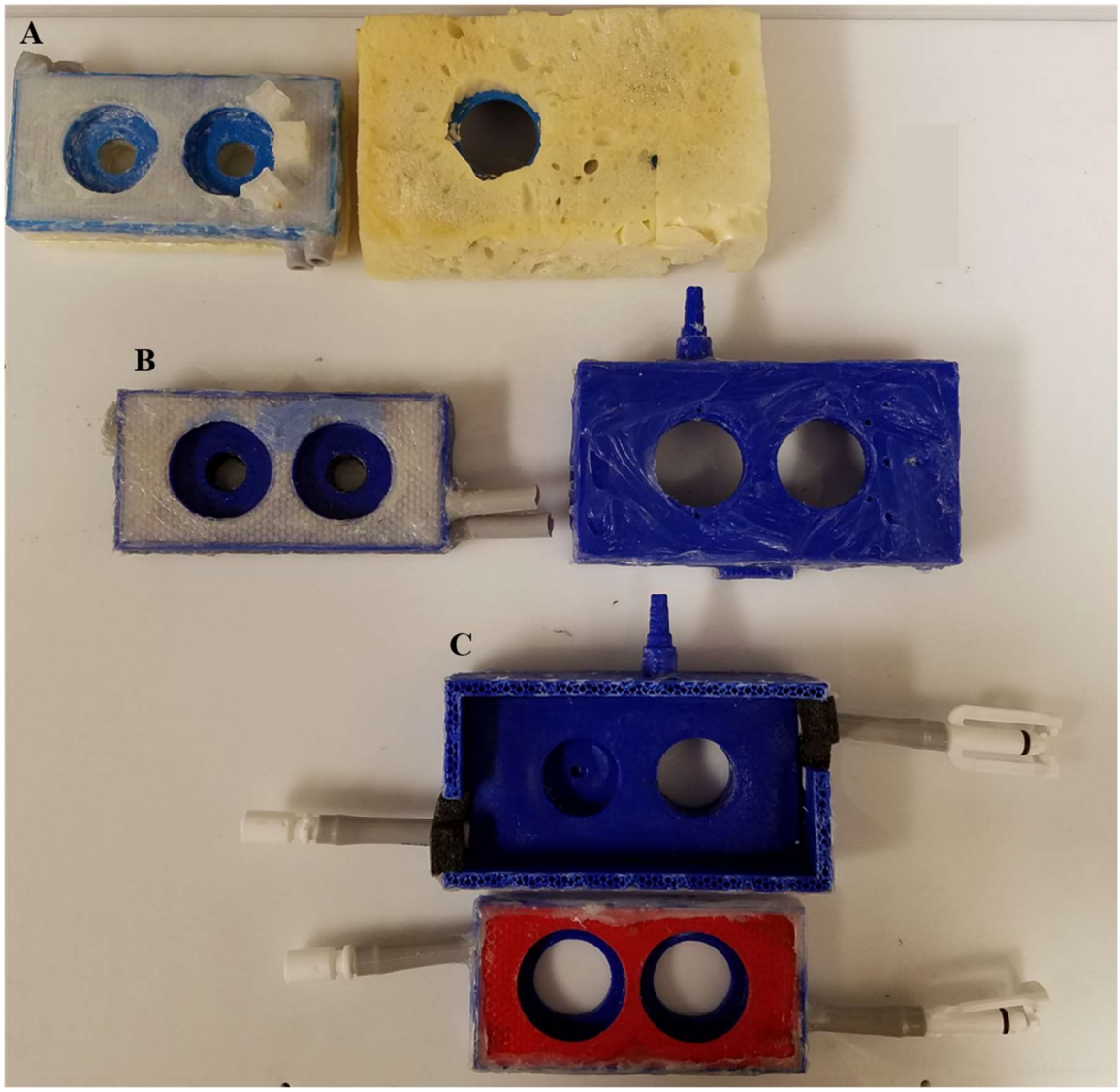

Figure 3-3: Warming Device Iterations. A. Original warming device, 1/2” foam insulates covering. B. Intermediate design; no foam, probe housing moved to the covering. C. Complete redesign: bottom of A and B now found on bottom of covering; Larger illumination holes for inverted microscope.

A Stryker TP700 T/Pump Professional water pump, with a temperature-controlled reservoir, was connected to the two heater plates using flexible water tubing (supplied with pump) and six Clik-Tite® connectors. Fifteen inches of tubing on each side were cut to create four short connection tubes for the Clik-Tite® connectors and a longer u-shaped hose to connect the bottom and middle heating plates. Tubing was secured with zip-ties

to prevent movement of the system from flowing water. The excess pump tubing was placed in Styrofoam tubular pipe insulation. Figure 3-4 depicts the entire system.

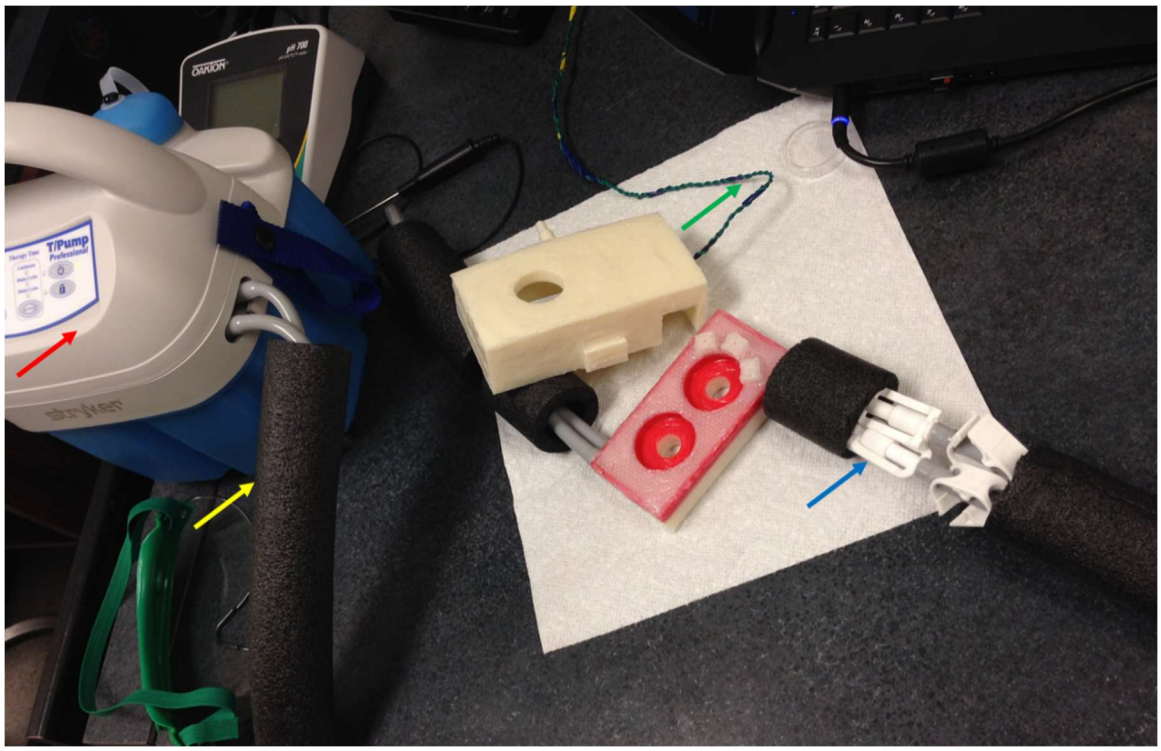

Figure 3-4: Complete System. Red arrow: Stryker® T-pump. Yellow arrow: Styrofoam tubular pipe insulation. Green arrow: Arduino temperature probe. Blue arrow: Clik-Tite® connectors.

3.2.1 Temperature Stability Tests

Original temperature stability tests were run at the 42˚C water pump setting for two hours. A Corning 35mm x 10mm culture dish was filled with 4 mL of Dulbecco's Modified Eagle's Medium (DMEM) and placed into a 37˚C incubator for 15 minutes prior to running tests. The pump was connected and initialized for 10 minutes before recordings were taken. Only the ABS build was heat tested in the original design. A PLA build was tested using an intermediate design, and the PLA redesign build was used for testing.

Once the media was warmed, it was placed into the device and a temperature probe was placed into the media to begin recordings. The temperature probe consisted of a thermistor (Agilent) run through an analog circuit connected to an Arduino Mega 2560. Data were recorded every three to five minutes using PLX-DAQ software. PLX-DAQ is an open-source software program that writes data from an Arduino directly into an Excel spreadsheet [23]. At least three tests were run per time period to give an overall average temperature from the device for that time period.

3.2.2 Cell Culture

SH-EP 1 cells from passage 12-15 were used to assess viability. SH-EP 1 cells were passaged every four days as per protocol, Appendix B-1. Cells were plated onto 35mm dishes at a density of 50,000 cells per dish. Dishes were allowed to come to 80% confluency, approximately three days, before testing. Negative controls were maintained in a CO_2 injected incubator while positive controls were set on a benchtop for the length of the experiment.

pH tests were performed using a digital Oakton pH 700 benchtop meter. Media was removed from cells after experiments and placed into separate conical tubes for individual testing prior to trypsinizing cells for flow cytometry. After pH tests were performed, the media from each conical tube was placed into a 10mL finely marked graduated cylinder to assess remaining media volume after evaporation.

3.2.3 Flow Cytometry

Flow cytometry using propidium iodide (PI) was performed to assess cell viability. Flow cytometry is a technique that measures cell characteristics (cytometry), by flowing cells in a tightly contained fluid stream in front of a laser coupled with an

electronic detector. The signals are then amplified and analyzed using computer software. Typically, flow cytometry signals are achieved by using fluorophores as fluorescent labels. When nonlabelled cells pass in front of the laser, light scatter is detected. When the laser excites the fluorescent label on the target cells, the fluorophore emits photons at a wavelength that is sensed by the electronic detector.

Flow cytometry experiments are used to answer many questions related to cell assessment, such as apoptosis quantification, cell viability, cell surface antigen presence (markers), protein expression, and cell cycle analysis, just to name a few. Another highly useful tool is fluorescence-activated cell sorting (FACS), which is a specialized type of flow cytometry that sorts cells into separate receptacles.

A Beckman Coulter CytoFLEX flow cytometer with accompanying CytExpert 2.0 software was used for all cytometry analysis presented here. Cells were trypsinized, centrifuged, and resuspended in PBS buffer supplemented with 1% BSA, 10% FBS, and 0.1% sodium azide for analysis. PI was added to each suspension at a concentration of 1ug/mL one minute before cytometer readings.

PI is a red fluorescent stain commonly used in flow cytometry to detect cell viability or for cell cycle analysis. It is valuable for these circumstances because PI is an intercalating agent, i.e. attaches to DNA, that is also cell-impermeant, meaning that it does not cross the plasma membrane. Thus, dead and dying cells allow PI to bind to DNA but live cells do not.

3.3 Results

3.3.1 Temperature Stability Tests

Most commercial cell culture incubation systems maintain a tightly controlled temperature system to keep the internal air within 98% of 37˚C (± 0.74˚C), the DIN 12880:2007 electrical laboratory devices standard. Tight control is maintained because cultured cell systems thrive within a relatively small temperature window. Overheating can induce cell death while underheating usually leads to slowed growth rate. Thus, temperature stability was critically important to establish for the incubator. Original temperature stability tests (Figure 3-5) showed that the dish warming system maintained a consistent temperature of 35˚C for up to 90 minutes after a warm up period of 30 minutes. Tests were conducted again using an intermediate design made of ABS, not pictured. It showed that the original double-layered design was capable of maintaining 37˚C for 24 hours, exceeding the design requirements of five hours (data not pictured).

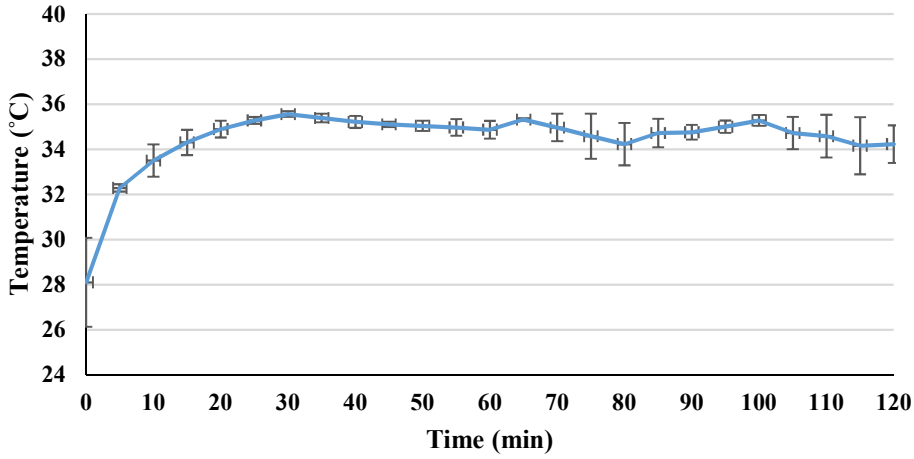

Figure 3-5: Temperature of Media in Original Design. Sustained mean temperature over 90 minutes. (Mean ± SEM).

In the redesign, it was decided that the sensor well should contain distilled water (dH_2O) to ensure humidity throughout longer experiments. It was assumed that the temperature could differ between wells since the well containing dH_2O was enclosed fully with the covering and the testing well, containing media, was not covered in the same way. A dual temperature test was performed to analyze possible well temperature differences, as seen in Figure 3-6. This test was performed in the same way as the tests in Figure 3-5 with the exception of a second temperature probe placed into the media well. Three 24 hr. tests were performed in order to get a mean ± standard error mean value set over time.

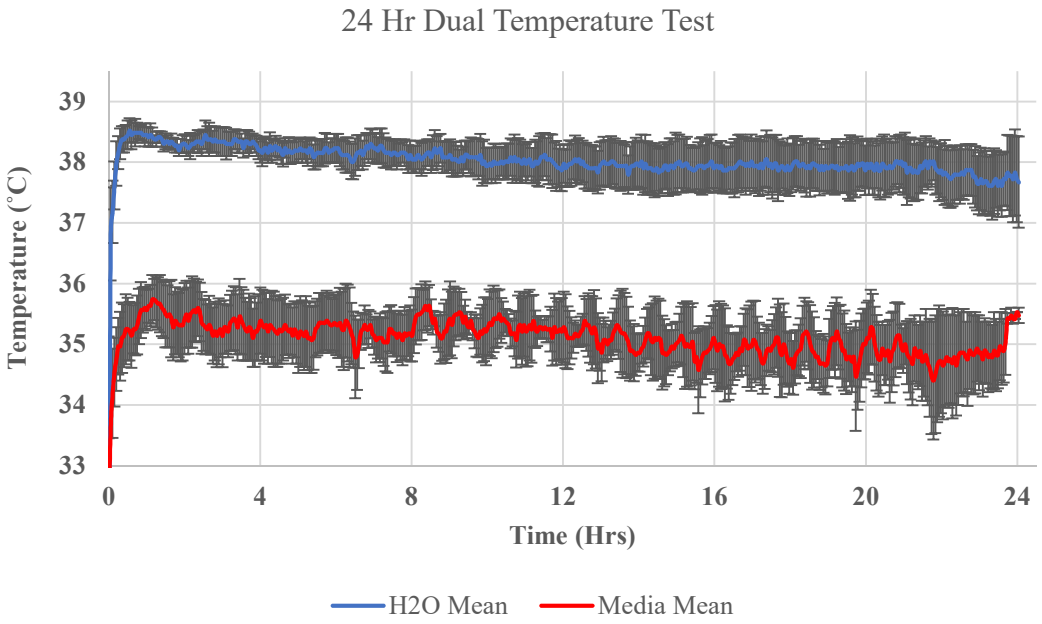

Figure 3-6: 24 hr. Temperature Test Results. Consistent difference in temperature of ~ 3˚C between dH_2O well temperature and media well temperature. (Mean ± SEM; n = 3) Measurements acquired every three minutes, averaged using Excel.

Results showed a definitive temperature difference between the media well and the sensor well filled with dH_2O over the 24 hr. periods. Figure 3-6 shows that the system maintains sustained heat around 38˚C in the dH_2O wells, while the media wells maintain

an average temperature around 35˚C. To assess whether the media temperature could be predicted from the dH_2O temperature since the temperature probe would remain in the dH_2O well during cell experiments, regression analysis of the averaged data in Figure 3-6 was performed. The Pearson's correlation coefficient (r) was 0.6537, denoting a positive linear relationship between dH_2O and media temperatures. The P-value was < 0.0001, considered extremely significant and denoting that temperature changes in the dH_2O wells are useful in predicting temperature changes in the media wells. Figure 3-7 displays the regression analysis chart for media temperature prediction based on dH_2O temperature.

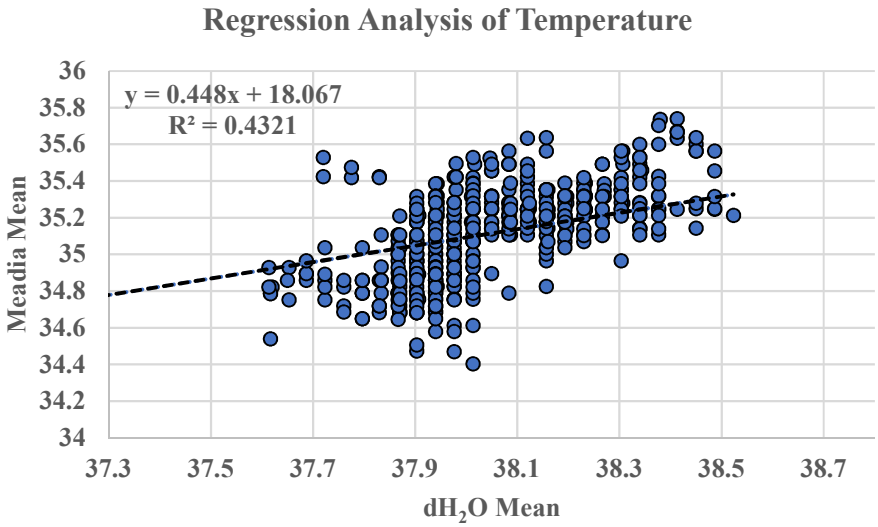

Figure 3-7: Correlation of dH_2O Well Temperature to Media Well Temperature. Prediction equation and R^2 coefficient of determination displayed; n = 3.

As displayed in Figure 3-7, media temperature can be predicted from the acquired dH_2O temperature based on the equation:

$$\text{Media Temperature } (^{\circ}\text{C}) = 0.448s + 18.067. \quad (3\text{-}1)$$

Thus, the temperature of the cell culture media can be monitored during the experiment using this equation in Excel. There is an average of 2.93˚C or ~3˚C difference between the dH_2O wells and the media wells. The mean temperature of dH_2O wells across all three tests was 38.01 ± 0.01˚C and the mean temperature for media wells was 35.1 ± 0.01˚C, which is less than the ideal 36-37˚C for mammalian cell viability.

Though not ideal, it is considered better that media temperature be a little low than high, and the temperatures shown will maintain viability though cell growth rate may be slowed. Further, the pumped water method maintained media temperature stability during the 24-hour tests. The pump system used only has settings of 35˚C, 38˚C, and 42˚C. A pump system with adjustable or higher settings can be recommended when attempting future iterations.

By maintaining temperature stability, the redesigned warming system showed the capability to become a complete stage-top incubation device with added O_2/CO_2 control. Further testing to confirm suitability for cell viability was necessary to confirm that the incubator has the capability to keep cells alive for a minimum of five hours.

3.3.2 Cell Viability

3.3.2.1 Imaging. Cell viability tests were run for 5 hours and 12 hours. Images of cells were taken before and after each test to identify changes in cell morphology. SH-EP 1 cells are an adherent line known to have a flattened epithelial-like morphology [24]. They grow attached to a substrate in a monolayer, often in discrete areas with small spaces in between until they reach confluency. They should exhibit a flattened polygonal shape with regular dimensions, resembling a cobblestone surface. Our SH-EP 1 line is

also grown in a DMEM containing phenol red for easy visualization of pH changes throughout their incubation.

Figure 3-8 displays characteristic before and after images at 5 and 12 hours. Even after five hours, cells left in normal atmospheric conditions lose polygonal shape and the fullness of cell body adhesion. Many cells have retracted, becoming round in shape, and are detaching from the dish as spaces between cells become larger. Changes in media color toward purple are also clearly indicative of pH changes toward alkalinity. Images after 12 hours display clear lack of polygonal shape; all cells became rounded with some blebbing and additional debris, suggesting apoptosis. The survival rate is very low after 12 hours in atmospheric conditions.

Images of cells left in the warming system display thinning of polygonal shapes and some larger cell spacing after five hours. Unlike the atmospheric conditions, there is no visual roundedness of cells and media coloring remains close to commercial cell incubator conditions; Sheldon VWR 2325 model incubator used. After 12 hours, the cobblestone-like appearance is gone, with much larger spaces between cells and a thinner, spindle-like morphology, which suggests cells are stressed. Media coloring indicated an alkaline condition, though it did not seem to be as dark as the atmospheric conditions. These results demonstrate that the warming device maintains adequate conditions for five hours, but cells tend toward apoptosis and death as the incubation time is extended.

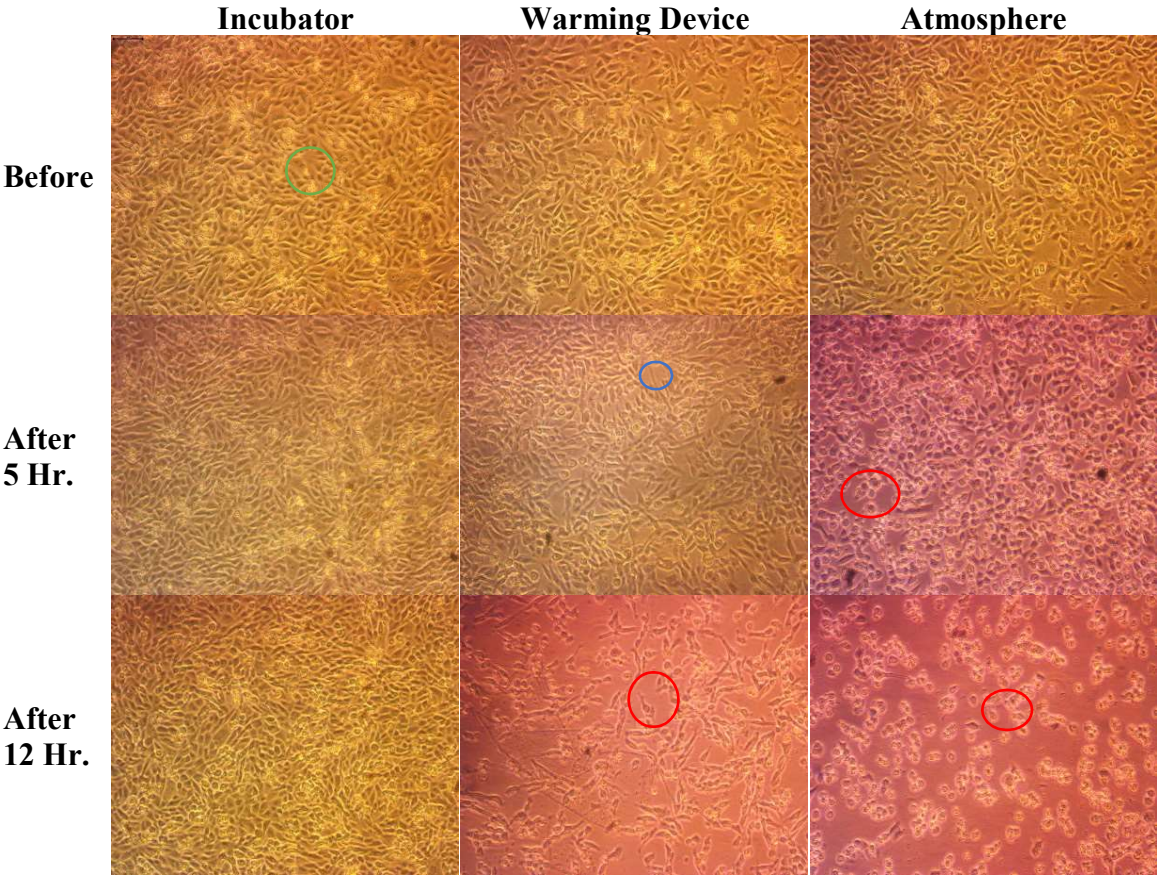

Figure 3-8: Representative Samples of SH-EP 1 Cell Morphology. Sample from each test condition (n = 3 for each condition); all illumination conditions kept same. Green circle: normal morphology with small spaces; Blue circle: thinning of shape; Red circles: retraction and death. 10x objective. Scale bar in upper left corner, 100µm.

3.3.2.2 pH and evaporation. pH is an important indicator of cell health. Media, the direct cellular environment, often contains sodium bicarbonate as a buffer, which is known to increase alkalinity of the media over time. The reason that incubators inject CO_2 into their atmosphere is to prevent CO_2 from leaving buffered media and increasing the alkalinity. Here, pH control is attempted through manually pumping in a premixed gas composition of 95% O_2/5%CO_2 for a length of five minutes at least once every four hours throughout the experiment. The optimal pH for cultured cells is from 7.2-7.7. The pH is indicated in culture media by the chemical indicator phenol red.

Since pH was a concern from the beginning, changes in media color were noted before and after tests. When length of time in the warmer changed media coloring, pH tests were performed to assess the final pH at the end of an experimental time point. An Oakton pH meter, calibrated at room temperature for pH buffers of 4, 7 and 10, was used for all pH tests. Figure 3-9 displays the pH mean ± standard error of the mean for all experimental conditions over the three tests. Average pH was higher than expected for all conditions: 7.8-8.0 for incubator, 8.3-9.1 for the stage-top device, and 8.8-9.2 for benchtop. This increase could be a result of the media temperature change as it cools on the benchtop before testing.

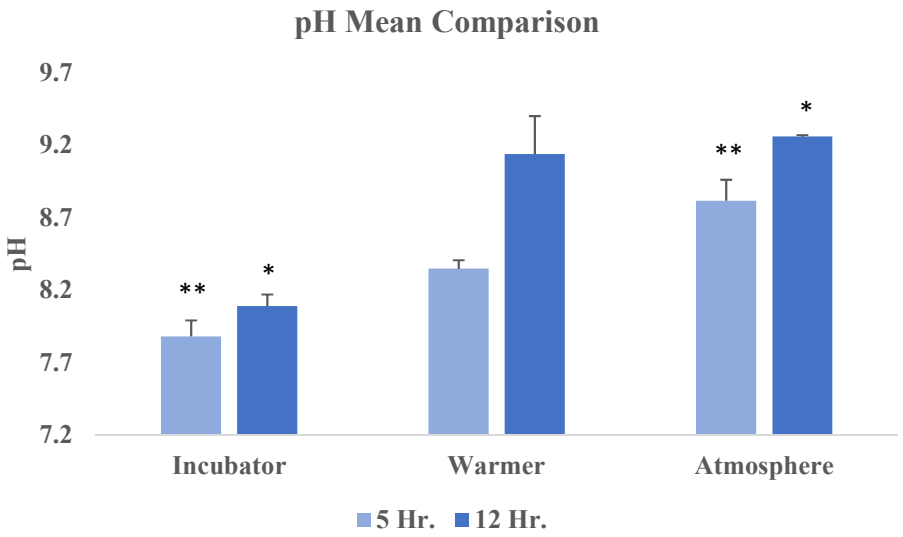

Figure 3-9: pH Mean Comparison. pH differences between 5 and 12-hr tests. Taken post experiment. (Mean + SEM, n = 3). *p = 0.01; **p = 0.003.

Single factor ANOVA was performed to assess differences in the mean pH between conditions. The hypothesis tested was that using the warmer keeps cells viable similarly to that of a CO_2 incubator and more than having them on the benchtop. The null hypothesis was that there is no difference between the groups, with an $\alpha = 0.05$. The

five-hour statistics returned an F value of 17.8 between group means and a corresponding F critical (F_c) of 5.14. The high F value indicates large variability of group means relative to variability within the groups, and $F > F_c$ indicates that variation among the condition means at five hours is significantly greater than expected by chance. The corresponding probability of finding an F value at least as great determined a P value of 0.0030, which was considered very significant. Both $F > F_c$ and $P < \alpha$ suggest rejecting the null hypothesis, showing a significant difference between the groups.

At 12 hours, the F value returned was 12.64 with an F_c of 5.78. Again, variability between group means is significant. The corresponding probability of determining such an F value returned a P value of 0.01, also indicating significance. As with the five-hour tests, both $F > F_c$ and $P < \alpha$ suggest rejecting the null hypothesis. Thus, a significant difference exists between the groups.

To confirm differences between groups, a Turkey-Kramer Multiple Comparisons Test was performed for 5- and 12-hour experiments using an $\alpha = 0.05$. For five hours, the Turkey-Kramer test confirmed that incubator viability is significantly different from benchtop, atmospheric viability. However, differences between the incubator and warmer as well as differences between the warmer and the benchtop after five hours were not significant. Thus, the null hypothesis could be rejected, the alternative hypothesis of incubator to warmer compatibility cannot be assumed based on pH at five hours. Since the q values between both the incubator and warmer as well as warmer and the benchtop are near the critical q value, it suggests that more tests at the five-hour mark may be needed to confirm differences.

The 12-hour Turkey-Kramer test again showed a significant difference between the incubator and benchtop, as would be expected. It also confirmed that there was a significant difference between the incubator and stage-top device but no significant difference between the warmer and the benchtop after 12 hours. Differences indicate that the pH of the media in the stage-top device increases to levels near atmospheric conditions after 12 hours, which could account for the stress observed in the warmer 12-hour images.

The pH is finely controlled in the media environment since cell health is quickly affected by pH drift toward either acidity or alkalinity. The pH control in this system was intended to be controlled using manually pumped in O_2/CO_2 premixed gas, periodically introduced to maintain favorable concentrations. Since pH is indicated as drifting toward alkalinity as experiment time is lengthened, it must be assumed that gas concentrations within the stage-top system are not kept as necessary to maintain proper CO_2 balance. Premixed gas was not left on throughout the experiment since it runs out quickly and becomes expensive if overused. As such, it is suggested to either increase gas introduction times or more finely control gas leaving the system.

Evaporation of media also became a concern when dishes left in the intermediate stage-top device over 12 hours lost considerably more media. Thus, in the redesign, the dH_2O was added to the back well and media volumes were taken account of at the end of each experiment. Figure 3-10 displays the mean media remainder post experiment with standard error. Single factor ANOVA statistics returned $F < F_c$ and $P > \alpha$ for both 5 and 12-hour tests, which showed no significant difference among groups. Statistics indicate

no significant difference between groups from either the 5- or 12-hour tests. Thus, evaporation can be considered the same between all groups.

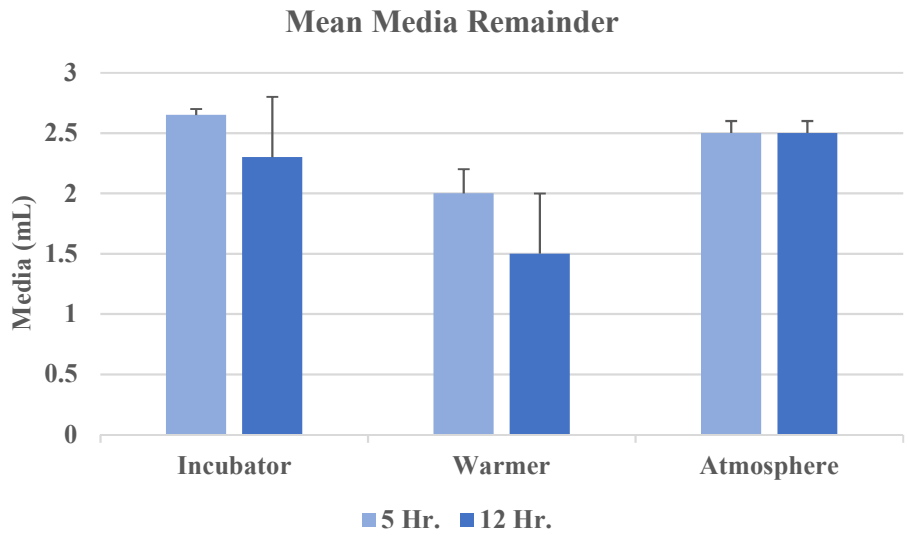

Figure 3-10: Mean Media Post Experiment. Shows media remainder in mL over 5 and 12-hr tests. No significant difference. (Mean + SEM, n = 3). Evaporation calculated as 3 mL – remainder.

Since increased evaporation is undesirable in an incubation device, no significance between groups at either 5 hours or 12 hours can be considered advantageous for the stage-top device. However, since means look generally lower for 12-hour tests, a paired t-test was performed between 5- and 12-hour means to assess a trend of evaporation over time. The two-tailed P value was 0.1528, showing no significant difference between times.

3.3.2.3 Flow Cytometry To assess cell viability, flow cytometry was performed with the intercalating stain PI. PI is often used with a 488 nm laser line and has an excitation max of 535 nm. The emission maximum is approximately 615-620 nm. Since PI and PE (R-phycoerythrin) emission spectra are closely related, the PE channel is often used to assess PI fluorescent intensity. We have chosen 488 laser excitation light in

combination with the 585/42 nm BP fluorescence emission filter (PE) to interrogate the cells as discussed in Appendix A.1.1.

Data was acquired from events occurring in both the FITC and PE channels. It was assumed that autofluorescing cells (unmarked) would be more pronounced in the FITC channel while stained cells would be more pronounced in the PE channel, as discussed in Appendix A.1.2. All events were narrowed into relevant populations using a series of gating methods: the singles gate, time gate and forward and side scatter (F&S) gate. Gated populations were then assessed for live and dead populations based on intensity. Both the FITC channel and the PE channel were compared with forward scatter areas as well as each other to assess differences in intensity. Figure 3-11 depicts characteristic histograms and dot plots of the gated data for a five-hour experiment control.

A

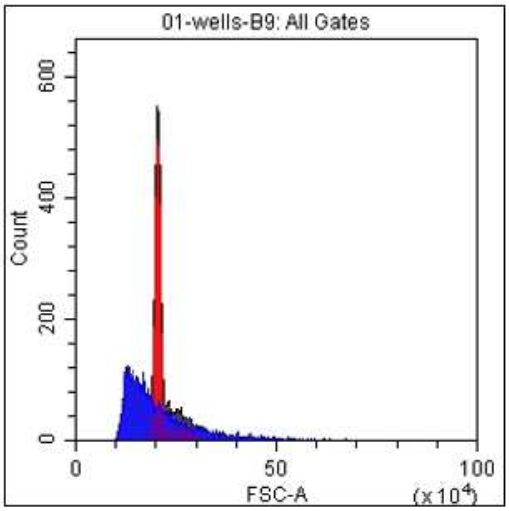
01-wells-B9: All Gates
Count
FSC-A
(x10⁴)

B

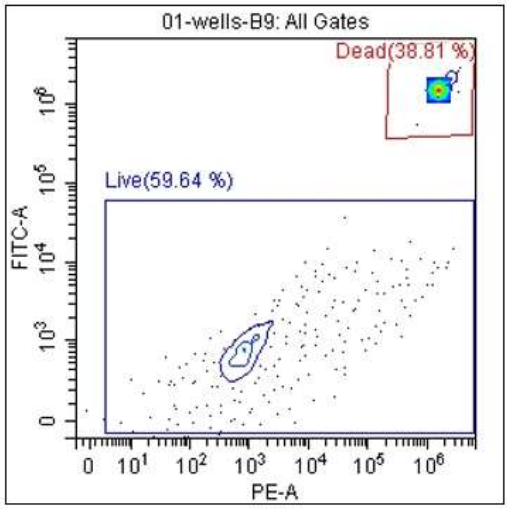
01-wells-B9: All Gates
Dead(38.81 %)
Live(59.64 %)
FITC-A
PE-A

C

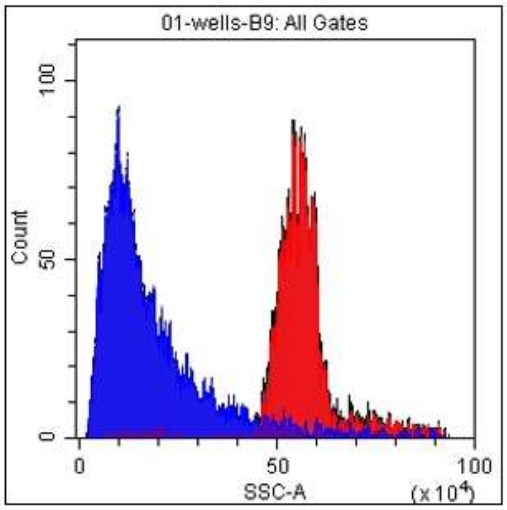
01-wells-B9: All Gates
Count
SSC-A
(x10⁴)

D

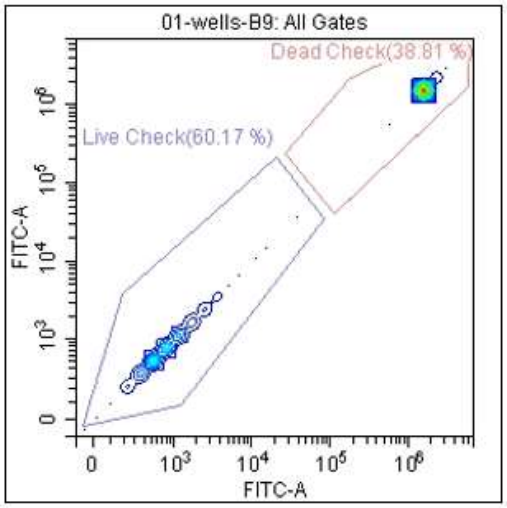
01-wells-B9: All Gates
Dead Check(38.81 %)
Live Check(60.17 %)
FITC-A
FITC-A

E

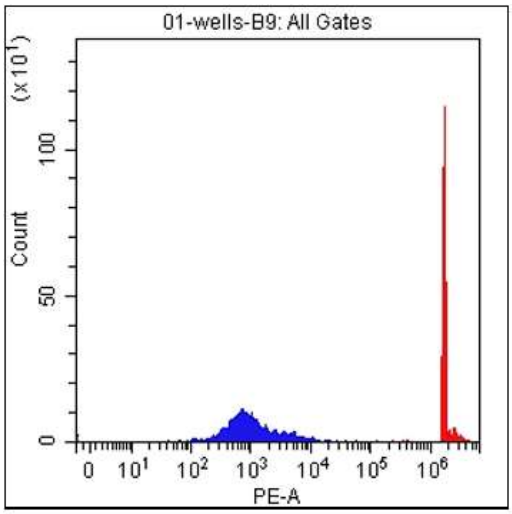
01-wells-B9: All Gates
(x10¹)
Count
PE-A

F

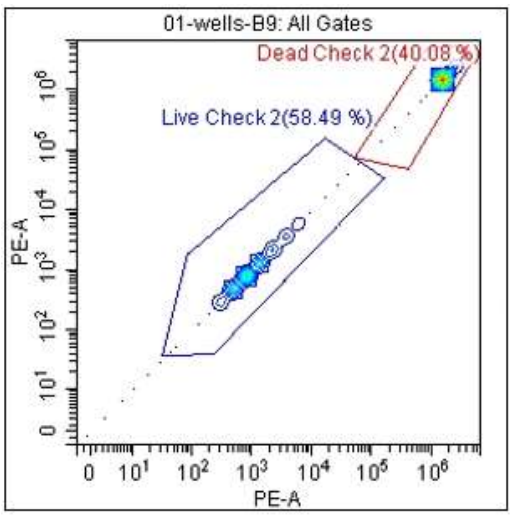
01-wells-B9: All Gates
Dead Check 2(40.08 %)
Live Check 2(58.49 %)
PE-A
PE-A

G

Tube Name: 01-wells-B9
Sample ID:

Population	Events	% Total	% Parent
All Events	10000	100.00 %	100.00 %
Singles Gate	5927	59.27 %	59.27 %
F&S Gate	5763	57.63 %	57.63 %
All Gates	5671	56.71 %	56.71 %
Live Check	3412	34.12 %	60.17 %
Dead Check	2201	22.01 %	38.81 %
Live	3382	33.82 %	59.64 %
Dead	2201	22.01 %	38.81 %
Dead Check 2	2273	22.73 %	40.08 %
Live Check 2	3317	33.17 %	58.49 %

Figure 3-11: Characteristic Univariate and Bivariate Plots of Control. A. Forward scatter histogram. B. PE-A vs FITC-A dot plot with two distinct populations, low intensity considered autofluorescing and high intensity considered stained by fluorochrome. C. Side scatter histogram. D. FITC-A contour plot identifying areas of event intensity within the FITC bandwidth. E. PE-A histogram, showing high intensity peak and indication of PI at 106. F. PE-A contour plot confirming areas of Live and Dead intensity. G. Population data extracted from graphs.

Figure 3-11, panels A, C, and E shows large populations of unmarked cells and a smaller population of stained, dying cells. Populations are validated by the contour plots in Figure 3-11, panels D and F which define a heavier population percentage around the low intensity cells marked Live. Percentages of the populations were extracted from the data as seen in Figure 3-11, G, and plotted on a scatter graph to summarize findings. Data indicates a difference in cell viability with more live cells in atmospheric conditions. Since atmospheric conditions are assumed dead or dying after five hours, flow cytometry data is not in line with other evidence, images and pH, which indicate a difference in viability with more live cells in commercial incubation. Thus, flow cytometry data is considered inconclusive.

3.3.3 Cost Analysis

When undertaking any new laboratory project, cost efficiency is a necessary consideration. Prototyping new tools should generally only be considered if cost and/or effectiveness of using existing methods or tools outweigh cost and effectiveness of the proposed prototype. One distinct advantage to using an FDM machine to create a system of parts is that parts will generally be very cost efficient, since the FDM materials are inexpensive. Here, we have compared a top selling stage-top incubator system with basic components, Table 3-1, to our proposed 3D printed system, Table 3-2.

Table 3-1: Cost of a Top Selling Stage-Top Incubator System

Temperature Unit	$ 6,878.00
CO_2 Unit	$ 6,765.00
Humidity Controller	$ 2,828.00
Air Pump	$ 616.00
Total	**$ 17,087.00**

The current price of a stage-top incubator with temperature and CO_2/O_2 controls ranges from $14,000 to $30,000 with the cost of the basic system from Table 3-1 in the lower price range. Advantages to this system are that the heating components are considered modular and may fit a variety of dishes when extra parts are purchased. This system also comes with a gas control unit, which ensures proper gas concentrations throughout incubation.

In contrast, the components of our 3D printed system are a fraction of this cost (Table 3-2). Five complete 3D printed systems could be purchased for the cost of one basic commercial system. The only large cost is the 3D printer itself, and other models

have been made in recent years that are not as expensive as the one listed. As the results have indicated, this system is capable of temperature control, but lacks the refinement of a gas control unit such as the top selling brand's CO_2 unit. The 3D printed housing also cannot be considered modular and must be reprinted to house different dish sizes. However, recurring printing cost is extremely low, ~$40 per extra housing.

Table 3-2: Cost of 3D Printed Stage-Top Incubator

Equipment	**Initial Cost**	**Recurring Cost**
MakerBot Replicator 2X	$ 2,499.00	
One roll of PLA, ABS, HIPS filament	89.99	
Water Pump (Model TP700, Stryker)	415.00	
Clik-Tite® Connectors (3 Sets, Stryker)	24.00	16.00
Silicone (Aquarium Sealant, Marineland)	8.29	8.29
Insulating Foam Sealant (Great Stuff)	6.48	6.48
Styrofoam tubing (Frost King)	1.98	1.98
Cyanoacrylate adhesive (Loctite)	4.98	4.98
CO_2 Flow Meter (Euthanex)	285.00	
Total	**$ 3,334.72**	**$ 37.73**

This price difference is enough that the suggestion of purchasing a single gas control unit from Table 3-1 to incorporate into the 3D printed system of Table 3-2 is not out of the question. Table 3-3 demonstrates the cost if valuable parts of the top selling brand are to be incorporated into the 3D printed system without the CO_2 flow meter. The cost difference between the complete top selling brand system and the proposed

combination is $6,656.28, a savings of 39% over the complete system. The proposed system is also an increase of $7,096.00 over the original 3D printed system, which represents an increase of 313%.

Table 3-3: Proposed Incubator Combination

Equipment	**Initial Cost**	**Recurring Cost**
Top Selling Brand CO_2 Unit	$ 6,765.00	
Air pump	$ 616.00	
3D Printed Stage-Top Incubator System	$ 3,049.72	$ 37.73
Total	**$ 10,430.72**	**$ 37.73**
Alternative Total (if have printer)	**$ 7,931.72**	

One other alternative is also suggested in Table 3-3; the circumstance in which a laboratory already owns a commercial 3D printer for printing labware. In this case, the original cost of the 3D printer is negated and all other proposed costs are included. The initial cost becomes $7,931.70, which represents a 46% price reduction from the top selling system and a 237% increase over the original 3D printed system. Potentially two of the proposed combined systems may be purchased for the price of one of the top brand systems.

3.4 Discussion

This work presents a custom designed, printed, and tested stage-top incubator system for long-term, *in vitro* microscopy experiments. As 3D printing for prototypes or parts has become widely available, inexpensive, and easy to use, it is practical to begin viewing the FDM machine as a possible choice for making custom laboratory equipment.

A great advantage to this is that printing takes little time when compared to other prototyping methods and can be fully completed in lab, requiring no outside machining or costs.

In this case, a stage-top incubator was required for experiments that would last up to five hours on the microscope. It was important to maintain a stable environment as well as create an easily built and replicated design. To do this, an existing 3D printable animal warming device constructed in our laboratory was transformed into the original dish warming device, which was redesigned into the stage-top incubation system presented.

The redesigned system reduces water flow vibrations by lowering turbulence in flow. Heat is radiated from the top of the housing and flow is slowed by wider jacketed channels around the dishes. Increasing humidity is also addressed by adding distilled water to the sensor well, which is hotter than the experiment well, providing faster evaporation of water into the housed air.

An equation for temperature of the experiment well based on the temperature of the sensor well was also calculated so that temperature of the experiment well may be monitored at all times. It is also easy to approximate since the temperature of the sensor well is normally three degrees above that of the experiment well. Though the experiment well temperature is not the ideal 37˚C condition of a typical mammalian incubator, it falls within viability conditions, though growth rate may be slowed. It is also suggested that using a water pump with a higher temperature setting could solve this problem.

The overall performance of the stage-top incubation system leads to the conclusion that it is an acceptable alternative for five hours, though it cannot be used

much longer than that without potential redesign. This conclusion is based on the images of cells left in the printed system, the pH after incubation, and the evaporation of media after five hours in comparison to a commercially incubated control and a positive control left on the benchtop. Fluorochrome confirmation of cell viability remain inconclusive, as the flow cytometry data presents unreasonable suggestions of viability in the control.

Images indicate that, unlike atmospheric conditions, there is no visual roundedness of cells and media coloring remains close to commercial cell incubator conditions after five hours. Media coloring toward alkalinity at 12 hours also suggested that pH rise was a factor in cell tendency toward apoptosis and death as the incubation time lengthens.

Average pH was found higher than expected for all conditions, although this may be explained as a factor of temperature as the media cools while on the bench awaiting measurement. For 5- and 12-hour experiments, a significant difference was found between the pH means for all groups. Upon further statistical testing, it was determined that neither differences between the incubator and warmer nor the warmer and benchtop could be assumed at five hours, indicating that more tests at the five-hour mark may be necessary to confirm differences in mean pH.

The printed system was similar to atmospheric conditions at 12 hours, indicating a problem with maintenance of pH over time. Since atmospheric CO_2 should maintain equilibrium with the bicarbonate buffer, it is most likely that loss of atmospheric CO_2 is the cause of pH shift. Data suggests that more tightly controlled CO_2 loss within the printed system should help alleviate cell viability issues.

Humidity is not considered a real issue for the redesigned stage-top system as evaporation was found to be the same among all treatment groups over all time periods, unlike evaporation in the original design. It is believed that the addition of distilled water to the sensor well alleviated this problem.

Finally, for the budget conscious laboratory, 3D printing can represent a method of acquiring necessary equipment that is cost prohibitive otherwise. Five complete 3D printed systems, including the printers, can be purchased for the cost of one top selling basic commercial system. However, the stage-top incubation system presented requires design modification and reprinting for varying dish size and is not suitable for long-term experiments over five hours. To address design modification for varying dish size, recurring printing cost for different dishes is also extremely low and requires only a few days to print and refine.

To address suitability for experiments over five hours, a combination of the 3D printed stage-top design with a purchased CO_2 unit and air pump, could be beneficial. The cost difference between the complete top selling brand system and the proposed combination still saves almost 40% over the complete brand system, and 46% if the laboratory already owns a FDM machine.

This work supports the overall movement of collaboratively sharing open source labware ideas on websites like Thingiverse or the NIH 3D Print Exchange. Useful laboratory equipment, like the commonly used stage-top incubator, can be created, shared with the scientific community, and expanded upon within that community as others locate and redesign files they also need.

CHAPTER 4

REVIEW OF STEM CELLS AND THE SUBVENTRICULAR ZONE NICHE

4.1 Stem Cells

A stem cell is an undifferentiated cell with two important capabilities [25]. First, it is able to proliferate, that is it divides to create more stem cells in a process called self-renewal. Second, a stem cell can give rise to a particular set of differentiated, specialized cell types. Self-renewal ensures a stem cell population throughout life, and differentiation into certain cell types allows for tissue repair when necessary.

It is believed that stem cell research will grant us the capability to grow whole tissues for transplant or implant cells for repair. Since stem cells can be maintained in a laboratory setting, growing stem cells into specialized types for disease research and individualized devices such as "lab-on-a-chip" [26] is possible.

Stem cells are found both in embryos and in mature tissues, the former being called embryonic stem (ES) cells and the latter being called adult or somatic stem cells. These cells are further distinguished by their potency. In 1957, Waddington presented the epigenetic landscape model [27] in an attempt to characterize epigenetic patterns associated with differentiation potential. Figure 4-1 is a modern revision of Waddington's model. The image is of a marble (cell) rolling down a hill (epigenetic potential). Each

stage depicts key differences of cell developmental potential as the cell comes to a terminally differentiated end, or unipotency.

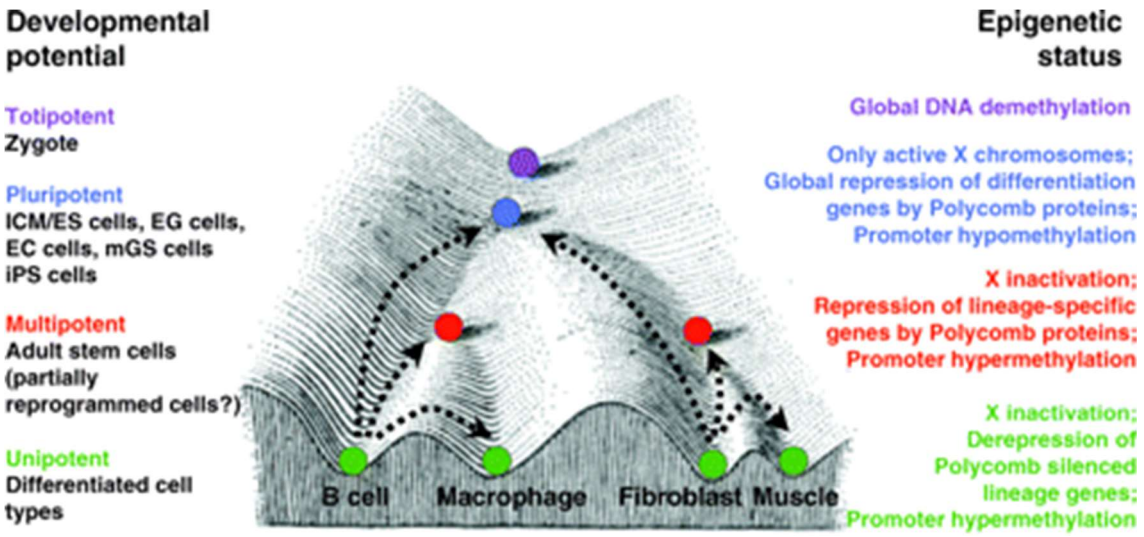

Figure 4-1: Modern Adaptation of C.H. Waddington's Epigenetic Landscape Model. Reprinted from [28].

From Figure 4-1 it can be surmised that ES cells are pluripotent cells capable of differentiating into any adult tissue type. Depicted along with ES cells are iPS cells, or induced pluripotent stem cells. These are terminally differentiated cells transformed into stem cells through transcription factors [28], technology advanced since the early 2000s [29]. Generally, it is believed that adult stem cells are restricted to cell lineages of their origin and are called multipotent. Adult stem cells are, therefore, referred to by the cell types they can become, such as mesenchymal stem cells (MSCs), hematopoietic stem cells (HSCs), or neural stem cells (NSCs).

Stem cell niches, or specialized areas where stem cells are found, exist all over the body and are important to stem cell maintenance and differentiation. These niches provide environmental cues believed to enable growth into particular cell types and sustain self-renewal [30, 31]. Two areas of the adult brain have specialized NSC

microenvironments, or niches. These niches are the dentate gyrus subgranular zone (SGZ) and the subventricular zone (SVZ) of the lateral ventricles.

The stem cell work in this dissertation revolves around NSCs, their potential, and their niches. NSCs are of particular importance because much neural damage and many neurodegenerative diseases are still untreatable, which combine to become some of the most pressing health problems in the United States and worldwide [32]. Neural deficits and loss of function can lead to depression, productivity loss, and exorbitant medical costs for individuals, families, and society [33]. Thus, the potential of neural repair "by replacing cells lost through disease" or damage carries much significance [34].

4.1.1 History of Neural Stem Cell Discovery

Although it is now understood that adult neurogenesis, the generation of functional neurons from NSCs [35], occurs continually throughout life, this was not always the popular belief. Thus, the history of NSC discovery and the excitement it generated are of importance when approaching the scientific community mindset about NSCs. While neurogenesis was first described in the SGZ of young rats (birth to three months) in 1965 [36], adult neurogenesis was not widely accepted in the scientific community. Unacceptance was mostly because the characterization and identification of proliferating cells was unclear and therefore inconclusive. Furthermore, neurogenesis was deemed unsuccessful in primates [37], which are considered much closer human relatives than the rats in Altman's 1965 study.

Adult neurogenesis was not formally accepted until the 1990s. Luskin, in 1993, showed that the SVZ generated neurons that "differentiated into granule cells and periglomerular cells of the olfactory bulb-the two major types of interneurons" [38] by

injecting neonatal rat pups with a tracer. Around the same time, Lois and Alvarez-Buylla presented evidence that proliferating adult mouse SVZ cells differentiated directly into neurons and glia, calling them neuronal precursors and arguing against the prior concept that SVZ cells died *in vivo* after proliferation [39]. Evidence like this spurred on studies of neurogenesis in the mammalian brain throughout the '90s.

Then, in 1998, Eriksson *et al*. reported that the adult human brain routinely spawns neurons in the hippocampus SGZ [40]. This evidence, combined with following studies describing neurogenesis in the human brain [40, 41], encouraged the hope for stem cell therapies targeting neural deficits, degeneration, and disease. Big questions still being addressed center on stem cell stimuli and steps in neurogenesis, niche interaction, where differentiating stem cells migrate and what factors affect migration, and finally, how differentiated precursors integrate into the tissue.

4.2 The Subventricular Zone

Studying the SVZ has yielded major insights into stem cell generation, migration, and activation. Today, the generation of interneurons from the SVZ has been characterized by three distinct stem cell types. The first is the multipotent NSC, also called a type B cell in this context. In 2004, Merkle *et al*. [43] found that adult NSCs are derived from radial glia in the SVZ. That same year, a second type of progenitor cell, intermediate progenitor cells (IPCs), also called transit amplifying progenitors, were characterized as progenitors that "divide away from the ventricular surface"[44], [45]. These are referred to as type C cells. Neuroblasts, type A cells, are generated from IPCs. Figure 4-2, adapted from Ming and Song [35], provides a good depiction of the way these cells are now believed to form.

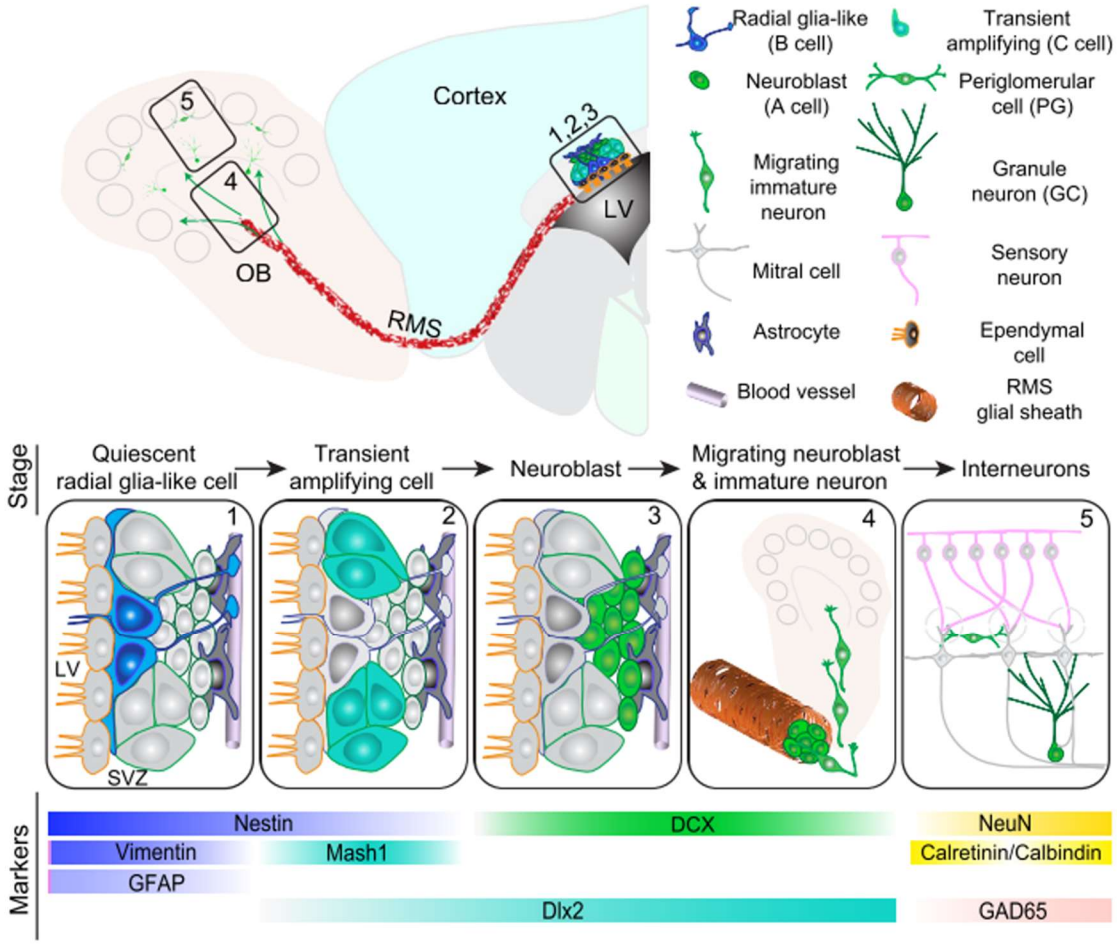

Figure 4-2: The Subventricular Zone and Rostral Migratory Stream. Adapted from Ming and Song [35].

From Figure 4-2, the rostral migratory stream (RMS) can also be visualized. The RMS is a major migratory pathway in rodents where neuroblasts travel from the SVZ niche to the olfactory bulb (OB). The RMS provides an excellent site to study stem cell migration and phenotypic transformation factors for three reasons. First, progenitors travel a large distance from the SVZ down the RMS to the OB, 5-8 mm [46]. Second, neuroblasts also differentiate into more mature phenotypes as they migrate, and some of these cells rapidly divide [46]. Finally, they eventually integrate into the OB as interneurons [38] as depicted in Figure 4-2.

Cell migration is necessary in embryonic development, tissue genesis, and wound healing. It involves complicated biochemical and mechanical signals as well as a complex network of intracellular interactions. With respect to the brain, neural cell migration is of interest because regeneration in the brain is believed to be very limited. Though neurons in the SGZ travel over a small area to integrate into the dentate gyrus [47] and SVZ neuroblasts travel down the RMS to integrate into OB interneurons, it still leaves the question of whether precursors travel to a site of brain injury for wound healing. In 2004, Goings *et al*. published that labelled cells from the SVZ could be found in the area of a cortical lesion after three weeks, and that migration to the OB had been lessened as a result [48]. Jablonska *et al*. also found that transplanted, tagged precursors travelled from the SVZ to a site in the corpus callosum after demyelination [49].

Though these studies are promising, there is also evidence to suggest that most cells originally from the SVZ that are injected into nonneurogenic sites of injury do not produce neurons [42], possibly preventing adequate wound healing. Though reasons for astrocyte over neuron formation in nonneurogenic sites are not well understood, we can postulate that astrocyte formation may be favored due to the regulatory functions of astrocytes. Astrocytes help regulate cerebral blood flow to the brain, providing essential and consistent supply to support function [50]. They also take up glutamate and release glutamine in the glutamate/glutamine cycle necessary for glutamatergic neurotransmission. As such astrocyte formation may be favored as a way to prepare the regulatory foundation that neurons need before neurons are allowed to form. However, studies have also found that “SVZ cells transplanted to another SVZ generate large numbers of neurons for the recipient animal OB” [51]. Thus, understanding niche

transforming characteristics and why migration from the niche itself sustains progenitors is of utmost consequence.

NSC activation can also be studied in the SVZ, since there remain questions of what in the niche triggers adult NSC activation. Evidence from a 1994 experiment by Morshead suggests that NSCs are mostly dormant, called quiescent, in normal CNS while precursors (type C cells from above) proliferated [52]. Since then, several laboratories have researched aspects of the niche that may be responsible for the observed quiescence in NSCs, including blood supply, cytoarchitecture, and cell signaling.

One study by Tavazoie *et al*. in 2008 suggests that "the SVZ vascular plexus whose planar structure and composition is different from vessels in nonneurogenic brain regions" may be a large part of the reason for advanced progenitor function in the area [53]. A cytoarchitecture study by Mirzadeh *et al*. in 2008 also suggests that the niche could be split into two compartments with active progenitors being found in the SVZ and more quiescent NSCs touching the ventricular zone in a pinwheel architecture that intercalates the ependyma [54]. Finally, a 2010 study by Kazanis *et al*. concluded that the "ependymal cell layer generates signals that may be at least as important as the vasculature in regulating mitotic activity of stem and precursor cells" [55].

4.2.1 Approaches to Characterize the SVZ.

Scientists have used several methods to further understand NSCs and their niches. A method developed early on was to dissect out the SVZ of pups or juvenile mammals such as mice, then dissociate the tissue and put the cells into a defined media with certain mitogens like EGF [56], [57]. This technique allowed researchers to study progenitors from the SVZ niche in detail, although removing the cells from *in vivo* conditions and

putting them into *in vitro* conditions necessarily alters cell mechanisms as cells adapt, especially over time.

Histological sections have also been frequently employed in order to determine migration paths and properties. It was through histological sections and confocal optical sectioning that much of the SVZ and RMS was originally characterized [46]. This method is not ideal, however, because migration is a dynamic process that occurs over time. Sectioning only permits still images of an on-going process, thereby not allowing the temporal resolution needed to fully explore precursor cell migration and differentiation.

Wholemount lateral wall explant (WM) extraction is a technique originally developed in the Alvarez-Buylla laboratory [58]. It involves sacrificing the animal, extracting the brain, then micro-dissecting the hippocampus away from the lateral wall where the lateral ventricles lie. The intact brain tissue, including the SVZ, can then be visualized. This is advantageous because it preserves the cytoarchitecture of the SVZ, allowing for visualization of the natural pathways, normal relationships and typical mechanisms of the resident stem cells.

As with all research methods, however, there are drawbacks. The main drawback to using the WM technique is that it still sacrifices the animal and the live tissue cannot be maintained over long periods of time since *ex vivo* conditions are not suitable for maintaining tissue. Thus, tools and technologies must be developed to improve the study of NSCs in the SVZ and further the field of stem cell research.

In the 2013 review by F. H. Gage and S. Temple [59], several foundational questions now facing NSC researchers were discussed. Table 2 of that review also

addresses the development of tools necessary to parse out these questions. Gage points out that 2D and 3D imaging tools for *ex vivo* imaging are desired and necessary for the advancement of questions relating to NSC interaction with the niche. That is, what are the static and dynamic interactions of NSCs within the SVZ? A reprint of this list is found in Figure 4-3.

In Chapter 5 of this dissertation, a novel imaging tool designed to facilitate 2D and 3D *ex vivo* (wholemount) SVZ research is described. This tool set addresses common issues found when attempting live wholemount imaging, which is desirable for preserving the dynamic relationships of the niche. Thus, this newly engineered tool is presented as one solution for the toolbox of technologies from Gage and Temple's "Wish List of Technologies that will Accelerate or Enable Important Directions in NSC Research" [59].

Table 2. Wish List of Technologies that Will Accelerate or Enable Important Directions in NSC Research

Tool	Questions		Translation
More antibody and other markers to prospectively identify NSCs and NPCs	What is the range of types of NSCs and NPC present in mouse and human?		Understanding the contribution of NSC lineages to disease
Diverse fluorescent markers to report multiple genes, multiple proteins	Visualize complex elements in the same cell		
Broad multiplex imaging: for immunostaining, in situ and gene expression reporting	To track multiple molecules simultaneously—analysis of networks, pathways and multimolecular complexes	How do NSC pathways change during development and with aging?	
3D cultures that recapitulate human neural development; integrate engineering	What mechanisms underlie human NSC development into neural progeny?	What morphologic changes accompany CNS development?	Improved cell transplants and prostheses and disease models
More 2D and 3D imaging and analysis tools ex vivo	How do NSCs interact with niche cells, statically and dynamically?	Quantification of image information	Imaging standards for cell products; pathology assessment
High definition (deeper and higher resolution), in vivo imaging	What is the dynamic behavior of NSCs in vivo in the normal niche?	How do NSCs migrate and integrate in vivo?	Precise cell tracking after transplantation in vivo
Closer collaborations between basic, clinical, applied, and commercial stake holders	What are the clinical implications of NSC-based discoveries?		Critical for effective translation
Better nonviral transfection methods	Accelerate and reduce the cost of answering many questions about NSCs		Allow easy, high-throughput screening
Improved models of neurological disease	What is the disease mechanism?	What pathways are best targeted?	Could supplant animal models for efficacy and some tox studies

Figure 4-3: List of Future Technologies for NSC Research. Reprinted from [59] with blue outlining for emphasis.

CHAPTER 5

PICS: A MACHINED ENHANCEMENT FOR PLANAR IMAGING OF CURVED SURFACES, SPECIFICALLY WHOLEMOUNT BRAIN IMAGING

The subventricular zone (SVZ) is one of two main regions in the brain where neurogenesis occurs in mice as well as humans [60]–[62]. In the SVZ, quiescent neural stem cells (type B cells) give rise to transit-amplifying cells (type C cells) which form neuroblasts (type A cells). In rodents, neuroblasts formed in this region travel in chains down the rostral migratory stream to the olfactory bulb where they become interneurons. There is a large interest in studying the native structure and function of this neurogenic niche , as well as its roles in development and brain injury, due to the therapeutic potential of neuronal progenitors [62]–[65].

Wholemount lateral wall explant extraction is a technique originally developed in the Alvarez-Buylla laboratory [58]. It involves sacrificing the animal, extracting the brain, then micro-dissecting the hippocampus away from the lateral wall where the lateral ventricles lie. The intact brain tissue, including the SVZ, can then be visualized. This is advantageous because it preserves the cytoarchitecture of the SVZ, allowing for analyzation of the natural pathways, normal relationships and typical mechanisms of the resident stem cells. Murine lateral ventricular wall wholemounts (LVWMs) prepared this way conserve the complex organization of cell interactions in the SVZ better than

histological sections[58]. Though LVWMs can be fixed and immunostained, time-lapse imaging of living tissue samples allows researchers to study dynamic processes such as motility and dispersion.

However, these studies are limited as images of live precursors of the SVZ can be difficult to acquire. In order to image the dynamics of SVZ niche function several considerations must all be addressed, including the curved structure of the tissue, the requirements for live cell imaging [66], and the limited time to capture acute images before cell interactions decrease as tissue condition degrades with time.

When drawn or modeled, the lateral ventricles themselves take the shape of large curved Cs, similar to the shape of rams' horns, one ventricle to each hemisphere with a third ventricle in the center between the other two. As Fiorelli, *et al*. [67] did an excellent job of modeling the mouse lateral ventricles, Figure 5-1 depicts a modified version of their Figure 4 for categorizing the structure of the lateral ventricles. Since the wholemount protocol requires peeling the medial wall away from the lateral wall, the structure of the wholemount takes that of the lateral wall and includes most of the dorsal wall, depicted in Figure 5-1 with the medial wall in green and the dorsal wall in red.

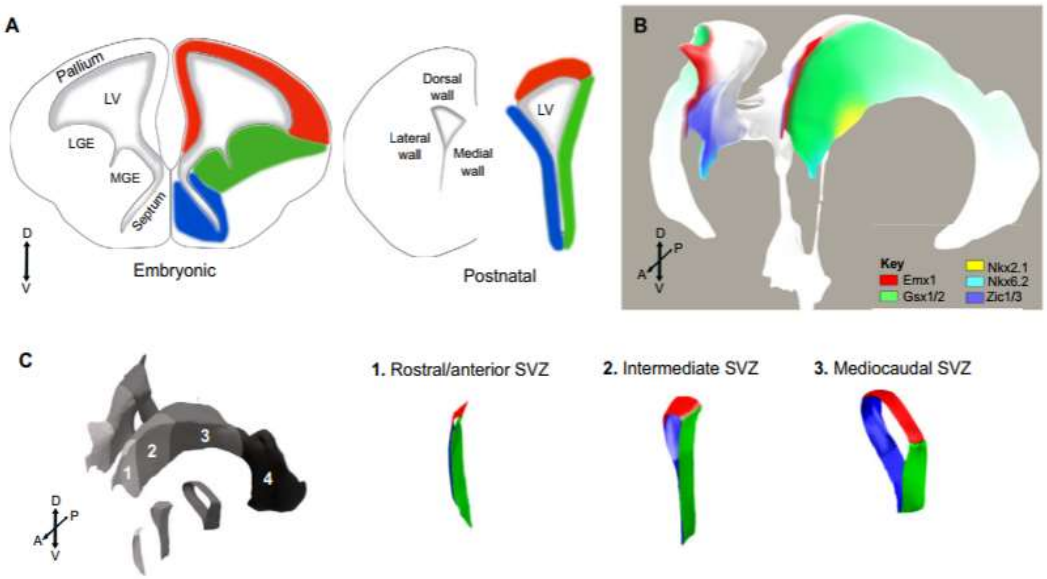

Figure 5-1: Modified images from Fiorelli *et al*, Fig. 4. [67] "(A) The V-SVZ walls (right) derive from their embryonic counterparts (left): the pallium, lateral and medial ganglionic eminences (LGE and MGE) and septum. Color-coding: red, pallium/dorsal wall; blue, septal/medial wall; green, ganglionic eminences/ lateral wall. (B) Fate-mapping studies… (C) A volumetric 3D reconstruction of the LVs is shown (top). Four anteroposterior subdivisions are illustrated by different shades of gray. Transverse sections of subdivisions 1, 2 and 3 with color-coded walls (red, dorsal; green, lateral; blue, medial) are shown." For our purposes, areas in green and red can be thought of as the curved wholemount cytoarchitecture to be imaged.

Figure 5-1 is also helpful in demonstrating the changes in structure as one views the lateral wall from areas C, 1 across to C, 3. It becomes easy to see how the green lateral wall shifts from a wide, almost flat area in Figure 5-1 C, 2 to that of a mirrored P as the dorsal wall becomes a larger part of the preserved wholemount tissue. Thus, the curved structure of the tissue refers not only to the horn-like curvature of the lateral ventricle but also to the changes in shape as the ventricle is imaged from the anterior to posterior direction, or vice versa.

Live LVWM imaging requires artificial cerebral spinal fluid (ACSF) or other medium immersion and fluid flow across the sample [46]. Due to fluid flow, LVWMs are

at risk of displacement and must be secured to prevent movement while imaging. Protocols suggest pinning [58] or adhesion, which inhibit imaging ability, as securing the tissue to a plate prevents tilting or repositioning the curved sample on the microscope. It can also introduce unwanted shear stresses to the sample, which can give an inaccurate impression of the tissue dynamics. Adhesion material can block access of tissue pockets to media that sustains the tissue, which hastens tissue degradation.

Keeping cells healthy, viable and behaving naturally in *ex vivo* requires planning for a microenvironment as close to *in vivo* conditions as possible. Though temperature of the dish and fluid flow can be controlled to elongate cell life-span, time-lapse imaging should be performed acutely, while astrocytes, which actively participate in astrocytic tube formation [68], still behave normally and cell migration factors are present. Therefore, it is suggested to limit studies using live tissue samples to within six to eight hours to assure that tissue is viable and cells are propagating and migrating [69].

There are many commercial tools available to keep cells and tissue viable while imaging. Since our goal for this work was directed toward tissue surface imaging and not tissue viability, it was decided that using a commercially available temperature controller from which fluid flow could be directed and to which our device could be attached was practical. It was assumed that the attachment part of such a peripheral device could then be changed to fit whatever standard microscope controller was employed. This allows the device to be more versatile across laboratories that may employ different viability control methods. Since two-photon microscopy is the “preferred method for imaging dynamic properties of living tissue” [46], the device was also required to fit and move on an upright microscope.

In a 2013 review by F. H. Gage and S. Temple [59], several foundational questions facing NSC researchers are discussed and the development of tools necessary to parse out these questions are listed in Table 2 of their paper (not shown here). Gage points out that 2D and 3D imaging tools for *ex vivo* imaging are desired and necessary for the advancement of questions relating to the static and dynamic interactions of NSCs within the SVZ.

Here, a novel imaging tool designed to facilitate a 3D *ex vivo* (wholemount) SVZ research is described. Due to its function of creating a more easily imaged plane from a curved tissue structure, it has been termed PICS for Planar Imaging of Curved Surfaces. This tool set addresses two common issues found when attempting live wholemount imaging of the SVZ: detailing the curved structure of its tissue and increasing the efficiency of imaging with such a structure, helping to preserve the dynamic relationships of the niche.

5.1 PICS Design

Our objective was to create a device that would stabilize the LVWM while allowing fluid flow around the tissue and facilitate rotation of the naturally curved LVWM with respect to the microscope objective lens for more efficient image capture. Three further considerations of the PICS device were as follows. First, that it should not add undue shear stresses to the sample tissue. Second, due to the curved nature of the lateral wall, the sample needs to rotate, but there should be no unintentional translation. Finally, it should attach to a standard microscope temperature controller in such a way that it does not interfere with temperature controls and does not move unintentionally.

To meet our objective, a design to place the center of mass at the point of the sample imaging plane about which a basket containing the sample could move was imagined. PICS parts were then created individually in SolidWorks®, with design iterations focused on the curvature of movement and basket stability to improve this strategy. The final PICS design consists of a 3D printed bottom plate (Figure 5-2, C) with clips (Figure 5-2, D), a machine milled basket (Figure 5-2, B), and a sample cap (Figure 5-2, A). The sample fits into the cap (A) and can be rotated radially. The cap is then placed into the basket (B) which rotates axially. Once individual designs were created, files were made into a full SolidWorks® assembly Figure 5-2, E.

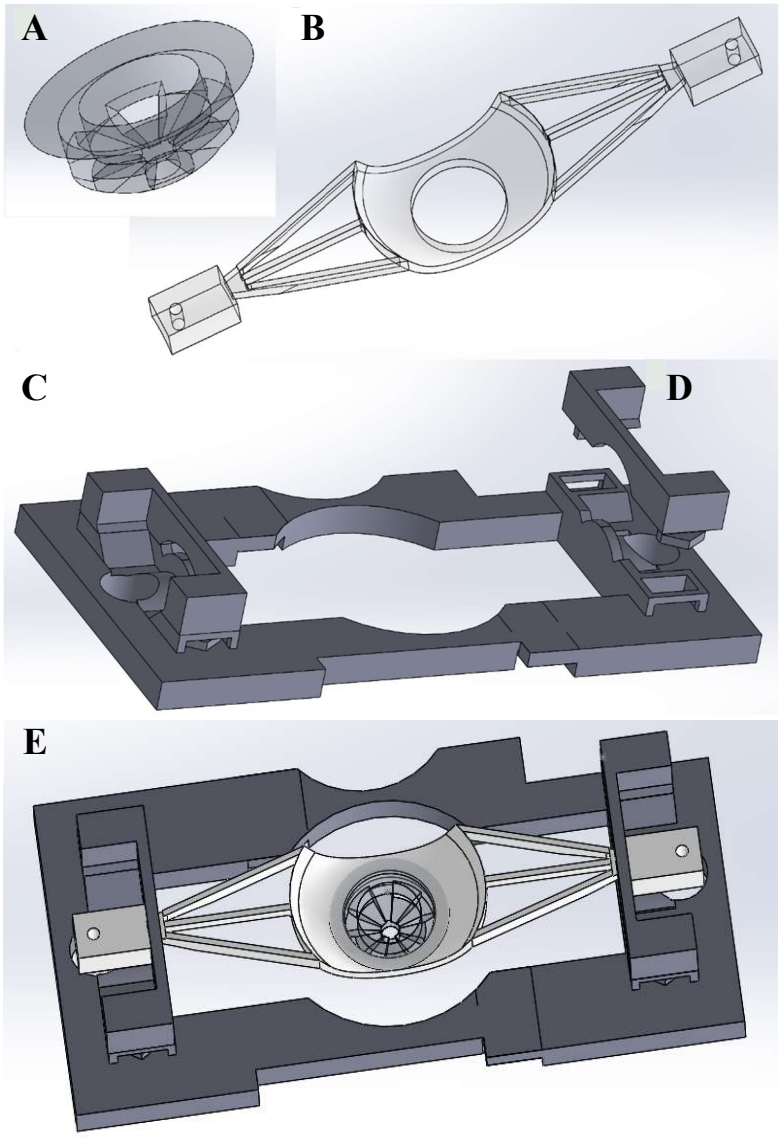

Figure 5-2: PICS Design. A. Tissue sample cap. B. Rotation basket. C. Plate designed to fit warming system. D. Clips to hold basket to plate. E. Entire SolidWorks® assembly.

5.1.1 Sample Stabilization and Fluid Flow

As mentioned in the first consideration, no added shear stresses should act upon the sample. Shear stresses can occur from pinning or adhesion of tissue as well as block access to ACSF. To prevent piercing the tissue or the need for adhesives, the inner structure of the cap was designed to slope downward, creating a depression that holds the

sample by gravity (Figure 5-3, A). A gentle slope of 22.6˚ from the center of the cap creates a five-pronged cavity, with an initial opening diameter of 10.5 mm and a final diameter of three millimeters. As the typical size of our mouse LVWMs ranged from 7 mm to 9 mm in length and 5 mm to 6 mm in width (measurements taken as samples lie on a ruler), the bottom hole was designed small enough that the wholemount would not fall through.

Fluid flows through small holes in the cap walls around the tissue (Figure 5-3), allowing for full immersion of tissue in ACSF. Since fluid flows up from the bottom of the cap to cover the tissue, there are no shear stresses from the flow of ACSF on the imaging face of tissue.

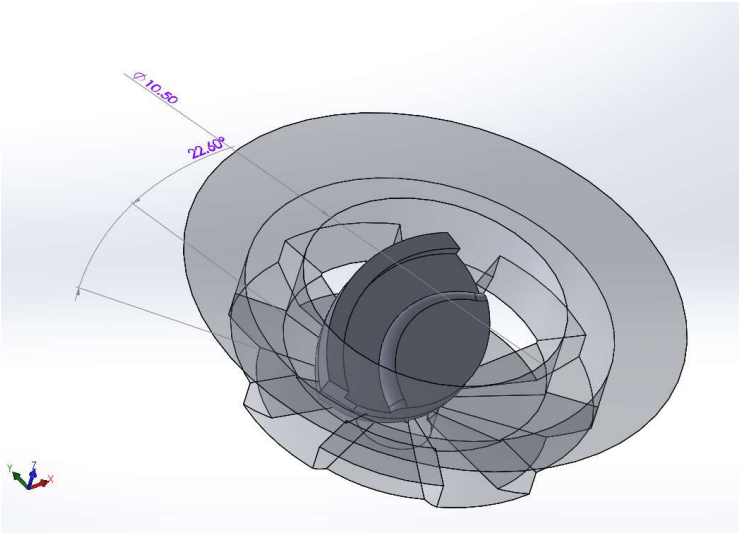

Figure 5-3: Cap Features and Sample Interaction. SolidWorks® dimensions for cap. Diameter 10.5mm; slope 22.6˚.

5.1.2 Designs for Sample Movement

The second consideration was that the sample needed to rotate to keep the curved structure of the LVWM in the image plane of the microscope. Key design criteria were that the PICS basket should rotate the curved LVWM structure but not produce incidental

translational movements. For tipping of the curved sample, an axial rotation archway scheme was devised (Figure 5-4). Since it is known that an unhinged body will rotate about its center of mass, care was made in construction of the parts to ensure the center of mass and therefore center of rotation would be at the top of the LVWM tissue sample, designated as the imaging plane. This was accomplished using the SolidWorks® center of mass tool, shown in Figure 5-4, A, along with the basket dimensions.

To create the arch along which the basket was designed to move, circles were made corresponding to the fixed center of mass point. Then lines were added matching the curvature of the cap bottom through the fixed imaging point to designated arc angles along the circle (Figure 5-4, B). The rotation archway in the bottom plate was drawn from these angles. Basket arms slide along the archway, tipping the sample while keeping the weight of the sample in the center to prevent lateral motion.

It was originally intended that the basket and cap were a single, solid piece designed to hold and rotate the sample. Upon building and testing, it was realized that the single piece would benefit from being made into two separate pieces. As one piece, the prongs of the single basket were much larger and endangered the sample to fall, getting stuck in the prongs. As two pieces, the bottom opening could be made much smaller, preventing the sample from falling through. This separation also allowed for radial rotation of the sample (Figure 5-12) which enhances imaging abilities. Thus, the two-part basket and cap design was adopted.

A

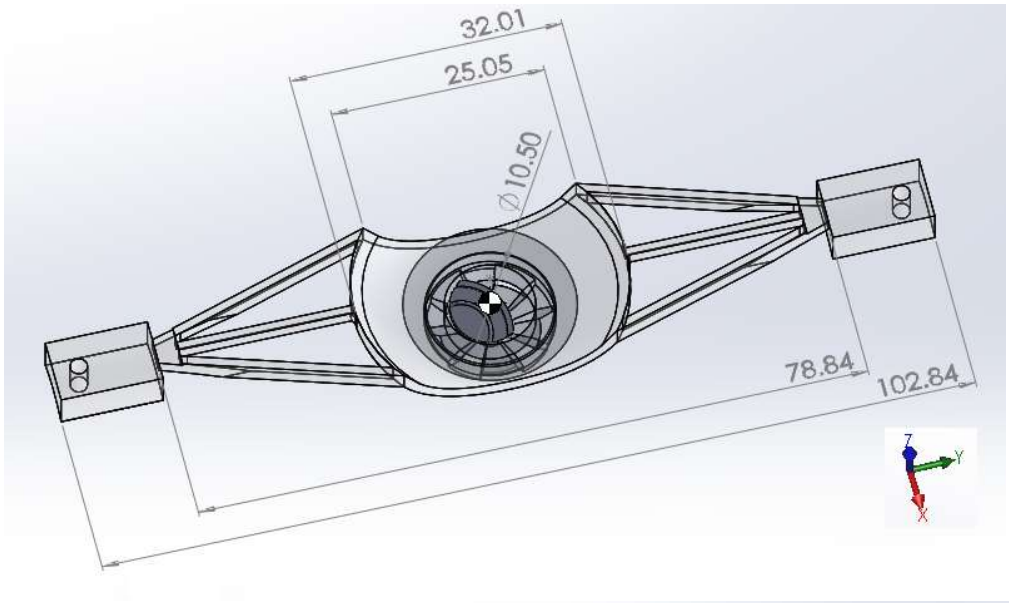

B

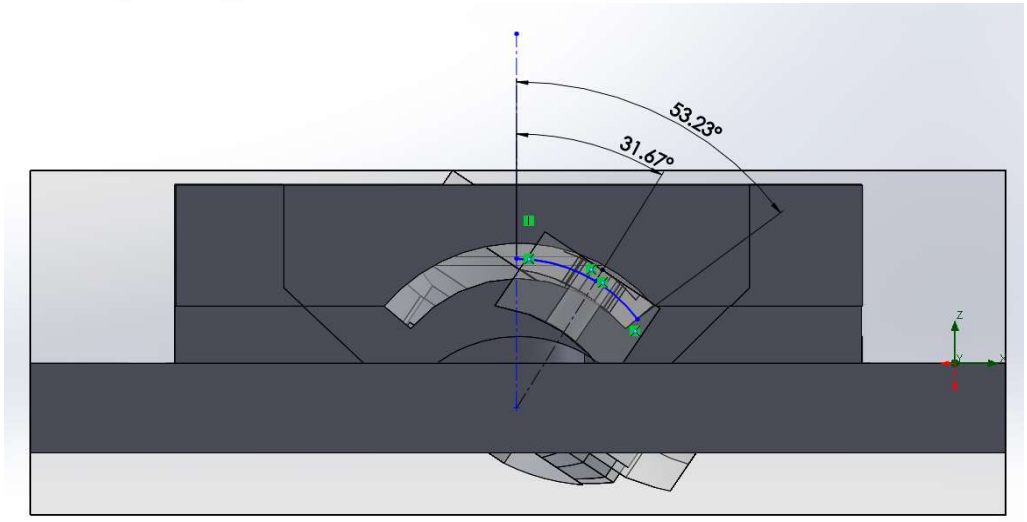

Figure 5-4: Basket Features. A. Dimensions of basket. B. SolidWorks® calculated angles of axial rotation for basket. ± ~32˚ from center.

5.1.3 Viability Control System Attachment

The final design consideration was that PICS needed to connect to a standard environmental controller in such a way that it did not interfere with the controller function nor easily fall off or be moved away from the viability enhanced environment

while imaging. A widely used controller, the Bioptechs Delta TC3 Culture Dish Micro-Observation Temperature Control System, was used to maintain the temperature of samples and direct fluid flow on the microscope. Bioptechs micro-environmental systems are commercially available environmental control systems for time-lapse microscopy. Thus, the 3D printed bottom plate was designed to fit over the Bioptechs system.

Since PICS could not interfere with the temperature or fluid flow controls, it was decided that a thin, open platform conforming to the preexisting Bioptechs structure was best. The Bioptechs system has screw posts connecting its two plates together to the left and right of the control dish. Since the baseplate would need to cover this area anyway, it was decided that surrounding the posts was a simple way to ensure attachment to the system preventing unintentional movement. Measurements of the Bioptechs system were made using a ruler and calipers. The SolidWorks® base plate was made corresponding to these measurements (Figure 5-5, A).

As shown in Figure 5-5, B, the 3D printed bottom plate and clips, fit into the Bioptechs micro-environmental control system as designed, allowing fluid flow into the temperature control dish over the machined basket and cap. It should be noted that the baseplate is a 3D printed part. It is assumed that such a part can be easily and quickly remade if necessary. Thus, having the SolidWorks® model, a baseplate can be designed to cover any other commercially available environmental control system by simply changing the dimensions of the plate. This makes PICS a versatile attachment, allowing for use across laboratories and controllers.

A

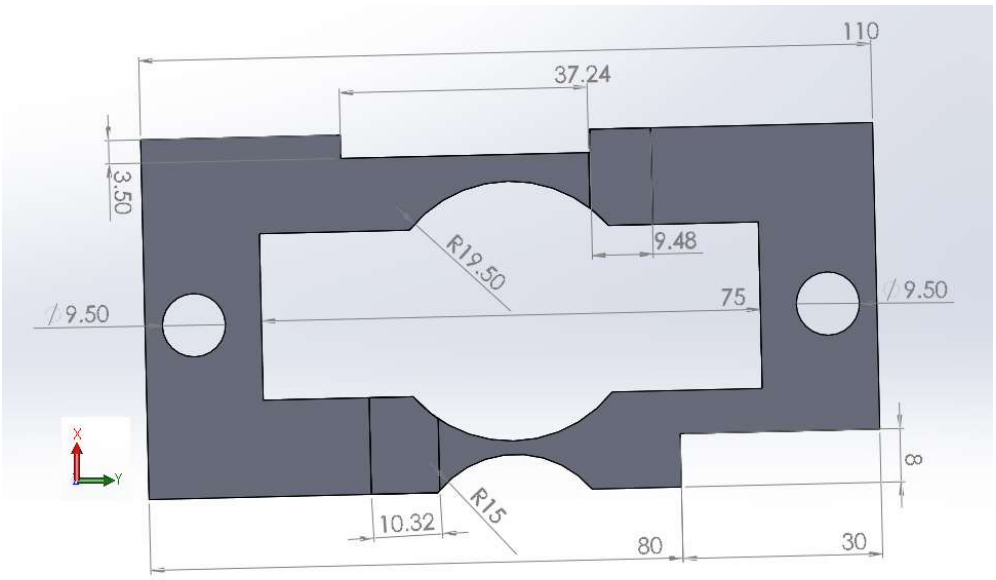

B

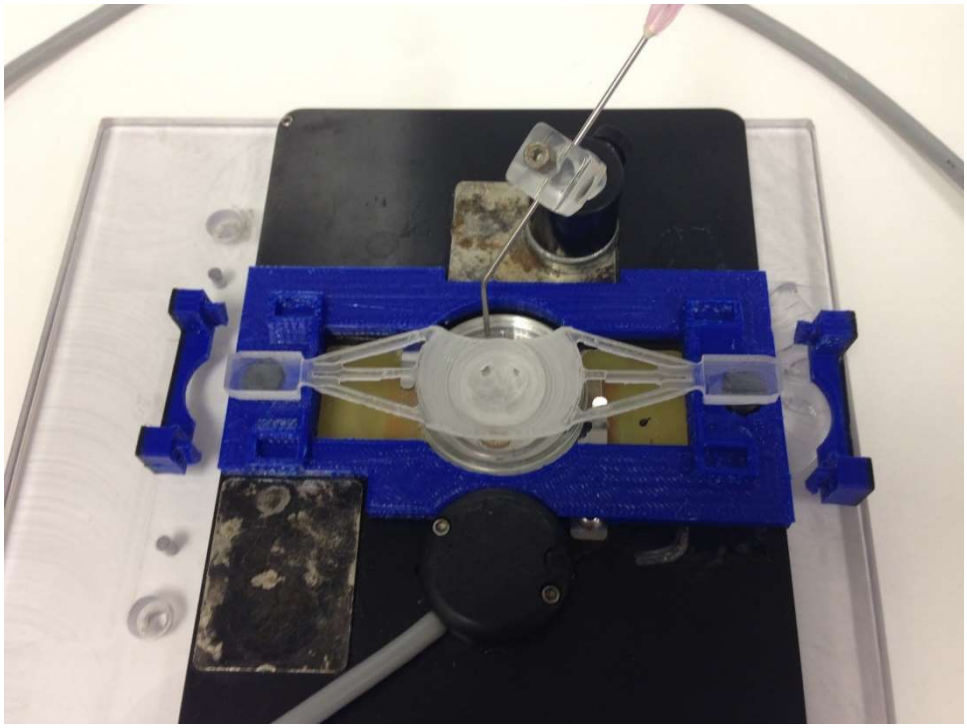

Figure 5-5: PICS in Environmental Control System. A. Measurements of baseplate. B. PICS fits as designed into commercially available environmental control system.

5.2 Materials and Machining Methods

Iterations of the device were completed using (1) outsourced milled nylon, (2) 3D printed polylactic acid (PLA) filament, (3) resin on a Formlabs Form 1+ printer, and (4) a 3D printed and milled combination, as depicted in Figure 5-6. Though much force was not expected on the device, materials were subjected to manually applied downward pressure and torque to assess general structural rigidity and expected endurance. One initial problem noted was the tendency of the basket to slide on one side and not on the other, causing torsion on the basket. Rigidity of the basket was important for simultaneous movement of both sides of the basket rather than one side. Though the nylon displayed great durability, outsourcing the milling was undesirable due to cost.

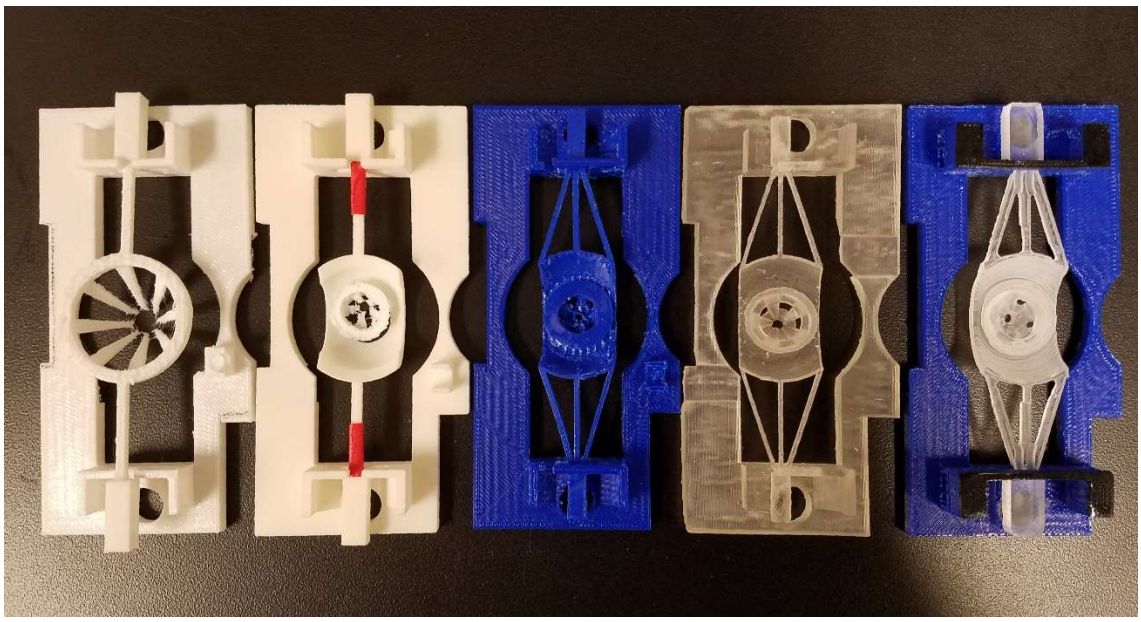

Figure 5-6: Iterations of PICS Device. From left to right: (1) Basket prior to two-part separation. (2) Nylon, outsourced material. (3) PLA after supports removal. See distortion of inner basket and cap. (4) Resin. (5) Final two-part PICS; basket and cap milled, baseplate and clips printed.

All 3D printed parts were created using a MakerBot® Replicator 2X 3D printer using PLA filament. The PLA was rigid and durable; it is still used for the baseplate and

could have been used for the basket and cap. However, it was very difficult to remove the supports from these parts to get the original desired design since we only had access to one printing extruder. Pieces of the archway needed to be completely clear of debris to allow the basket to slide smoothly along the archway without sticking or breaking away. Also, drilling or sanding out undesired supports caused archway distortion, which led again to basket sticking or torsion. It was this design characteristic that led to clips being used to secure the basket to the plate rather than the earlier design of basket entry.

It is possible that if two extruders and the dissolvable HIPS filament could be used, that fully 3D printing this device could be advantageous. Three-dimensional printing the parts was also the most time and cost efficient of the prototyping methods we employed. If a single prototyping method is used, the maker does not have to be familiar with both milling and rapid prototyping methods. As we only had access to a single extruder and the shaping of parts was extremely difficult due to supports, we next chose to resin print the basket and cap.

After testing, it was determined that though basket and cap files could be created using resin printing means, the material was not stiff enough, or needed to be made much thicker. The basket and cap combination benefitted from the rigidity of a more robust material such as polycarbonate (PC). Thus, the end result of these iterations was a 3D printed PLA bottom plate and milled PC basket and cap combination.

5.2.1 Computer Numerical Control (CNC) Machining

To mill the basket and cap, a CNC was utilized. CNC machining uses computer programs to finely control machine tools. Similar to 3D printing, a G-code, or G programming language, for toolpaths must be created for CNC milling. Unlike 3D

printing, a separate computer-aided manufacturing (CAM) program is needed to create toolpaths and formulate G-code. Figure 5-7 displays the toolpath created when the PICS design was imported into our chosen CAM program, Autodesk® Fusion 360™, a 3D cloud-based computer-aided design (CAD)/CAM/computer-aided engineering (CAE) program.

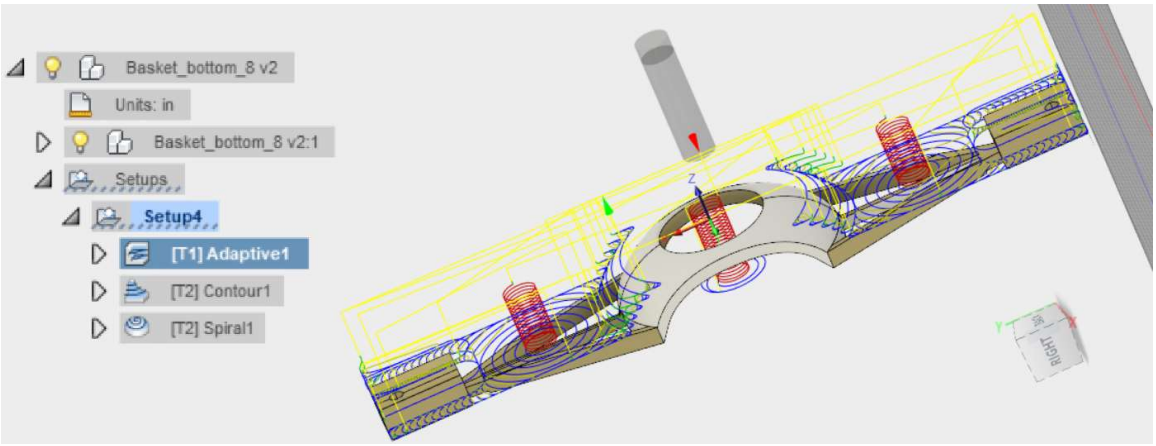

Figure 5-7: Fusion 360™ Toolpath Model. Left: lists three individual paths taken to create model. Right: projected toolpath for first of three paths.

Basket and cap files were converted to STL and placed into Fusion 360™, where the CAM models, the toolpath, and G-code were created as seen in Figure 5-7. We used the tool library to create a bit the exact size of those we had available. One advantage to running the full milling toolpath in Fusion 360™ is that trouble areas can be spotted and accounted for. When the program's toolpath was run, it became apparent that the smallest bit we had, two millimeters in diameter, was too wide to shape the arms to the exact size originally designed. For this reason, light redesigning of these features in CAD with special attention to proper center of mass, was made. It can be seen in Figure 5-6 that the milled basket arms are slightly larger than the PLA or resin prints. This increase in size

directly affects the arc length that the basket is able to travel over the archway, however upon testing, the extra length was unnecessary, as described in the discussion section.

The G-code was then transferred to PathPilot®, the controlling system software created by and for Tormach Personal CNCs (PCNC). When milling anything that has both a top and bottom (or front and back) face, care must be taken to set the path beginning from an origin that can be easily identified on the physical face of the stock. While this is done in the CAM program during G-code creation, it is imperative that the exact stock origins are followed through with during milling. If proper care to set origins to physical stock placement is not observed, the faces of the object being milled are likely to be mismatched, creating an unusable part and expending more stock than necessary.

The basket and cap were milled out of PC stock using a Tormach PCNC 770 according to the G-code created in Fusion 360™ (Figure 5-8). Simple manual milling modifications were made to the cap to ensure holes were wide enough for fluid flow and to basket arm height to ensure fit into baseplate.

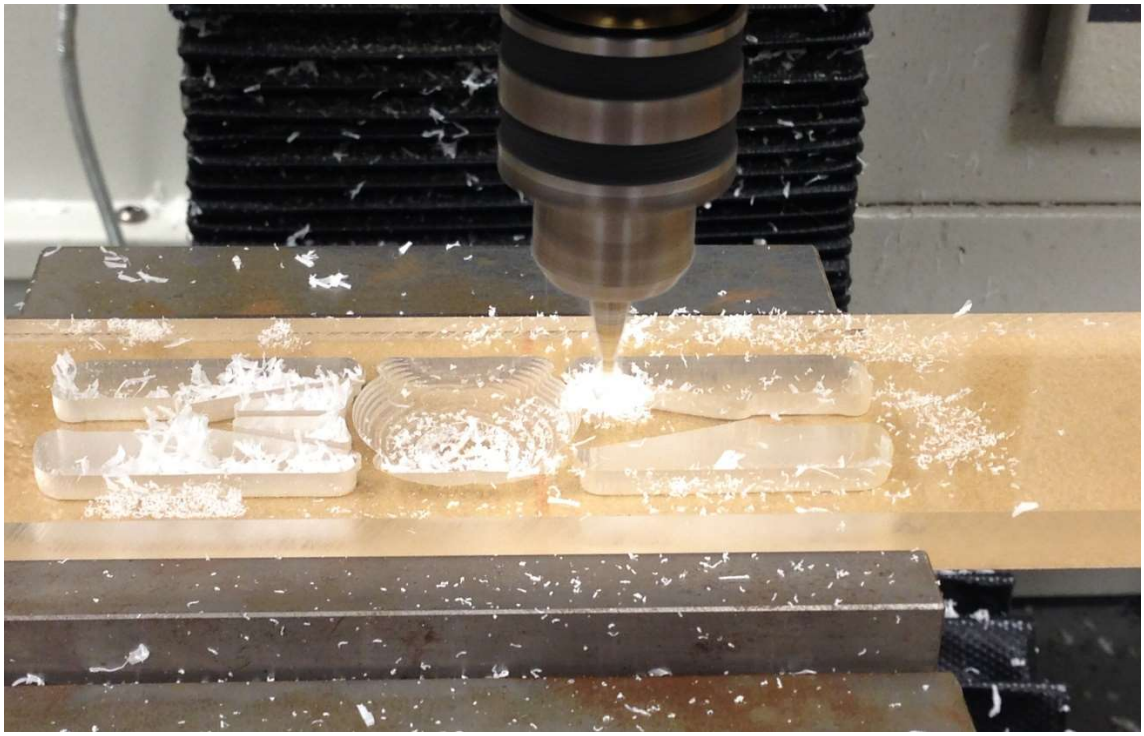

Figure 5-8: Milling the Basket from PC Stock. Smallest bit available 2mm diameter. Some features larger due to milling bit size.

5.2.2 SVZ LVWM Preparation and Imaging.

To perform an imaging experiment, the Bioptechs system, the PICS device, and fluid pump controllers were placed on the microscope prior to tissue extraction, as seen in Figure 5-9. The center of the PICS basket was placed directly underneath the dipping objective, then tilted toward the front of the microscope to remove the PICS cap. The PICS cap was then placed beside the stereomicroscope for later placement of the tissue sample, and ACSF was prewarmed to ensure correct temperature.

PICS adds1.3 cm to the Bioptechs system, which makes the entire arrangement only two centimeters high on the microscope. Thus, additional microscope stage modifications are not required.

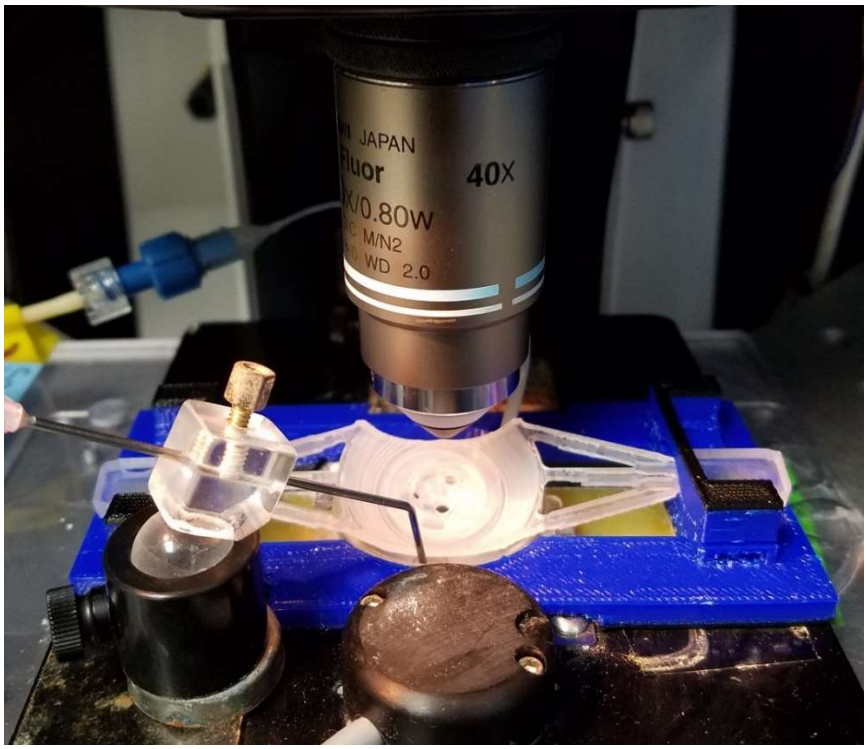

Figure 5-9: PICS Setup on Microscope Stage. Ample room for PICS underneath objective.

Since images of vasculature were desirable as landmarks, Texas Red-Dextran was employed for vascular staining. Prior to cervical dislocation, mice were injected in the lateral tail vein following the protocol found in Appendix B.2. Three minutes after injection, LVWMs were extracted from two to six-month-old STOCK Tg(Gad2-EGFP)DJ31Gsat/Mmucd (RRID:MMRRC _011849-UCD) transgenic Gad2 promotor targeted mice. Gad2 is a gene that encodes glutamic acid decarboxylase, a 65KDa isoform, and is found in both Pancreatic Islets and the Brain. In the brain, Gad2 enzymes convert glutamate to GABA. In LVWM imaging, Gad2 is used as a marker for neuroblasts, since in the SVZ and RMS neuroblasts transcribe Gad2 [70].

Extraction was completed following the Mirzadeh *et al*. protocol found in Appendix B.5. [58]. Briefly, mice were sacrificed and brains extracted. Using a

stereomicroscope, the medial wall was retracted from the lateral ventricle and cut away. Overhanging cortex and thalamus were removed to give clear view of the lateral ventricle. The final LVWM has a seashell shaped curvature with the ependymal layer facing up.

After dissection of the LVWM was complete, the LVWM was placed immediately into the PICS cap, which was then transferred into the prewarmed, oxygenated ASCF waiting on the microscope. Cap and tissue sample were placed into the basket, then rotated radially to acquire desired imaging section. The basket was axially rotated when necessary to acquire curved surface images.

Images of LVWM tissue were obtained using a Vivo™ Two-Photon Microscopy Workstation (3i) with both red and green channels. A Leica 40x dipping objective was employed to obtain detailed images of neuroblasts and surrounding vasculature. In some instances, time-lapse imaging was used to capture migration. Imaging sessions were limited to one hour after brain extraction.

5.3 Results

5.3.1 Summary of Performance

The PICS device has been used to test over 15 samples in our laboratory and has not needed any repairs or revisions. The machined basket and cap provide versatility in sample positioning during imaging, as desired. Samples are stable, being able to undergo imaging without unnecessary refocusing or repositioning. Since a dipping objective is used, it is assured that the sample is continually immersed as the lack of fluid would cause resolution to decrease. This is not observed in our imaging sessions, as the crisp focus of images attests.

Tissue repositioning for curved imaging can be accomplished with radial rotation of the cap as well as axial rotation of the basket. Using PICS instead of attaching a sample to a flat plate also allows for the tissue itself to be moved inside the cap during breaks between imaging, if necessary. The entirety of the LVWM can be imaged using PICS, and time-lapse studies for migration are possible.

5.3.2 Describing PICS Capability

The slope in the depression of the cap was considered successful through evidence of sample stability in the device. Sample stability was judged as seen upon observation and as imaged through the objective. The sample should fall into the depression and remain there without tipping or moving laterally, allowing the seashell shaped curvature of the LVWM to open toward the objective without falling through the cap or getting trapped in the sides of the cap. There should be no unintended lateral movement during fluid flow or microscope use. Fluid should be able to completely cover the sample.

Figure 5-10 depicts the observed LVWM sample stabilization in the cap with fluid flow. The cap allows fluid to flow through the holes in the cap walls (Figure 5-10, A). During tests, no visible tipping or lateral movement of the sample due to fluid flow after one hour of continual ASCF flow was observed. Upon axial or radial rotation, the sample does not fall through the bottom of the cap, nor does it stick to the sides of the cap.

Our dipping objective has a working distance (WD) of 2.0 mm, requiring a well deep enough both to hold the volume of sample and allow for the full range of the WD

for clear images. Full immersion of the sample takes place, allowing the microscope dipping objective to sit in the fluid (Figure 5-10, B) while taking images.

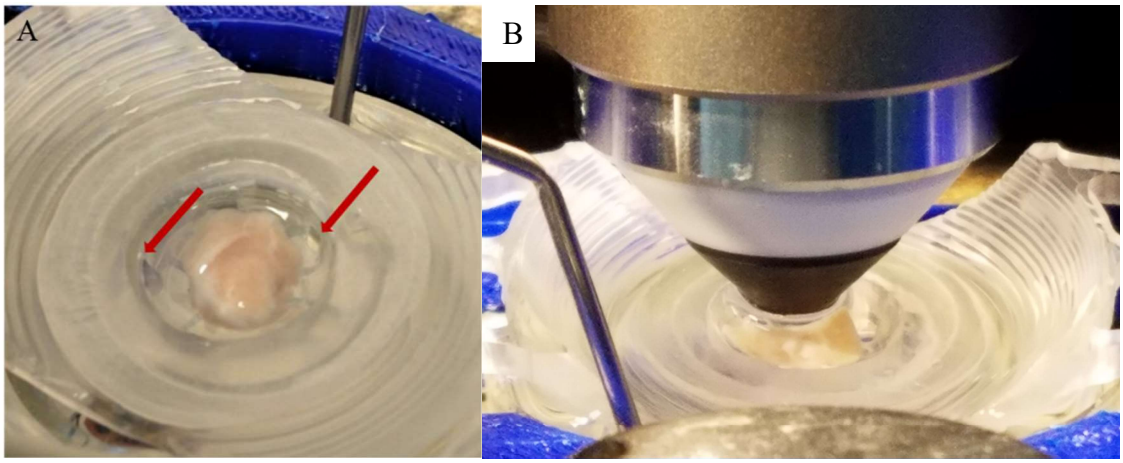

Figure 5-10: Sample Interaction. A. LVWM fits into sample cap and remains in place with fluid flowing (arrows show direction of flow). B. Dipping objective sitting over sample. Full immersion sustained; 40x objective. 2.0 WD.

Image sets show that there is no unintended lateral movement during microscope use of PICS. Figure 5-11 shows a Z-stack taken using the device. It is expected that if the sample itself was moved during imaging, disruptions in the continuity of the Z-stack would appear as the objective automatically changes position. All images are clear, in focus, and the z-stack does not seem to drift. Images are high in detail, sharply displaying branches in vasculature and roundedness of neuroblasts with some cells having distinct extended leading or trailing processes. Contrast between red and green fluorescence is distinct with little to no overlap. The large vessel to the lower left corner becomes more apparent as the Z-plane moves the structure into view, yet the structure itself does not move sharply in any direction as would be expected with sample movement.

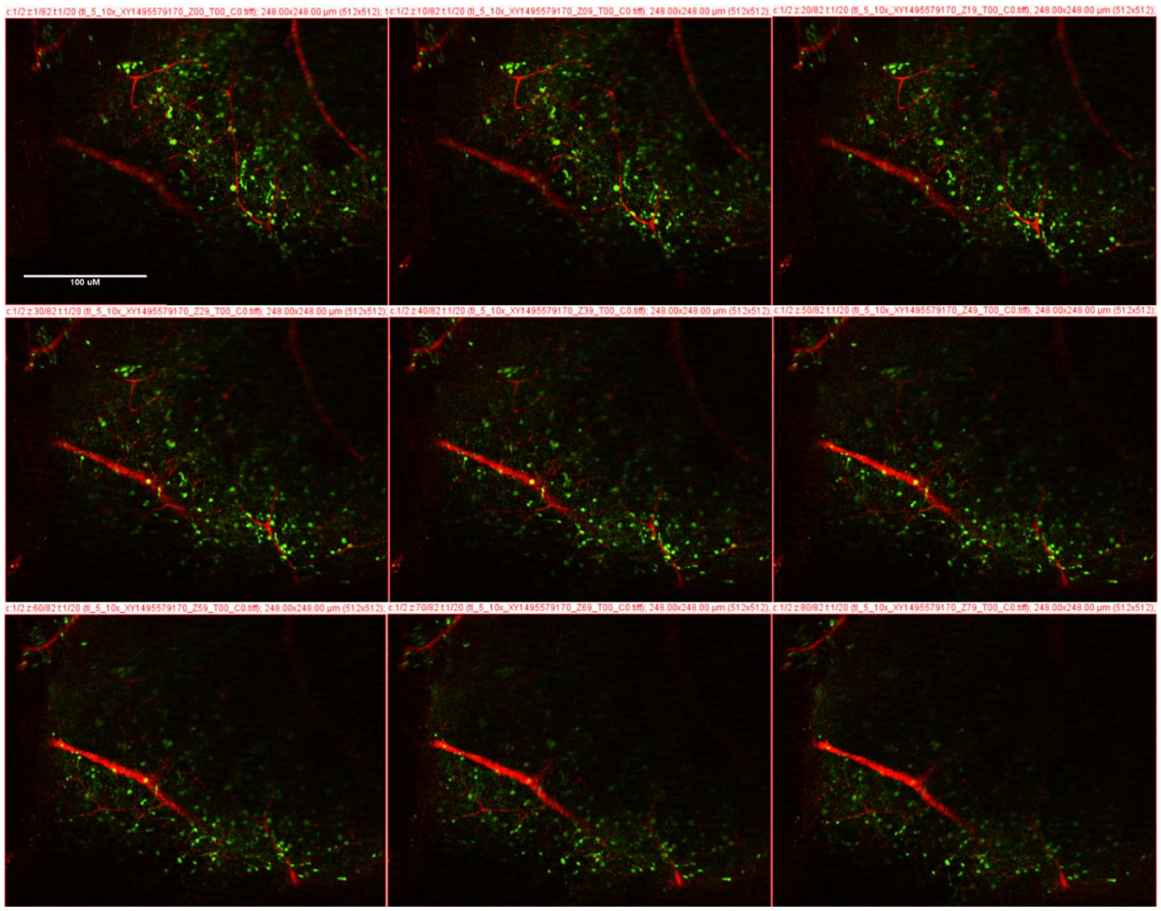

Figure 5-11: No Lateral Movement During Imaging. 80um Z-stack using PICS; 40x Objective. Red is vasculature. Green are neuroblasts under Gad2 promoter.

Radial rotation of the sample allows for simple repositioning and is achievable via forceps to the cap as depicted in Figure 5-12, A. The sample remains visibly stable inside the cap as the cap itself is turned. Clockwise or counter-clockwise rotation is possible.

Once the tissue is set correctly into the depression, it is most efficient to ensure that the tissue sample itself does not have to be readjusted within the cap. However, if angled views beyond radial or axial rotation are necessary, the sample itself can also be moved during breaks in imaging (Figure 5-12, B-C) because it is not glued or pinned. This is an extremely beneficial aspect of using the cap. There is no need to attempt

removing adhesive or unpinning the sample. Forceps quickly reposition the sample, which can then be adjusted radially or axially using the basket and cap.

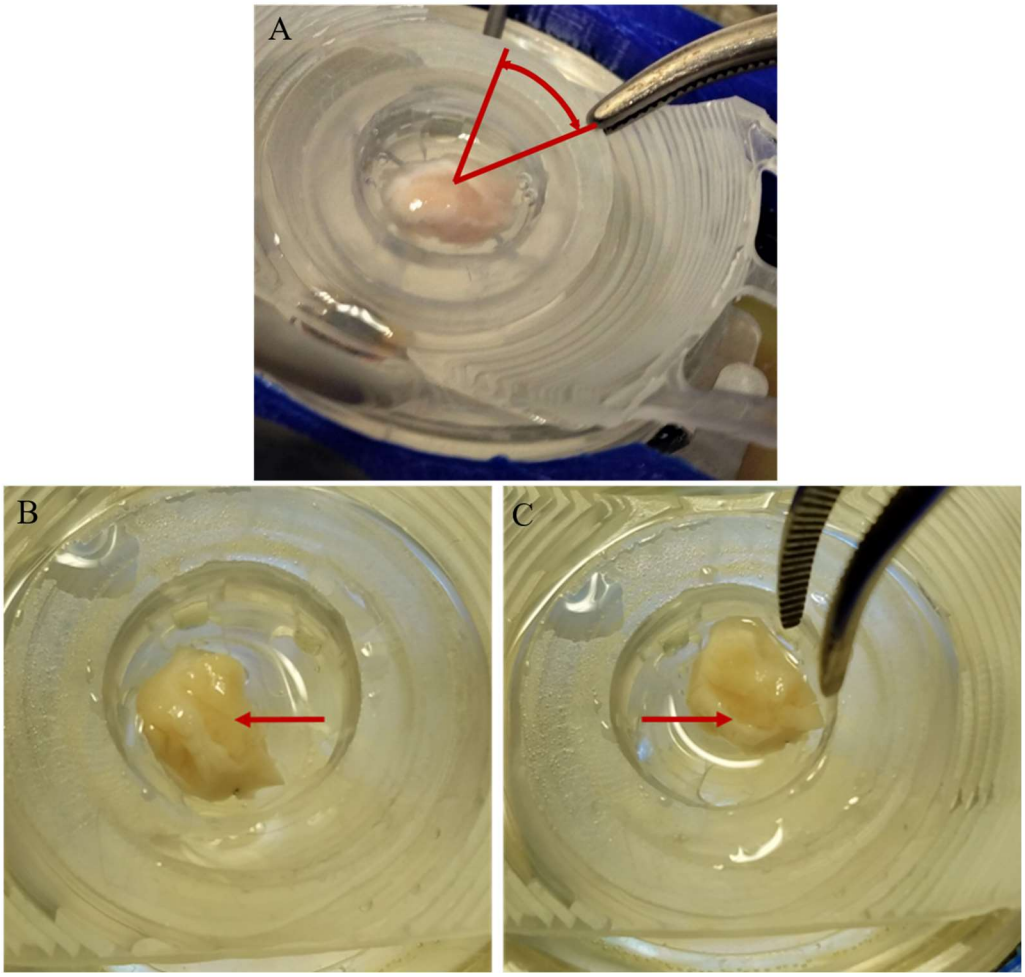

Figure 5-12: Further Sample Interaction. A. Radial rotation of sample cap using forceps. B-C. Tilting the sample itself to allow for angled views. Arrows indicate area of focus: inner and outer curvature.

Axial archway rotation was tested by sliding the bask*et al*ong the archway and actual degree of tilt was measured using a protractor (Figure 5-13). Though the model intends ±32˚ from center, the axial rotation of basket is ±16˚ from center (Figure 5-13, A), full rotation ~ 32˚. Limited rotation is due to precision of milling bits upon milling used for producing the basket arms. The basket rotates smoothly along the plate arch

while clips secure the basket to the plate (Figure 5-13, B). Insignificant translational movement of the sample was observed during axial rotation.

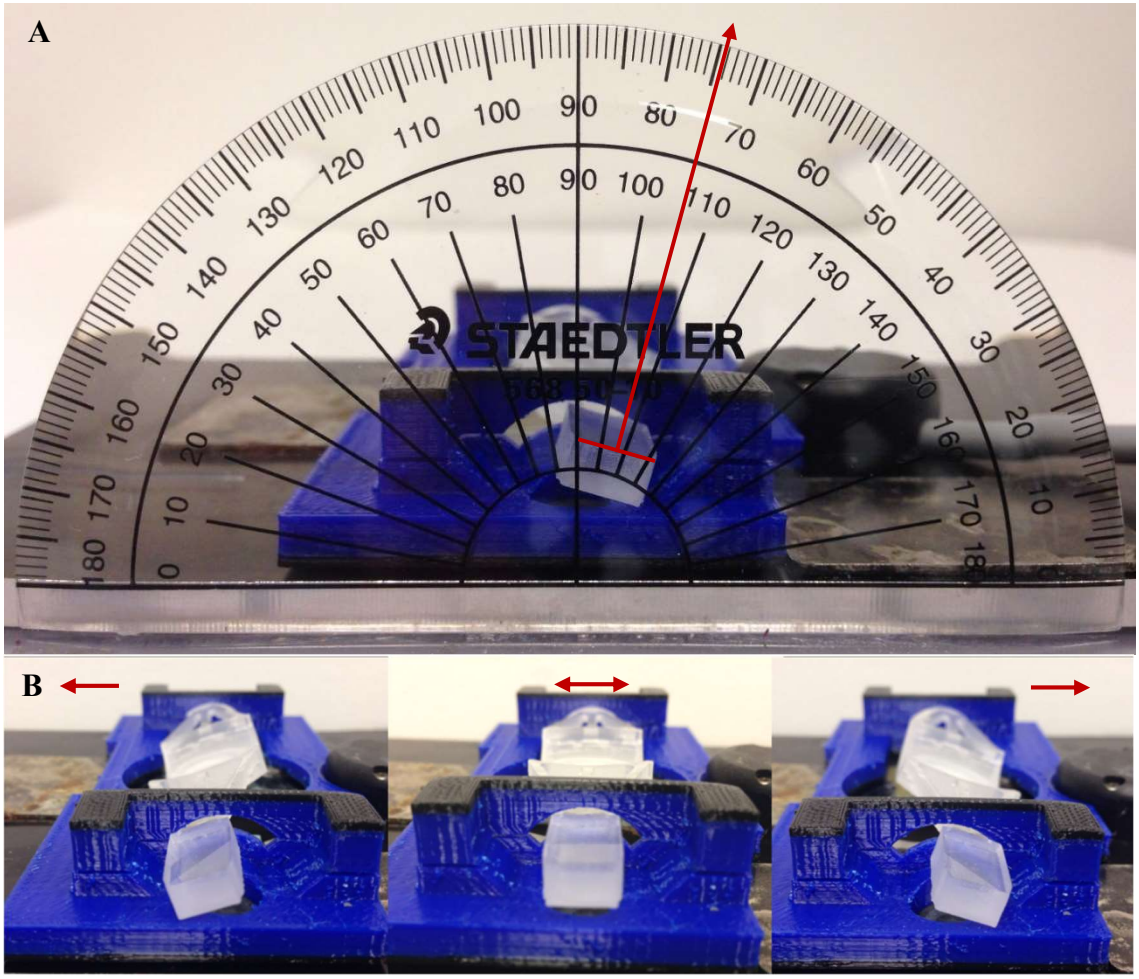

Figure 5-13: Basket Axial Rotation. A. Side view of machined device showing angle rotation. ±16˚ B. Smooth rotation along archway without torsion: left, middle, & right.

Multiphoton images of the lateral ventricular wall were taken using the device. A mosaic using Fiji's Stitching plugin [71] was created from images to show the full span of a typical LVWM (Figure 5-14). Fourteen images were combined to produce a mosaic view of the cytoarchitecture of the SVZ. Highly detailed images of the LVWM can be taken using PICS, as the extracted image of the rostral portion of the SVZ shows.

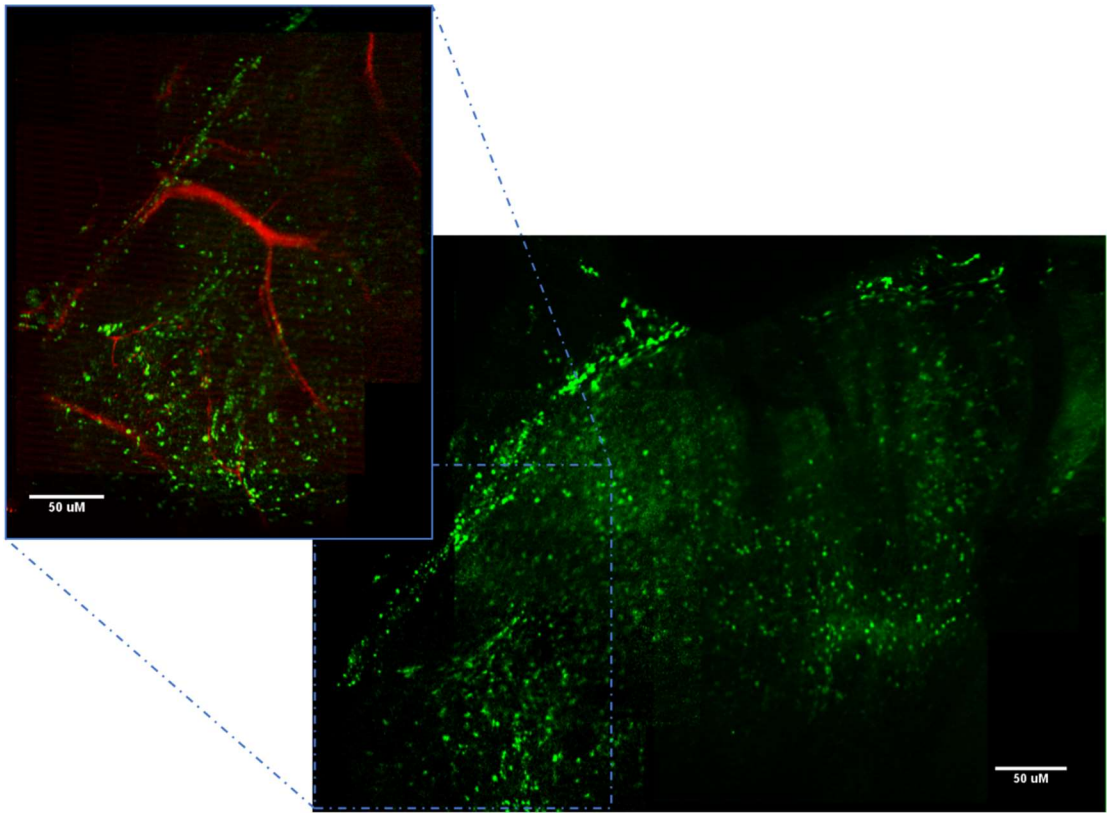

Figure 5-14: Mosaic of Entire LVWM. 14 tiles complete the entire curvature of the SVZ image in green (GFP under Gad2 promoter). 10 tiles complete the more detailed view (blue box) with counterstained vasculature. 40x objective. Stitching, a Fiji plugin, was used to create mosaics.

5.4 Discussion

Studies involving live LVWM imaging involve time constraints as the sample degrades and cells become less motile. Curved tissue, such as the LVWM, can be especially difficult to manage since securing the tissue to a plate prevents tilting or repositioning the curved sample on the microscope. We have developed a device, PICS, to allow for sample tilting and rotation while imaging to increase imaging efficiency.

The PICS device machines and prints according to models. It rotates axially along 3D printed archway for a tilting arc of ~±16° from center and also rotates radially to reposition the sample with the simple use of forceps. It fits a standard microscope

temperature controller. The device also allows fluid flow and sample immersion through holes designed in cap wall, ensuring that samples receive necessary nutrients, oxygen, and buffering for maximal survival time.

PICS stabilizes the sample by containing it in the cap's depression. Using the depression method allows curved LVWM samples to be further opened for imaging while not gluing or pinning the tissue, preventing further movement or stress to the sample. It also performs as necessary to capture desired images of WMs and SVZ niche. PICS easily manipulates a curved tissue sample to provide angled imaging views.

With the proper tools, PICS can be easily printed and machined for use in other laboratories where imaging of curved tissue, especially wholemount imaging, is necessary.

CHAPTER 6

REVIEW OF NEUROTRANSMITTER KINEMATICS AND ELECTROCHEMICAL SENSOR METHODS

6.1 Glutamate as a Neurotransmitter

Glutamic acid, $C_5H_9O_4N$, is a nonessential amino acid. Loss of one proton in glutamic acid results in the anion glutamate, also known as monosodium glutamate or MSG when referring to dietary additions. Glutamate is the common form of glutamic acid in the body. It is also the most abundant free amino acid form found in the brain and the most prominent excitatory neurotransmitter in the mammalian CNS [72]. As such, it plays an important role in normal synaptic function.

Normal neurotransmission in a glutamatergic synapse follows the excitation pathway expressed in Figure 6-1. When the glutamatergic presynaptic neuron is stimulated, it will release glutamate into the extracellular space of the synapse where both the receiving (postsynaptic) neuron and the regulatory glial cell have access. There are several glutamate receptor (GluR) protein families, located mainly on the neuron, which bind to glutamate to perform a variety of functions on the postsynaptic neuron, including depolarization.

GluRs are classified as “N-methyl-D- aspartate (NMDA) receptors (Gonda 2012; Bonaccorso *et al*. 2011; Santangelo *et al*. 2012), AMPA

(a-amino-3-hydroxy-5-methyl-4-isoxazole propionic acid) receptors (Rogawski 2013), kainate receptors (Lerma and Marques 2013) and metabotropic receptors (Gregory *et al*. 2013)" [73]. Rates of GluR activation differ between receptor families, with AMPA being the fastest responders. In presynaptic terminals, glutamate is housed in vesicles, which are released by a Ca^{2+} dependent mechanism [74]. It is estimated that each vesicle contains a concentration of approximately 100 mmol/L while the synaptic cleft itself maintains a concentration of approximately 2-1,000 μmol/L [72]. It follows, then, that glutamatergic neurotransmission is controlled by glutamate concentrations in the extracellular fluid of the synapse. As vesicles filled with glutamate are released, the concentration of glutamate within the synapse must be depleted quickly to prevent overexcitation of GluRs, as this leads to neuronal damage and death, also known as excitotoxicity. However, because there are no enzymes in the extracellular fluid to remove glutamate from the synapse, free glutamate must be removed from the extracellular fluid through diffusion and cellular uptake [75].

A

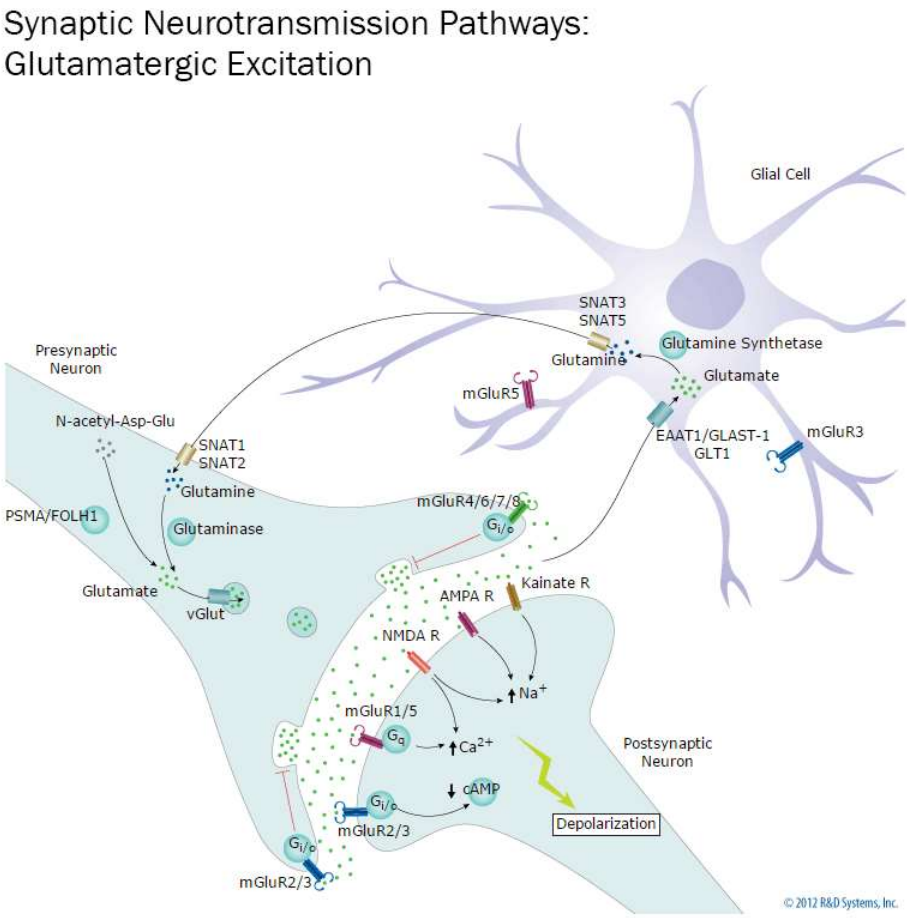

B

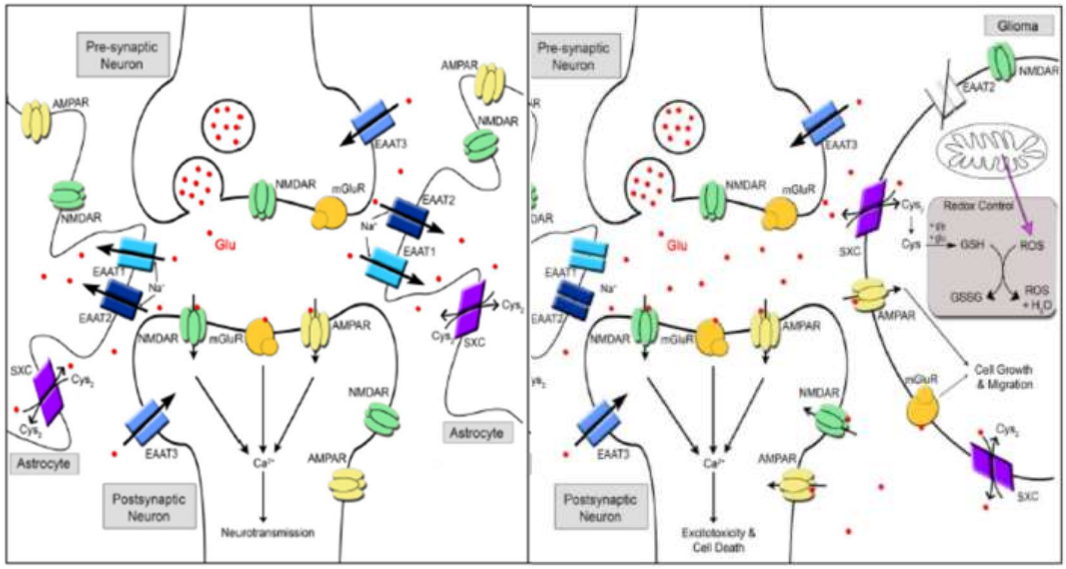

Figure 6-1: Glutamatergic Synapse Neurotransmission. A. Normal Glu synapse. Reprinted from R&D Systems, Inc. [76] B. Normal Glu synapse versus impaired glioma synapse. See downregulation in EAATs in glioma, reprinted from [77].

6.1.1 Glutamate Transport and Kinetics

Cellular uptake is performed by glutamate transporter proteins which move glutamate across the neuronal and glial membranes, and thus regulate extracellular glutamate concentrations in the synaptic cleft. Transporter families, seen in Figure 6-1, include EAATs (excitatory amino acid transporters), VGLUTs (vesicular glutamate transporters), and the glutamate/cystine exchanger System x_c^- (SXC). Much work has been done using glutamate transporter cloning (cDNA) [72], [78] to assess transporter structure and function. Five clones of plasma membrane transporter subtypes have been made, and to avoid confusion, it should be noted that transporter subtypes are often referred to by their clone names. Thus, EAAT1 is also often referred to as GLAST (glutamate aspartate transporter) [79], EAAT2 referred to as GLT-1 (glutamate transporter 1) [80], and EAAT3 referred to as EAAC1 (excitatory amino acid carrier 1) [81]. Primarily, EAAT1,2 are found on glia and EAAT3-5 on neurons.

Total brain glutamate concentrations are estimated at 10 uM in cerebrospinal fluid and three to four micromolar in extracellular fluid [82]. For extracellular glutamate concentrations, there are three ways that uptake can occur: first, through reuptake by the presynaptic neuron, second, through uptake by the postsynaptic neuron, and finally, through glial uptake. According to the review by Robinson and Jackson, “the bulk of glutamate clearance in the brain is mediated by the astroglial pools of GLT-1 and GLAST [a.k.a. EAAT 2,1]” [83], asserting that astrocytes are the primary cells responsible for ensuring rapid glutamate uptake from the extracellular space.

The glutamate transport cycle was organized by Grewer *et al*. into four steps: “the glutamate-binding step, the transition to the anion-conducting state, the

glutamate-translocation step, and the formation of a glutamate-independent anion-conducting state" [84]. Different transport subtypes vary in their speeds of the above steps, causing dynamic kinetics and a range of time in which glutamate concentrations are cleared [85].

Transporters bind glutamate very quickly, within microseconds [84], [86], with subsequent steps being slower. After binding, the transporter enters its transition state in which it alters shape (conformational change) to allow transportation. There is also a chance that glutamate will release from the transporter and diffuse back into the extracellular space after binding. According to Vandenberg, "The capture efficiency for EAAT1-3 is ~0.5, which means that glutamate has an equal chance of unbinding as being transported" [78].

In the second step presented by Grewer, the transporter enters into an anion conductance state. Transport is electrogenic, changing the cell's electric potential. In the late '90s, Levy *et al*. confirmed through the cloned GLT-1 that transport moves $3Na^+$ and $1H^+$ in co-transport as well as counter-transport of K^+ [87]. Thus, for each completed transport cycle two net positive charges move into the cell, presenting an inward current, often referred to as uptake current or coupled transport current [88]. Transport of Glu against a large concentration gradient is powered through the Na/K-ATPase, which maintains ion gradients necessary for proper function of the transporter [89].

Transporters also facilitate an anion current, sometimes called uncoupled anion current, since it is uncoupled from glutamate movement. Initial anion conductance happens upon glutamate binding and the conformational change of the transporter.

However, the glutamate accumulation is “neither dependent on anions nor affected by the direction of anion flux” [90].

The third step is actual glutamate translocation, and the translocation of the aforementioned Na^+, H^+, and K^+ ions. It is proposed that reactions of the K^+-dependent branch are the rate-limiting step [88]. For EAAT1-3 transporters, glutamate transport times are estimated at 10-50 milliseconds [90]. According to Gamerio *et al*, 2011, it takes approximately 300 milliseconds for glutamate movement across the membrane.

6.2 Electrochemical Sensors for Neurotransmitter Study

Due to the importance of Glu as a neurotransmitter, there have been numerous studies exploring Glu signaling using microelectrodes and implantable probes as methods [91]–[95]. The most commonly used devices have been microdialysis probes, carbon fiber microelectrodes (CFMEs) as hydrogel-coated microsensors, and microelectrode arrays (MEAs). Each type of probe has its own advantages and disadvantages, as there are many aspects of probe design necessary to consider when developing a long-term implantable microelectrode to test neurotransmitter dynamics. First, neurons are small in size, so neurotransmitter probe must also be small, preferably on the order of one to 10s of microns. There is also a low concentration of Glu (approximately 10uM average in the human brain); thus, a Glu probe must be highly sensitive. Due to the presence of other transmitters and molecules in the brain, such as dopamine and glucose, it also must be highly selective. Finally, Glu dynamics are in the sub-millisecond range. Probes should be able to measure small fluctuations in the millisecond range.

Microdialysis for neurotransmitter study was originally developed by Ungerstedt and Pycock in 1974. It is a very sensitive analytical technique for neurochemical

measurement and is “well suited to follow basal levels [of neurotransmitters] and the slower and smaller changes in concentration that occur during behavior and in response to pharmacological manipulation” [96]. It samples the extracellular fluid and collects it for recovery from the body, making it accessible for analysis. It can also be used with “living, awake and freely moving animals” [97]. Microdialysis has been used extensively to study neurotransmitter release, although it has been questioned if the dialysate recovered relates quantitatively to synaptic release [97].

Uncertainty of physiological origin in microdialysis is problematic in long term Glu detection. According to Oldenziel, *et al*. in 2006, “glutamate detected by microdialysis does not fulfil the classical release criteria for exocytotic release as it does not show calcium dependency or response to sodium channel blockade. Detection of extracellular glutamate with a higher spatial and temporal resolution is apparently required to facilitate sampling of the synaptic pool” [91]. Microdialysis also produces damage in a large area, greater than one millimeter diameter, around the implant site and a glial scar that reduces detection with chronic implantation [98].

Voltammetry, including the techniques of chronoamperometry, pulse voltammetry and fast cyclic voltammetry, differs from microdialysis in that it uses a potential applied to an electrode to oxidize molecules, generating an oxidation current at the electrode surface. Electrochemical sensors like CFMEs and MEAs use a method of voltammetry or amperometry to acquire data on fluctuations in extracellular Glu concentration. Though microdialysis is more highly selective than an electrochemical sensor, the CFMEs and MEAs have faster response times and can be much smaller than microdialysis probes for better spatiotemporal resolution [99].

CFMEs as a probe for neurotransmitters were originally developed in 1973 by the Adams lab to measure catecholamine levels [100]. CFMEs are advantageous for biological applications as they are biocompatible, non-toxic, and minimally invasive, on average less than 10 μm in diameter [101]. CFMEs have a much faster response time versus microdialysis [101], [102]. Continual improvements to sensitivity and selectivity have been the major focus of many studies using CFMEs.

Selectivity in electrochemical sensors is achieved by coating a microelectrode surface with a discriminating material that will pass specific molecules and block others. Nafion, for instance, is used to decrease anionic interference [103], [104]. Glutamate oxidase (GluOx) is an enzyme that catalyzes glutamate into a keto acid, ammonia, and hydrogen peroxide. It is often used in combination with a base material as a selective sensor coating for Glu, where peroxide becomes the analyte. For instance, the Westerink lab in 2005 developed CFMEs with redox hydrogel-enzyme coatings to act as a Glu sensor [91].

Semiconductor carrier, multisite microelectrodes were first introduced in 1970 by Wise, Angell, and Starr [105]. Their design used gold electrodes formed on a silicon wafer. Thirty years later, in 2000, Burmeister, Moxon, and Gerhardt suggested using ceramic substrates, introducing a four-site platinum electrode on ceramic wafer with polyimide coating [106]. Using ceramic-based microelectrodes resulted in a fast responding and highly sensitive microarray with material strength better than that of silicon probes. Silicon probes must be insulated prior to laying conductive lines. In contrast, the non-conductive ceramic material provides a decreased shunt capacitance

between the metallization layer and the substrate, reducing electrode crosstalk [106] which reduces processing time.

In 2001, Burmeister and Gerhardt reported using the same probe to self-reference measurements of Glu in the rat brain [104]. This was accomplished by using two recording sites in close proximity, one coated with GluOx (enzyme) and a bovine serum albumin (BSA)/glutaraldehyde mixture as well as Nafion, and the other with the BSA mixture and Nafion without the enzyme. Through this enzyme coating, it could be assured that peaks seen only in the GluOx site were due to Glu while any interference peaks recorded with the BSA site could be subtracted from the Glu recording.

Dr. Gerhardt went on to found CenMeT, The Center for Microelectrode Technology, at the University of Kentucky where ceramic-based MEAs can be commercially ordered by laboratories seeking neurotransmitter probes. In Chapter 7 of this work, we have used one of CenMeT's MEAs, the R1 probe, to assess Glu uptake by astrocytes *in vitro*.

CHAPTER 7

AN ENZYME-BASED ELECTROCHEMICAL PROBE TO MEASURE ASTROCYTIC UPTAKE OF GLUTAMATE IN REAL TIME

Glutamate (Glu), the most prominent excitatory neurotransmitter in the mammalian CNS [107], plays an important role in normal synaptic function [73]. In presynaptic terminals, glutamate is housed in vesicles, which are released by a Ca^{2+} dependent mechanism [74]. It is estimated that each vesicle contains a concentration of approximately 100 mmol/L, while the synaptic cleft maintains a concentration of approximately 2-1,000 μmol/L [72]. Glutamatergic neurotransmission is controlled by glutamate concentrations in the extracellular fluid of the synapse. As vesicles filled with glutamate are released, the concentration of glutamate within the synapse must be depleted quickly to prevent overexcitation of glutamate receptors, as this leads to neuronal damage and death, known as excitotoxicity.

Excitotoxicity, the damage of neurons due to increased concentrations of Glu, is found in seizure activity [108]. As neurotransmission through the glutamatergic synapse involves specific Na^{+} and Ca^{++} exchanges in receptors, ionic imbalance occurs when excessive Glu appears in the cleft. Since there are no enzymes in the extracellular fluid to remove Glu from the synapse, free Glu must be removed from the extracellular fluid

through diffusion and cellular uptake [75]. It has been suggested that impaired uptake contributes to epileptic seizures [108]–[110].

Astrocyte Glu transporters EAAT2 and EAAT1 are the primary clearance proteins responsible for ensuring rapid Glu uptake from the extracellular space [83], preventing neuronal excitotoxicity. For EAAT1-3 transporters, Glu transport times are estimated at 10-50 ms [90] which are slow compared to Glu binding times, < 100 μs [86], making Glu transport the rate limiting step. Different transport subtypes vary in their speeds of the glutamate transport cycle, causing dynamic kinetics and a range of time in which glutamate concentrations are cleared [85].

A secondary mechanism for controlling Glu uptake in extracellular space is the System X^c (SXC), a Na^+-independent glutamate/cystine exchanger. In healthy astrocytes SXC acts as a cellular protectant, enabling uptake of cystine necessary for glutathione synthesis, which neutralizes reactive oxygen species. However, in glioma cells, SXC is used to support rapid growth through increased cystine uptake. As SXC is an exchanger, glioma cells release glutamate, causing an increase in extracellular Glu [77]. Glioma cells also downregulate EAATs[111], causing impaired uptake. Glioma glutamate imbalance has been implicated in seizure activity for patients with brain tumors.

Here we have employed an enzyme-based, highly sensitive electrochemical multisite microarray to measure *in vitro* astrocytic uptake of extracellular Glu in real-time. A comparison between healthy astrocytes and a glioma line were made to determine whether impaired uptake could be deciphered using the sensor. Recorded measurements verify a detection range of 10 - 570 μM with 4.4 ± 0.3 pA/μM sensitivity.

7.1 Materials and Methods

7.1.1 Amperometric Probes for Glutamate Sensing

As a study of capability in design, Glu sensor probes were created by manually coating glutamate oxidase (GluOx) and electrodeposition coating m-phenylenediamine (mPD) onto a commercial probe (R1) from CenMeT, the Center for Microelectrode Technology at the University of Kentucky, KY, USA. R1 probes are ceramic-based microelectrode arrays (MEAs) with four platinum electrode sites, size 50 µm x 150 µm with 50 µm spacing in between (Figure 7-1). An Ag/AgCl reference electrode was attached close to the extended body of the array for all recordings. A constant potential (+0.7 V) was applied to the electrodes versus the reference electrode. MEA data were recorded every 0.1 seconds. An eight-channel FAST-16mkIII electrochemical recording system (Quanteon, LLC, Nicholesville, KY, USA) was used to record all data.

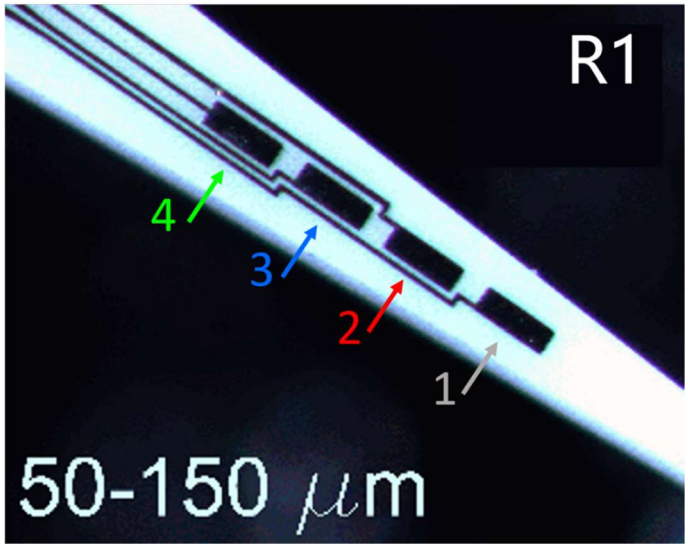

Figure 7-1: R1 Probe, Uncoated. Four Pt recording sites (50x150 um with 50 ums between sites). Modified from the CenMeT products page [112]. Colors indicate recording site numbers as expressed in data.

GluOx is an enzyme that catalyzes glutamate into α-keto acid, ammonia, and hydrogen peroxide as shown in the reaction below.

$$\text{L-glutamate} + O_2 + H_2O \rightleftharpoons \text{2-oxoglutarate} + NH_3 + H_2O_2$$

It is often used in combination with a base material as a selective sensor coating to measure Glu concentration, where peroxide becomes the analyte. Coating of probes was completed according to previous works [113]–[116]. Prior to coating, probes were cleaned with 70% isopropyl alcohol and DI water. Then blown dry with N_2 and put into an oven at 160˚C for five minutes. GluOx solution (0.1 U/µl GluOx, 0.8% BSA, and 0.1% glutaraldehyde) was applied to all four recording sites. Probes were placed in the dark at room temperature for at least 48 hours before use. The night before an experiment, a size-exclusive layer of mPD was electrodeposited to the enzyme coated surfaces by cyclic voltammetry scan between +0.2 V and +0.8 V for 20 minutes (10 mM mPD in 1M KCL, a Ag/AgCl was used as reference electrode, the scan rate was 5 mV/s).

Probes were calibrated before each *in vitro* recording session. A dish containing only the media used for either astrocytes or tumor cells was placed into our homemade incubator system, see cell culture for details. The sensor with reference electrode was immersed into the media. After a stable baseline was established, Glu concentrations were added via dropper: 10 µM, 20 µM, 40 µM, 100 µM. The same concentrations were added to the experiment dishes containing astrocytes or CRL-2303 tumor cells.

7.1.2 Cell Culture

Astrocytes from primary newborn rat tissues were cultured on 35 mm tissue culture (TC) treated petri dishes (Falcon®) in Nutrient Mixture F-12 Ham plus

L-glutamine and sodium bicarbonate (Sigma) with horse serum (5% v/v), fetal bovine serum (5% v/v), and penicillin/streptomycin (0.5% v/v). To demonstrate the utility of the probe to discern cells with impaired Glu uptake, CRL-2303 (ATCC, C6/lacZ7) rat glioma cells were cultured on Falcon® 35 mm TC treated petri dishes. Culture media consisted of DMEM-high glucose (4500 mg/L), L-glutamine, and sodium bicarbonate, with fetal bovine serum (10% v/v), MEM non-essential amino acid solution 100x (1% v/v), and penicillin/streptomycin (0.5% v/v). The petri dishes were coated with poly-L-lysine one day prior to plating cells. Both astrocytes and CRL-2303 tumor cells were plated at 750,000 cells per dish. Cells were incubated at 37˚C with a CO_2 buffer (95% O_2/5% CO_2) and grown to ~80% confluency for experiments. Prior to experiments, cells were imaged and then media was replaced with 5 mL fresh, serum-free basal media without L-glutamine. After measurement experiments were completed, cells were imaged again. Cellular morphology was used for a qualitative assessment of relative health of the cells. While cells sometimes had a slightly narrower morphology at the end of the experiment, they were remained adherent and spread on the dish, implying that the cells were alive and functioning.

Due to both the length of these experiments (exceeding five hours) and the sensitivity of the R1 probe to changes in temperature, cells were maintained in a homemade water bath placed inside a Heratherm IMC18 bench top incubator (Figure 7-2). The MEAs were also sensitive to electrical noise from lights, motors, other equipment in the lab. Thus, the incubator door was only opened when necessary.

The bath temperature was monitored by a temperature probe consisting of a thermistor (Agilent) run through an analog circuit connected to an Arduino Mega 2560.

Temperature data were measured and recorded once every 18 seconds using PLX-DAQ software, which writes data from Arduino directly into an Excel spreadsheet.

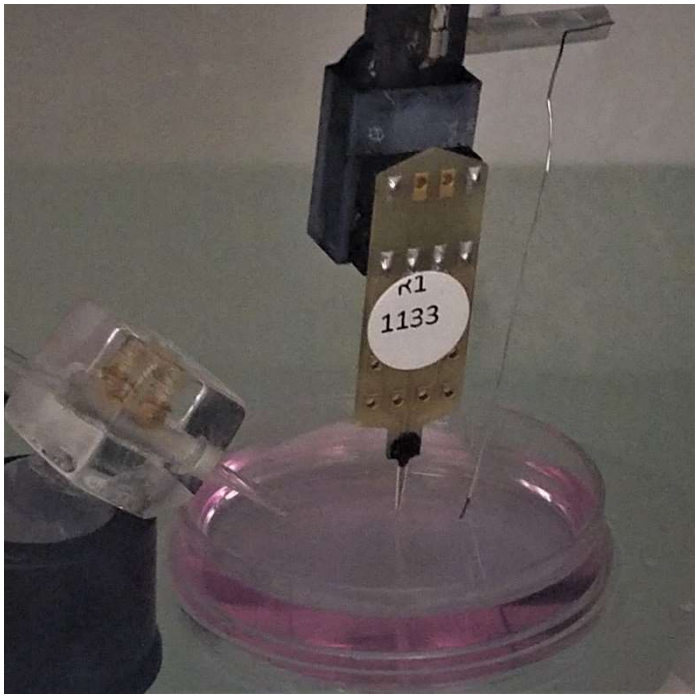

Figure 7-2: Environment and Sensor Arrangement. Sensor immersion into fluid, covering all four sites; centered in dish. Does not touch bottom of dish. Reference pictured to right. Dropper pictured left.

Carbogen (95% O_2/5% CO_2) was added to the test environment for 15 minutes at the beginning of every experiment to buffer the cell culture media. The probe was placed into the approximate center of the dish with all four electrodes fully immersed in media (Figure 7-2, B). Glu solutions of specific concentrations were added near the outer edge of the 35-mm dish to minimize motion artifact in the recordings. A CMA microdialysis automatic syringe pump was used to drop precise volumes of Glu solution.

7.1.3 Data Analysis

Peak data was assessed using Origin Pro 2018 software from Originlab. Specifically, the Quick Peaks Gadget was used to assess peak maximums. The Rise Time

Gadget was used to assess rise (t_{90-10}) and fall (t_{20-80}) times as well as fall velocity (T_c) and maximum velocity (V_{max}). The Integrate Gadget was used to assess area under the curve (AUC), and full duration at half maximum of concentration additions (FDHM).

Data analysis was performed using GraphPad Prism 7.03. Prior to analysis, outliers were removed using the robust regression and outlier removal (ROUT) method with Q set to 0.5%. The differences in mean probe measurements between the glutamate uptake by astrocytes and CRL-2303 cells were compared using a two-tailed unpaired t-test with Welch's correction, as data set variances were significantly different. For all significance values, α was set to 0.05.

7.2 Results

7.2.1 Electrochemical Characteristics of Home-Coated R1 Probes

Though the MEA probes from CenMeT are well characterized [92], [104], possible changes in recording performance in our hands, due to manual and electrodeposition coating, may have occurred. To determine the electrochemical characteristics of these manually coated and electroplated microelectrodes, two tests were performed: (1) tests in basal media to determine the limits of detection and (2) acute media calibrations compiled to acquire sensitivity and potential variation in site due to coating differences.

To determine both the limits of detection and the linear portion of the calibration curve, measurements over a large range of Glu concentrations were acquired using constant-potential (E = +0.7 V) amperometry. A concentration range of 0-730 µM was investigated with a step size according to the reference in Table 7-1. The third column shows the actual concentrations after increasing Glu concentration by the addition in the

first column. The site data are presented as the average of the last five minutes of each addition, considered baseline for each electrode site, numbered as shown in Figure 7-1.

Table 7-1: Concentration and current of the basal media calibration test.

Added Glu (µM)	Amount added (µL)	Final C Glu (µM)	Site 2 (black, pA)	Site 3 (red, pA)	Site 4 (blue, pA)
0 µM	5000	0.1	854.9	746.7	837.1
10 µM	5	10	946.5	832.0	943.5
20 µM	10	30	998.9	863.7	987.2
40 µM	20	70	1153.9	976.2	1144.3
60 µM	30	130	1398.5	1172.8	1395.0
80 µM	41	210	1671.5	1379.5	1666.4
100 µM	51	310	2026.4	1625.8	2000.2
120 µM	62	430	2227.5	1800.1	2237.8
140 µM	73	570	2388.2	1874.5	2343.4

Site 1 not shown as not used for data acquisition. Dropped signal, so deemed defective.

Figure 7-3 depicts the calibration of the Glu sensor. As seen in the raw data (Figure 7-3, A), the upper limit of the probes peaked around 570 µM. This is the point at which peak values for increasing concentrations of Glu became indistinguishable in the plot of current versus Glu concentration. The calibration curve resulting from the basal media calibration is a sigmoidal curve (Figure 7-3, B). The upper tail of the curve begins plateauing around 550 µM, illustrating that concentration limit that was estimated from the raw data. The linear portion of the curve ranges from ~ 10 µM to ~ 200 µM.

A

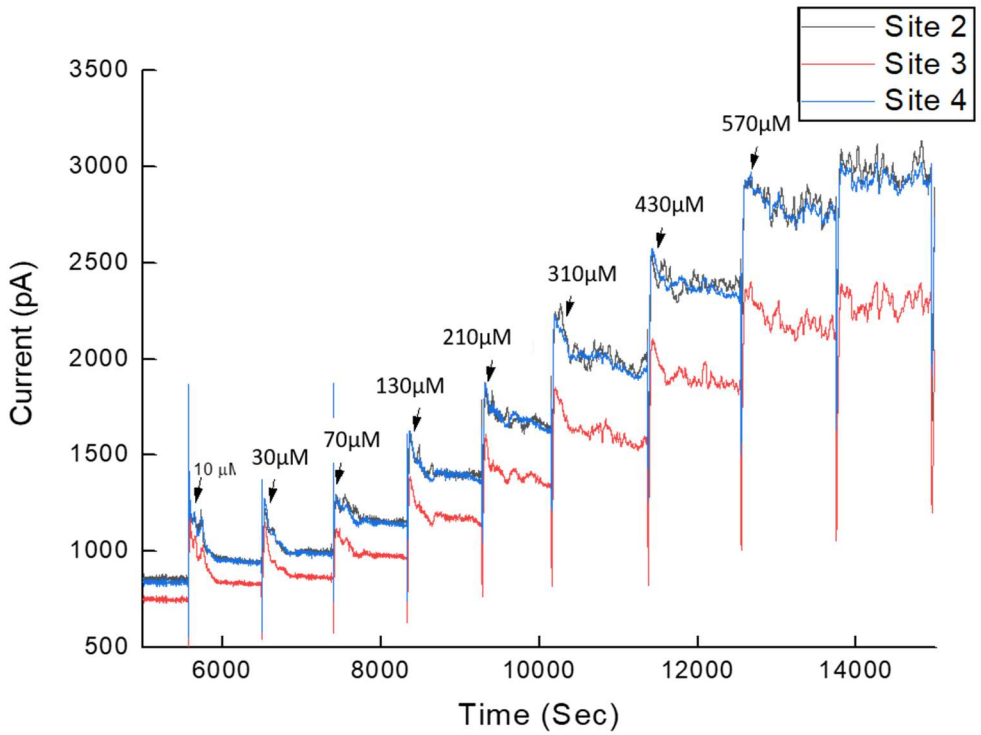

B

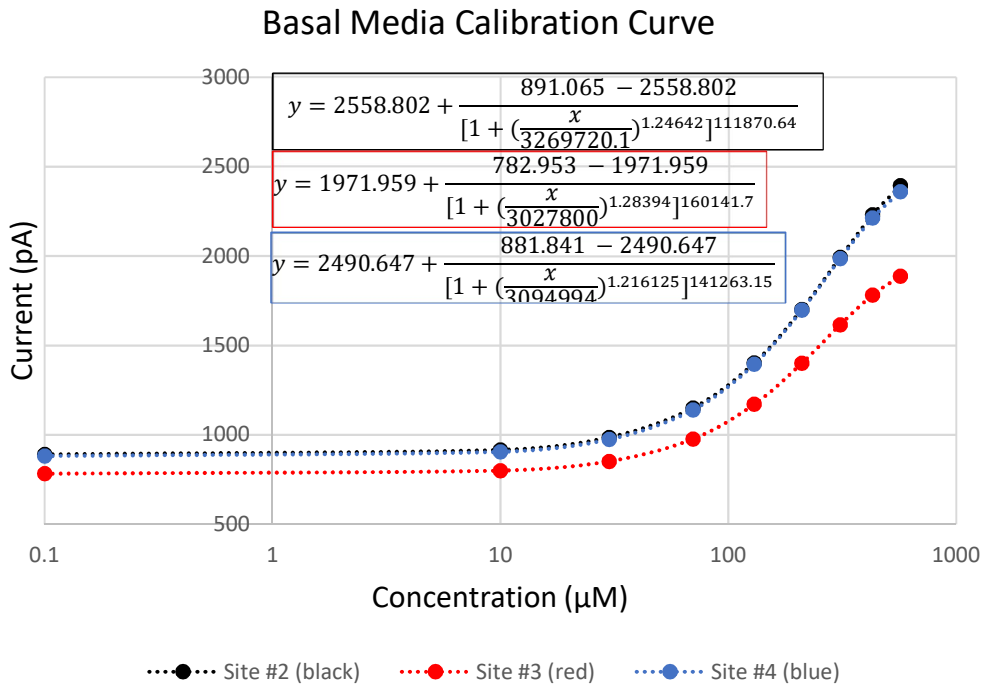

Figure 7-3: Calibration of Glu Sensor. A. Raw data, current versus time. Glutamate added as noted on the plot. Sites 2-4 shown; Site 1 not shown because defective. B. 0.1-570 uM calibration of probe using basal media. Dotted lines are five parameter logistic fit for asymmetrical sigmoidal data; fit equations boxed.

A basal media calibration was performed acutely, prior to each *in vitro* cell test. The probe was dipped into the approximate center of the dish and immersed into media fluid, covering all four sites. Concentrations of 10 µM, 20 µM, 40 µM, and 100 µM (10 µM, 30 µM, 70 µM, 170 µM totals) were added in 15-minute intervals after a stable baseline was achieved, approximately 1.5 hours. Excellent linearity was observed for all sites (Figure 7-4), R^2 Pearson correlation coefficients being 0.995 or greater. The linear region of the calibration curve was used to determine the amount of glutamate added using Equation 7-1:

$$[\text{Glutamate}]\text{uM} = \frac{\Delta\text{Sample}}{\text{Slope}}. \tag{7-1}$$

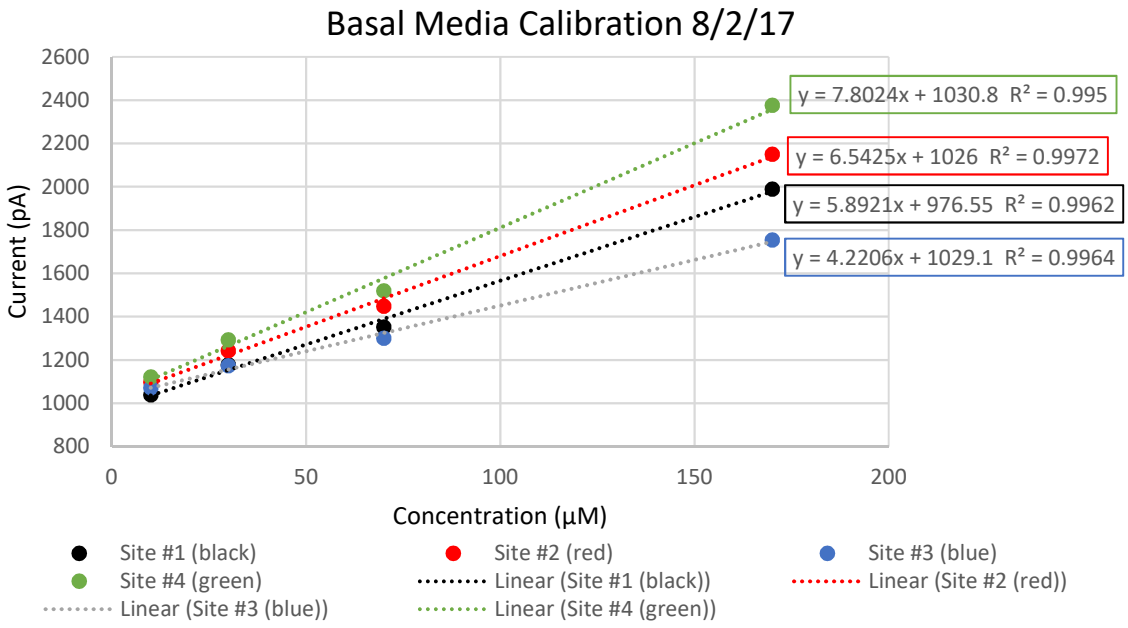

Figure 7-4: Basal Media Calibration Sample, Day 8/2/17. Site colors correspond to site regions indicated in Figure 7-1. Slope and linear fit calculated from measurements taken in basal medium (n = 1).

To ensure that Equation 7-1 was the most appropriate way to assess glutamate concentration, a second method was investigated using the sensitivity ratio. Since there

was question as to whether manually coated sites would differ in sensitivity, sites were individually calculated for sensitivity (Table 7-2). Ratios were calculated by dividing the change in concentration pA (Δ pA) during calibration by the actual concentration added. Ratios were then averaged across individual sites for each day's sensitivity and across days for the total sensitivity. As coating is manual, sensitivities differ due to amounts applied before electrodeposition. Any potential defects in the surface of the electrode may also cause difference in sensitivity.

Table 7-2: Sensitivity for Manually Coated Microelectrodes

	n	Sensitivity (pA/uM)
Site 1	12	4.4 ± 0.5
Site 2	11	5.1 ± 0.4
Site 3	11	2.9 ± 0.4
Site 4	12	5.3 ± 0.6
Total	46	4.4 ± 0.3

Sensitivity listed as mean ± standard error of the mean; *n*, number of tests using this site

7.2.2 Glutamate Dynamics According to Electrochemical Analysis

An advantage to using a microelectrode is that readings are given per hundred milliseconds, so real-time measurements can be taken. To determine probe analysis characteristics relevant to cell uptake using the MEA sensor as designed, comparison of astrocytes to the astrocytic tumor line CRL-2303 were made with special attention to peak rise and fall times, fall velocity (T_c) and max velocity (V_{max}), area under the curve (AUC), and full duration at half maximum of concentration additions (FDHM).

Previous studies have discussed two ways to gather cell enzyme clearance rates from a probe such as ours: (1) by finding the slope of the most linear portion ($t_{20\text{-}80}$) of peak decay time, T_c, [117] and (2) by finding the rate constant, k, using an exponential

decay function to assess the fall of the peak [104]. Here, we have used the T_c method to calculate the clearance rate of glutamate in astrocyte and CRL-2303 glioma cell cultures (Figure 7-5). A significant difference was found between the clearance rate in astrocytes and CRL tumor cells; $p < 0.0001$, $\alpha = 0.05$. The T_c (mean ± SEM) for astrocytes was 1.3 ± 0.22 pA s^{-1} (n = 36 tests) and the CRL T_c was 3.31 ± 0.3 pA s^{-1} (n = 38 tests), leaving a difference of 1.99 ± 0.4 pA s^{-1} between means.

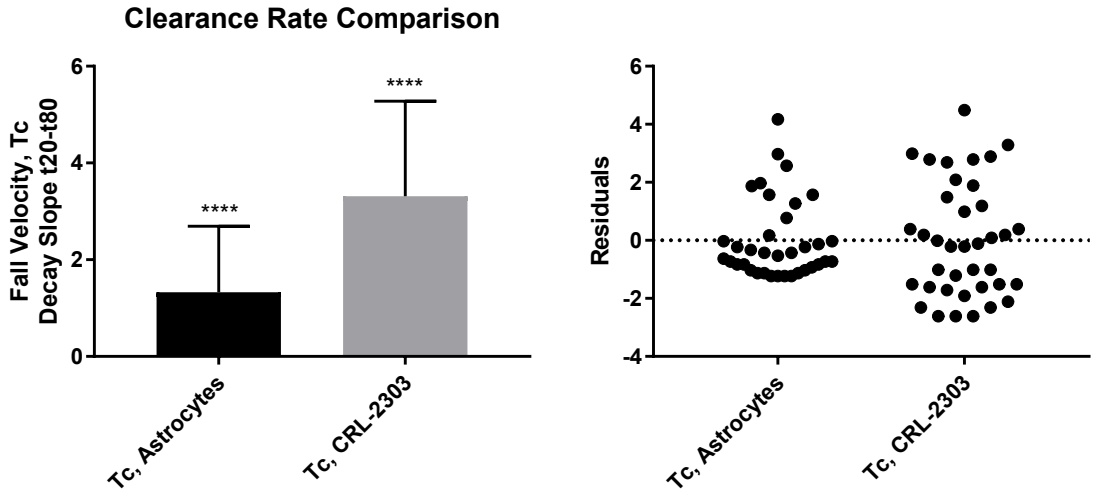

Figure 7-5: Glutamate clearance rate. Left. Fall velocity (Tc) determines the rate of glutamate clearance by astrocytes and CRL-2303 cells. Lower velocity in astrocytes indicates slower clearance rate. **** $p < 0.0001$. Error bars: mean ± SEM. Right. Scatter plot of residual values. Height difference in CRL-2303 indicates wider deviation from the sample mean than astrocyte group.

Total duration time for astrocytes and glioma cells was compared according to the full duration at half [peak] maximum (FDHM) for each group. The expectation was that a more rapid elimination of Glu from astrocytes would decrease the duration of response within the astrocyte group. Instead, the astrocyte response was significantly longer than the tumor line response (Figure 7-6).

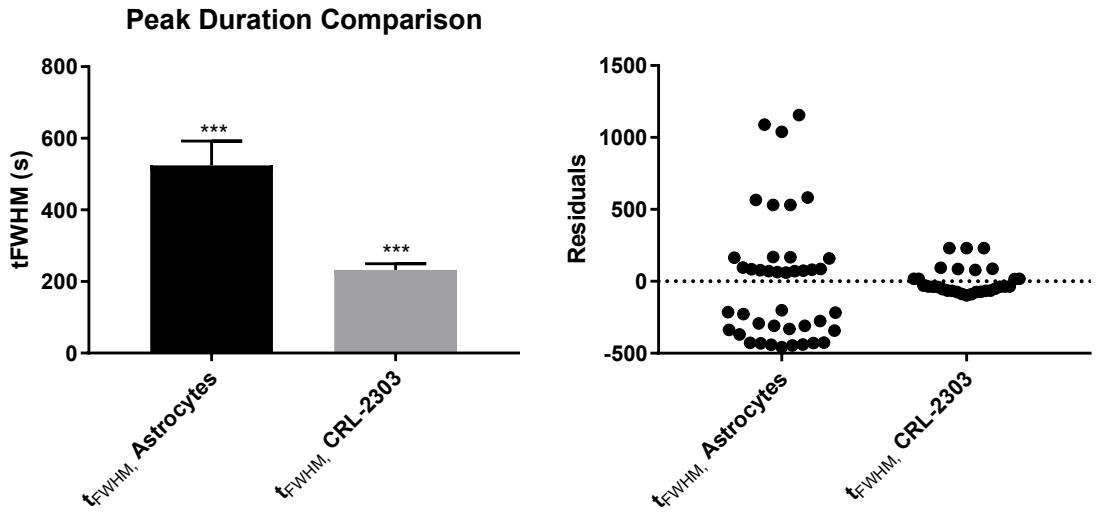

Figure 7-6: Peak Duration. Left. FDHM of peak comparison longer response duration in astrocytes. *** p = 0.0001. Right. Durations of individual concentrations seen clearly as "levels" in residuals plot. Differences in residual height indicate more tightly grouped FDHM over all concentrations in glioma. All error bars: Mean ± SEM.

In pharmacokinetics, the AUC represents total drug exposure over time and is linearly proportional to the dose where the clearance rate should be constant over that dose interval. Here, the AUC represents the total Glu exposure over time. The total AUC of the astrocytes and CRL-2303 cells were compared. As seen in Figure 7-7, A, astrocytes have significantly larger AUCs than do glioma cells. This shows a more robust reaction to Glu additions in astrocytes and agrees with the FDHM that astrocytes have longer response duration than CRL-2303 cells.

Clearance rate constants, k, were calculated by dividing the AUCs of each peak by individual concentration levels added prior to the peak. Rate constants were then compared to determine if the extended duration and higher Glu exposure over time could be explained by difference in constant uptake versus rapid uptake (Figure 7-7, B). The rate constant k was significantly smaller in the glioma line than in the astrocytes. This

shows that glioma uptake is slower overall when compared to the astrocytic uptake, as expected.

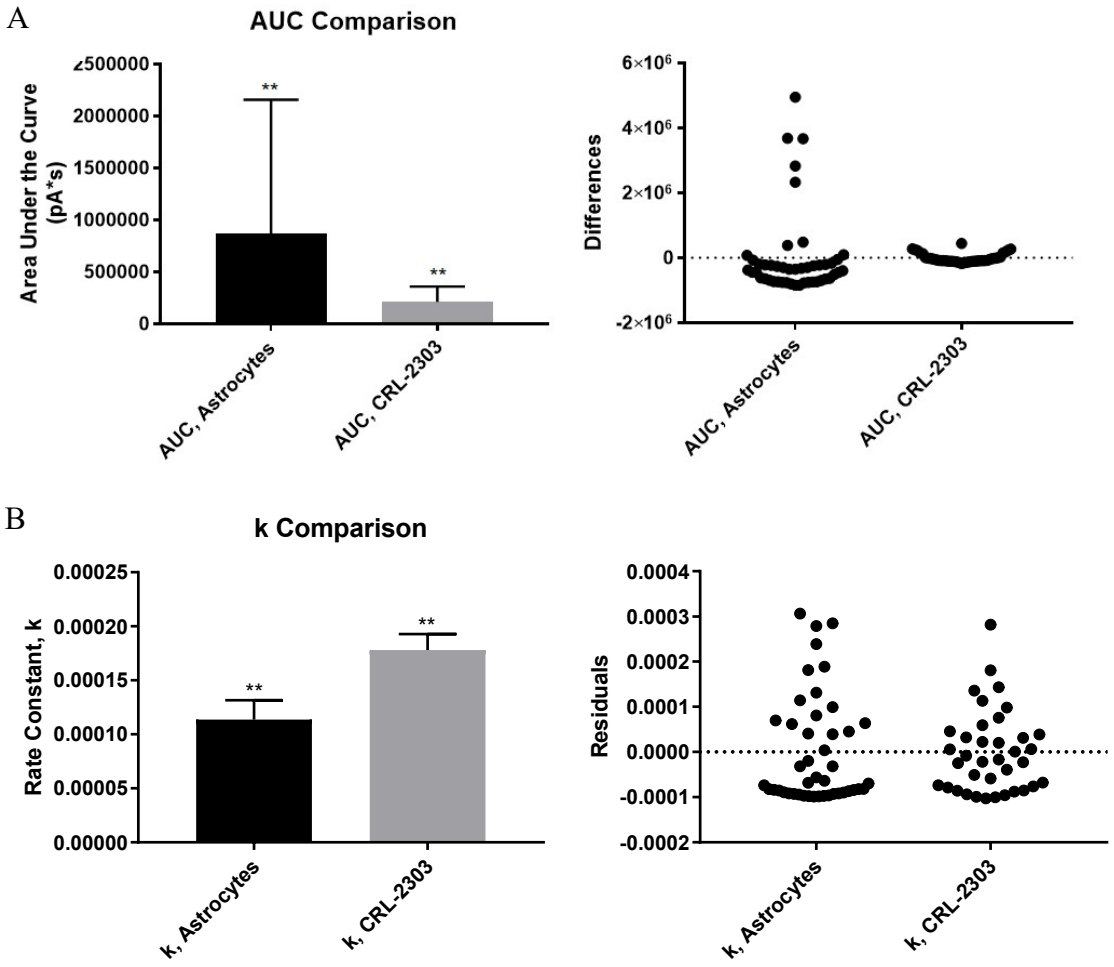

Figure 7-7: Area under the Curve. A. Left. AUC comparison shows longer response duration in astrocytes, in agreement with FDHM. ** p = 0.002. Right. Areas seen as tightly grouped to individual means (around 0). B. Left. Rate constant, k, from AUC comparison indicates lower clearance rate in astrocytes (See discussion). ** p = 0.007. Right. Approximately equal height and widths of residuals indicate consistent deviation from sample mean between groups. All error bars: Mean ± SEM.

Since the CRL line has impaired uptake, we expected that the astrocyte rate of elimination should be greater than the CRL rate of elimination. To assess the astrocyte and CRL rates of elimination, the maximum fall velocity, V_{max}, corresponding to the maximum rate of elimination were compared. V_{max} differed significantly between groups;

$\alpha = 0.05$ (Figure 7-8, A). Mean astrocyte V_{max} over all groups was 22.8 ± 3.6 pA s^{-1} (n = 39), which corresponds to a maximum uptake rate of 4.5 uM/s. For CRL cells, the mean V_{max} was 11.22 ± 1.4 pA s^{-1}(n = 31), with a difference of 11.6 ± 3.9 between means. Thus, the maximum rate of elimination was lower for CRL tumor cells than astrocytes, as expected.

Latency in peaks, corresponding to impaired uptake, were expected in the dish containing tumor cells. Thus, rise times were compared between astrocytes and glioma cells (Figure 7-8, B). The difference between rise time means is 34.6 ± 6.6 s, with astrocyte rise times being much higher (64.6 ± 6.1 s). A shorter rise time for the glioma line would indicate either faster binding and uptake times, which is unlikely, or a higher concentration of glutamate present within the dish. It is likely that rise times are faster due to CRL glutamate release.

If glutamate is continually being released by tumor cells, then concentrations would be higher overall when adding more glutamate to the system than they would be in the astrocyte dish, where cells are uptaking Glu. This difference in baseline may not be enough for the probe to detect between groups during stable readings, and as such, is detected only when additions cause a sharp rise in overall concentration. Thus, data suggest that astrocytes clear glutamate faster than glioma cells, which retain an overall higher extracellular Glu concentration.

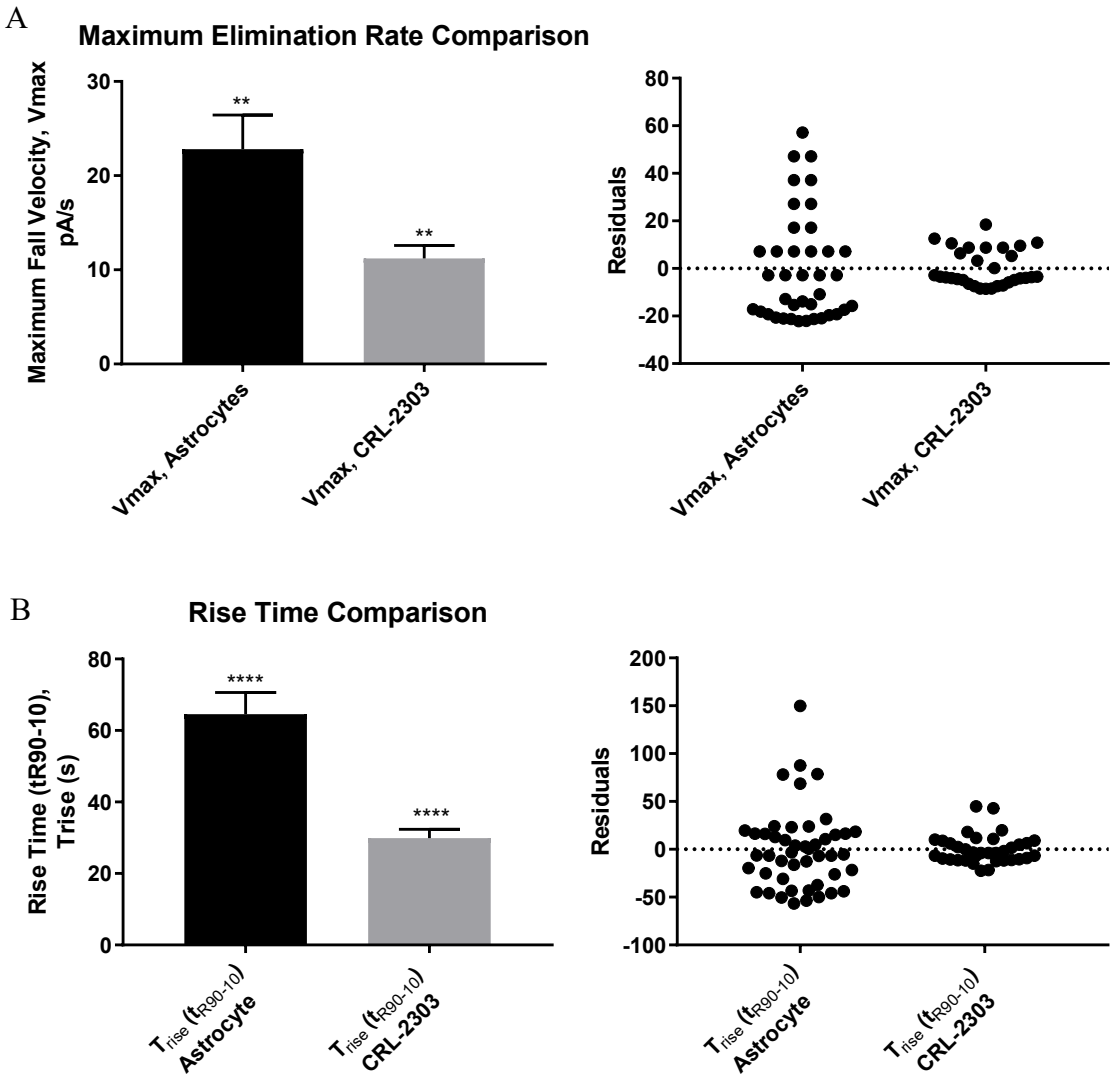

Figure 7-8: Further comparisons. A. Left. Maximum Fall Velocity comparison shows astrocytes have higher faster elimination rates than glioma. Right. Residual plots display individual recordings deviation from sample mean, fan shape indicates possible need for data transformation. ** $p = 0.004$. B. Left. Rise times of astrocyte versus tumor cells indicate shorter rise times for glioma. **** $p < 0.0001$. All error bars: Mean ± SEM.

7.3 Discussion

We have presented an enzyme-based, highly sensitive electrochemical multisite microarray to measure *in vitro* astrocytic uptake of extracellular Glu in real-time. This probe makes real-time measurements in a verified range of 10 - 570 µM Glu *in vitro*

without the need for cell lysate. The overall sensitivity is 4.4 ± 0.3 pA/uM. As the clearance rate comparison indicated a lower clearance rate for astrocytes than glioma cells, contrary to expectation, a different view was taken to explain this characteristic.

Normal transportation contains an approximate 50% chance of Glu diffusing from astrocytes only to be bound again before transportation. However, impaired uptake should have a greater chance of diffusion back into the media and less active transport, causing a stepped like appearance in the curve, similar to the calibration. Indicators of this could be coming to a faster steady baseline, again, similar to the calibration. This is what we see with the FDHM of the astrocytes versus CRL-2303 cells. The glioma line comes to a faster steady baseline at higher current, indicating higher overall concentration, even at higher concentration additions like 100μM. This is unlike the astrocyte line which has a longer FDHM and is continually decreasing in current rather than coming to a steady baseline at higher concentration additions. This is the first indication that the glioma cells have impaired uptake.

The further release of Glu from the glioma line would put even greater glutamate back into the media. Glioma cells have been shown to release glutamate even in 100 μM conditions [111], so we should expect that the CRL-2303 cells are releasing glutamate through the System X_c^- exchanger. We would expect that more diffusion of glutamate away from cell bodies toward the electrode would result in the detection of higher levels of glutamate, as the steepness of the concentration gradient adjacent to the electrode directly determines the observed current magnitude. As glioma cells release glutamate, the current should rise farther and faster than that of the astrocytes, which are taking up the glutamate. The astrocyte dishes show longer rise times, indicating that the CRL line

current does rise faster than the astrocytes. However, the total AUC is larger for astrocytes than for glioma cells. This could indicate either a higher (farther reaching) peak or a longer response in the astrocyte dish.

The k constant was computed to assess both AUC response and as another test for clearance rate difference between groups. To recap, the k constant is calculated by taking the AUC of each peak and dividing by the concentration added prior to the peak. The k constant for the glioma line is smaller than the astrocytes, indicating a slower consistent clearance rate in glioma due to impaired uptake as expected.

The CRL-2303 cells also have slower elimination rates as shown through V_{max}. The maximum fall velocity is a measure of the fastest change in concentration during the decay peak, that is, the time that cells should be uptaking Glu to bring down concentrations in the dish. A faster V_{max} corresponds to greater potential for eliminating Glu from the dish. When corresponding with faster rise times, the indication is that glioma cells have greater overall concentrations in the dish, likely due to release, while impaired uptake keeps their maximum elimination rate slower.

Thus, we concluded that we are able to make a distinction between glioma cells and astrocytes, due to CRL-2303 Glu release characteristics. A curve more stepped like in appearance, closer to that of a calibration curve, coming to a steady baseline faster and having a shorter FDHM, is a first indication of impaired uptake. A second indication is a lower k constant, indicating a slower overall clearance rate. Finally, faster rise times corresponding with a slower maximum elimination rate all add to indicate impaired uptake in glioma cells.

CHAPTER 8

DISCUSSION

Neuroscientific research advancement is of principle concern to our nation. We see this in the "Grand Challenge" of the BRAIN Initiative put forth by the Obama administration in 2013. This challenge encourages researchers to study the brain, its cellular interactions, and circuitry through the development and application of new neurotechnologies. It is hoped that this will enable researchers "to treat, cure, and even prevent brain disorders." This initiative expresses both our need for increased knowledge in neuroscientific study and our belief that accomplishing higher levels of understanding will require new machinery and mechanisms that expand our current toolboxes.

Presented within this cumulative work are a total of three projects overseeing three distinct devices that advance neuroscience research. Each of these devices was created or explored in answer to questions arising from the needs of research groups working within the neuroscientific field of study. However, each advances the field in different ways.

Development of the 3D printed stage-top incubation system supports the overall movement of collaboratively sharing open-source hardware ideas on websites like Thingiverse or the NIH 3D Print Exchange. Through sharing the printable device, it is expected that other laboratories will download and construct the device. This will create a monetary return on investment (ROI) for the scientific community as discussed in Section

8.1.2. This device advances the field first through putting more resources into the hands of researchers who can use it to continue furthering their efforts and second through offering a stage-top incubation device to universities and/or communities who do not have access to one but do have access to 3D printing. This is further discussed in Section 8.1.

The PICS design supports imaging of curved tissue, especially wholemount imaging, in multiple scientific areas of expertise as PICS can be easily printed and machined for use in other laboratories where necessary. Specific to neuroscientific study, PICS provides a tool to better image lateral ventricular wall wholemounts, allowing for quality and efficient study of the SVZ stem cell niche. However, PICS could also be used to study retinal ganglion cells, which spreads its use into areas of development and regeneration as mentioned in Section 8.2.

The utility of the MEA sensor in determining differences in uptake between normal astrocytes and the CRL-2303 line shows that such a probe will be beneficial for monitoring the impairment of uptake in an *in vivo* model. This application advances the field by granting identifiers that normal and impaired uptake can be compared from. Such a probe can be used for both epilepsy and glioma research. However, the monitoring capabilities of these sensors have potential in the clinic as well, as discussed in Section 8.3.1.

Though each project advances the field in different ways, the sum of the work is the advancement of neuroscientific investigation through engineering tools and/or the applications of existing tools, creating a broader toolbox to work from. Each tool's impact to the field is discussed in further detail at the end of each section. Finally, future

design modifications to the stage incubator and PICS system that would increase their usefulness are discussed.

8.1 Stage-Top Incubation

The first research requirement addressed in Chapters 2 and 3 comes from the in house need of our own laboratory. We asked the question, "Can we develop a low-cost and efficient *in vitro* incubation device for our research aims?" This question came about due to an experiment in which we needed five hours of continuous cell imaging on a microscope. Though there are already commercial stage-top incubators on the market, the costs of the stage-top incubators were beyond the resources we had available for that project, as it was a preliminary study. Also, we believed the question had relevant implications for the overall scientific community. As 3D printing machines have grown in popularity, their use in the laboratory has also grown. So much so that the NIH (National Institutes of Health) now has an open-source website dedicated to sharing printable models, called the NIH 3D Print Exchange [4]. It was believed that if we could answer this question and that a stage-top incubation device could be printed, then it could be made available through the NIH 3D Print Exchange and become useful to researchers who also needed such a device.

Through answering this question as discussed in Chapter 3, we found that 3D printing is capable of creating custom lab equipment like a stage-top incubator. Since we had previously shown that we could create an animal warming device using a FDM™ printing system, we redesigned this device to fit 35-mm dishes. As there were problems with vibration in the device, we also redesigned the original stage-top device to reduce water flow vibration. The final stage-top incubator design showed it was capable of

24-hour sustained heat stability and acceptable viability at five hours of incubation. This determination was based on temperature testing, cell imaging, pH testing, and media evaporation measurement in comparison to a commercially incubated negative control and a positive control left on the benchtop. An equation for temperature of the experiment well based on the temperature of the sensor well was calculated so that temperature of the experiment well may be monitored at all times.

8.1.1 Future Work

It was determined through our use that adding dH_2O in the sensor well encourages media retention. However, it appears that media evaporation from the stage-top device over time also correlates with the CO_2 loss, that is, as time goes on, the system loses both more media to evaporation and CO_2 to leakage. Combined, this indicates that the system may need better sealing and more refined gas control. As future work for the device, sealing and refining gas control are key to ensuring viability and need to be addressed first.

A simple fix to create a better seal would be to widen the bottom plate of the device so that the CO_2/O_2 covering fits into the bottom plate (Figure 8-1). This differs from the previous arrangement in that both the CO_2/O_2 covering and bottom plate were surrounded in silicone. Since silicone was applied manually, it may not have been as think in some areas as others, possibly allowing leakage. Fitting the CO_2/O_2 covering into the bottom plate as seen in Figure 8-1 would prevent gas from escaping through the sides.

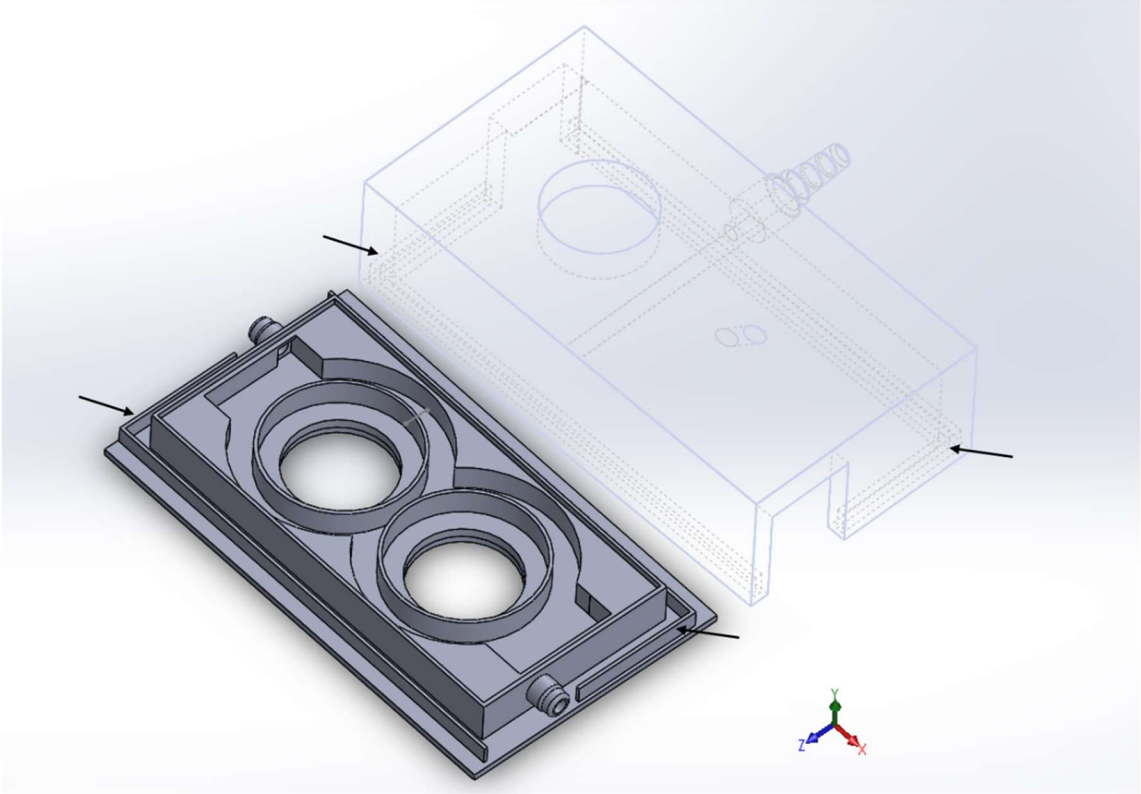

Figure 8-1: Future Stage-top Incubator Design. CO_2/O_2 covering fits into the bottom plate via the inserts seen in the bottom plate. Arrows depict connection planes. This actively seals the bottom and sides to prevent gas loss.

It was also suggested in Chapter 3 that a CO_2 gas unit and air pump may allow for more refined gas control. This is necessary in this system both to prevent CO_2 loss and to ensure concentrations are kept around 5% CO_2, avoiding over exposure. The gas unit and air pump mentioned in the proposed incubator combination (Table 3-3) can either be controlled with a digital touch interface bought separately from the manufacturer or through a software development kit (SDK) available through the manufacturer's website. It appears as though this SDK is compatible with programs such as LabVIEW from National Instruments or MATLAB from MathWorks®. Though it is not yet clear how easy this SDK would be to implement or run, the availability demonstrates an avenue to cut costs and run the integrated system.

8.1.2 Implications for the Scientific Community

Development of the 3D printed stage-top incubation system supports the overall movement of collaboratively sharing open-source labware ideas on websites like Thingiverse or the NIH 3D Print Exchange. According to Dr. Joshua Pearce, the head of the Michigan Tech Open Sustainability Technology Laboratory (MOST), development of a single piece of collaboratively shared laboratory hardware has an "astronomical" return on investment (ROI) to the scientific community. Dr. Pearce performed a case study of "a syringe pump released under open license" in order to calculate the ROI of an open source hardware design. His calculations, based on the number of downloads over five months and the standard cost of a traditionally manufactured syringe pump, estimate a ROI "ranging from 460% to over 8300%", a potential savings in millions of dollars [118].

Other labs across the country have successful open-source 3D printing labware stories [119]. Dr. Jordan Miller at Rice University designed an orbital shaker that he estimates cost him approximately $140 [120]. Dr. Peter Allen at the University of Idaho estimates that 3D printing has saved him 50-90% in electrophoresis components. According to a recent manuscript by Coakley and Hurt, both Director Collins at the NIH and engineers at the National Center for Advancing Translational Sciences (NCATS) support the development of 3D printing parts, citing that small parts lead to large savings [119].

Beyond the needs of the community within the United States, such useful laboratory equipment, like the commonly used stage-top incubator, can be created and shared with the scientific community in developing countries where funding or materials

are of great issue [121]. For example, Michael Molitch-Hou shares “How a medical clinic in the Bolivian Rainforest might use 3D printing” on the 3D Printing Industry website [122]. He states that 3D printing can directly help clinicians and patients through devices like finger splints, prosthetics, and encouraging good foot care. Away from direct care, Molitch-Hou also states that such clinics can benefit from 3D printing by “providing lab equipment and medical models” to their healthcare students.

Open-source developers need to also be aware of universities in a “resource-challenged context” like Pontificia Universidad Católica del Perú where biological laboratory equipment is minimal but 3D printing is available or those in sub-Saharan Africa where “Open Labware may make the crucial difference between having some usable equipment to work with and having none at all” [123]. According to Baden *et al*. in 2015, such universities benefit extremely from the open-source movement. They introduced three-week neuroscience summer schools in Uganda and Tanzania where participants came into contact with 3D printed lab tools like pipettes, manipulators and microscope adapters. Baden *et al* found that “Hands on exposure allowed students to judge for themselves which designs would be useful in their own research and teaching activities.” They also gave a survey in which participants rated the usefulness of the open labware designs “at least nine out of ten on average (n = 33)” [123]. Clearly, open-source labware is beneficial to many aspects of the scientific community as it allows others to locate and redesign files they also need to conduct their research.

8.2 The PICS Design

The second research need, addressed in Chapters 4 and 5, came out of a collaborative laboratory. Their desire was for a device which would make imaging their curved sample easier. They asked us “How to hold a sample to enable quick repositioning of a curved tissue sample for the best imaging results?” This need was due to the fact that curved tissue, such as the lateral ventricular wholemount, can be especially difficult to image as microscope cameras are designed to image in planes. Protocols for imaging the LVWM call for securing the tissue to a plate by pinning or adhesion, which prevents tilting or repositioning the curved sample on the microscope. Thus, PICS was designed to enable the imaging of curved surfaces, specifically wholemount brain imaging.

Though PICS gets its name from imaging curved surfaces, only one curved tissue surface has been tested with the device. In order to assess the benefit to other areas of research, PICS needs to be used with other examples of curved tissue. For example, neonatal retinas are a naturally curved, easily accessible surface that is cited as an excellent model to study angiogenesis [124]. Retinal ganglion cells have also been used to study voltage gated calcium channels, making it a model for electrophysiological studies as well as developmental biology and regeneration (angiogenesis). Wholemount retinas are usually prepared by cutting open the retina into petal shaped parts and laying it flat onto microscope slides for 2D (planar) imaging [124]–[126]. However, the tissue itself is described as cup-shaped. PICS poses potential benefit by allowing a 3D imaging setup without the need to cut tissue to lay it flat.

PICS has also only been assessed at one size with one viability controller type. As mentioned in Chapter 5, the final design consideration was that PICS needed to connect

to a standard environmental controller with benefit that the baseplate can be redesigned to cover another commercially available environmental control system by simply changing the dimensions of the plate. It was believed that designing PICS in this way made it a versatile attachment. Again, as laboratories begin to use PICS, it is expected that the baseplate will need to be adjusted to fit a variety of controllers across different laboratories. Recalling the benefits of open-source labware, one strong advantage to laboratories is the ability to remake models to their specifications so long as the laboratory has the modelling software.

PICS potential also goes beyond neuroscience. The PICS design supports collaborative effort across scientific areas of expertise as PICS can be easily printed and machined for use in other laboratories where imaging of curved tissue, especially wholemount imaging, is necessary. As previously mentioned, wholemount retinas could be a potential candidate as benefitting from this device, branching into developmental biology, electrophysiology, and regenerative medicine laboratories. However, kidneys, lungs, and liver all have curved shapes that may be of interest to laboratories studying the form and function of these tissues. Part of the benefit of having a design like PICS is that its dimensions can be changed to fit different tissue sizes so long as the principles of the design (that the weight is kept in the center and that the archway is created according to the curvature of the imaging plane) are kept the same. As different laboratories begin to use PICS, it is expected that individual laboratories may need to resize and/or potentially even reshape the basket to fit their tissue needs.

8.3 The Glutamate Microelectrode Array

The final research need addressed in this work was the facilitation of a larger collaborative effort, as discussed in Chapters 6 and 7, with the understanding that extracellular levels of glutamate affect seizure activity. In this case, we tested a commercial probe, R1 from CenMeT, using two cell lines: astrocytes and CRL-2303 glioma cells. We showed that the sensor takes measurements in a verified range of 10 - 570 μM Glu *in vitro* without the need for cell lysate and that the overall sensitivity of the probe is 4.4 ± 0.3 pA/uM. We also compared astrocytes and CRL-2303 glioma cells to determine if probes were capable of distinguishing the impaired uptake in glioma cells from the normal uptake in astrocytes. It was determined that the combination of slower V_{max} in CRL-2303 cells as well as faster rise times can be used to indicate impaired uptake in glioma cells.

Astrocytic Glu uptake is typically measured using a biochemical assay, such as microdialysis for *in vivo* studies and a colorimetric assay for *in vitro* studies. Such assays require either cell lysate or cell culture medium that is removed from cells. Though these assays are highly sensitive, they do not provide a real-time measurement of Glu clearance dynamics. Temporal quantification of extracellular Glu release and uptake are necessary when studying disease characteristics, especially if impaired uptake is indicated. For instance, it has been suggested that lack of real-time Glu correlation has caused errors in identifying molecular mechanisms in Huntington Disease [127]. Thus, it would be beneficial to compare the real-time recordings of the coated probe to a biochemical assay such as a colorimetric assay. As we have data from a colorimetric assay for both the

astrocytes and CRL-2303 cells [Dr. Decoster, unpublished], the next step in determining probe capability will be to compare the colorimetric data to data gathered by the probe.

Though these experiments were performed with probes centered above the cells in dishes, future *in vitro* work should focus on growing cells upon the probes or platinum sites for more overall accuracy. Differences in probe site recordings may be due to diffusion differences as each site is 150 μm higher than the previous site. Also, distance between the cells themselves and the probe may cause delays in reading which could be prevented by growing cells on top of the MEA.

Maintaining the cell environment was important due to the length of these experiments, exceeding five hours. The MEAs were sensitive to changes in temperature as well as sensitive to electrical noise from lights, motors, and other equipment in the lab. The addition of the Ferriday cage as well as the homemade water bath and environmental setup could benefit researchers using long *in vitro* experiments with such probes. As previously stated, the R1 probe is a commercial probe used for several different experiments that range from glutamate, to dopamine, to glucose studies. Cutting down on interference in the pA range can be difficult. Thus, having a previously determined method to cut noise and ensure proper signal is beneficial to laboratories attempting similar methods.

8.3.1 Further Impacts

The real-time measurements of the R1 probe were pursued here under the umbrella of epilepsy research. As mentioned in Chapter 7, it has been suggested that impaired uptake contributes to epileptic seizures [108]–[110]. Glutamate imbalance in glioma has also been implicated in seizure activity for patients with brain tumors. The

utility of the probe in determining differences in uptake between normal astrocytes and the CRL-2303 line shows that such a probe will be beneficial for monitoring the impairment of uptake in seizure activity in an *in vivo* model. Rat models are already being prepared for this purpose.

However, the monitoring capabilities of these sensors have potential in the clinic as well. Some patients suffering from epilepsy are already monitored via electrode arrays for potentials that could indicate an oncoming seizure. Correlation of potentials with glutamate levels could help us to understand the onset and continuation of seizures as well as provide individual patient data to the clinician.

Characterization of the glioma cells using these probes have farther reaching impacts as well. It is understood that glioma cells release glutamate via the System X^c pathway and that this release causes excitotoxic reactions in the nearby normal neurons, leading to neuronal death. It is possible that future sensors could medically monitor areas where glioma has been found and surgically removed, as glioblastoma multiforme has high recurrence rates. In this case, electrode arrays would act as glioma recurrence indicators or monitoring sensors, helping clinicians by providing patient Glu level information around the area of original tumor resection.

8.4 Conclusions

In this work, we showed that a cellular environment to keep cells healthy and viable for five hours on a microscope could be created using FDM printing (Chapter 3). Design criteria were that it maintained correct temperature, high humidity and proper pH to control the environment as discussed in Chapter 2. Results indicated that cells would

maintain viability for up to five hours, but redesigns needed to be made for extending viability past five hours.

An imaging enhancement termed PICS (Planar Imaging of Curved Surfaces) was also introduced (Chapter 5). For this project, design criteria were that the device stabilized the tissue for imaging while allowing fluid flow around the tissue and facilitate rotation of the naturally curved tissue with respect to the microscope objective lens. Three further considerations of the PICS device were: (1) that it should not add undue shear stresses to the sample tissue, (2) that there should be no unintentional translation, (3) that it should attach to a standard microscope temperature controller in such a way that it does not interfere with temperature controls and does not move unintentionally. Results indicate successfully movement of tissue with respect to imaging plane to facilitate productive image capture.

Finally, in Chapter 7, a microelectrochemical array was used to explore differences between glioma and normal astrocyte glutamate levels. Results showed that glioma and normal astrocyte glutamate uptake can be tracked in real-time and compared using the probe. The distinction between glioma cells and astrocytes relies on three indicators: (1) a signal more stepped like in appearance, closer to that of a calibration curve, coming to a steady baseline faster and having a shorter FDHM, is a first indication of impaired uptake; (2) a signal showing a lower k constant, indicating a slower overall clearance rate, (3) faster rise times corresponding with a slower maximum elimination rate. These corresponding factors together indicate impaired uptake in glioma cells versus normal astrocyte glutamate uptake.

APPENDIX A

EXTENDED METHODS AND RESULTS

A. 1 Flow Cytometry Experiment Principles and Methods for Analysis

To correctly enable the performance and analysis of a flow cytometry experiment, principles of flow cytometry must be well understood. The following are the principles used both to acquire and assess the flow cytometry data presented in this work.

A.1.1. Excitation Laser and Fluorescence Channels

Since the channels that will record data are predetermined in a flow cytometry experiment, it is important to choose the best channels to assess your data before running the cells through the machine. The CytoFLEX laser configuration can be seen in Figure A-1. The channels pictured have bandpass (BP) filters that allow transmission within the range listed, the first number being the center of range and the second being the total range around that number.

Excitation	Fluorescence Channels	Fluorochromes
488nm	525/40 BP	FITC, Alexa Fluor 488, CFSE, Fluo-3
	585/42 BP	PE, PI
	610/20 BP	ECD, PE-Texas Red, PE-CF594, PI
	690/50 BP	PC5, PC5.5, PerCP, PerCP-Cy5.5, PI
	780/60 BP	PC7
638nm	660/10 BP	APC, Alex Fluor 647, eFluor 660
	712/25 BP	APC-Alexa Fluor 700, Alexa Fluor 700
	780/60 BP	APC-Alexa Fluor 750, APC-Cy7, APC-H7, APC-eFlour 780
405nm	450/45 BP	Pacific Blue, V450, eFluor 450, BV421
	525/40 BP	Krome Orange, AmCyan, V500, BV510
	610/20 BP	Violet610, BV605, Qdot 605
	660/10 BP	Violet660, BV650, Qdot 655
	780/60 BP	Viole780, BV785, Qdot 800

Figure A-1: CytoFLEX Channel Configuration. PI is indicated for 488nm excitation across all PE channels. Reprinted from [128].

Since the fluorochrome used was PI, it was necessary to make sure that at least one of the PI channels was operational before experimentation. The 585/42 BP channel, called PE, was available for assessment and so was chosen.

A.1.2. How Flow Cytometer Measurements Are Taken

Figure A-2, A depicts the quantification of fluorescence when a cell passes in front of the excitation laser. For each fluorescing event, a pulse is created that measures the voltage, often referred to as intensity, of the photoelectrons produced when photons hit the photocathode of the detector. Thus, it is the voltage that is measured and quantified by the analog to digital converter found in the flow cytometer.

Since the voltage is measured over time, three measurements that can be quantified according to the pulse are pulse area, pulse width, and pulse height. The voltage is considered to be directly correlated to the intensity of the fluorescence, meaning that the higher the peak, the more the stronger the fluorescent signal. The pulse width is also referred to as the "time of flight" and correlates to the size of the event, or cell, passing the laser. The pulse area is the integral of the pulse and is considered the more accurate representation of the fluorescence event. Thus, the quantification of events is most often reported in terms of area. In an experiment, many pulses are added together to give an overall picture of the fluorescence measured. Figure A-2, B depicts basic interpretation of a histogram of pulse events versus fluorescence intensity.

A

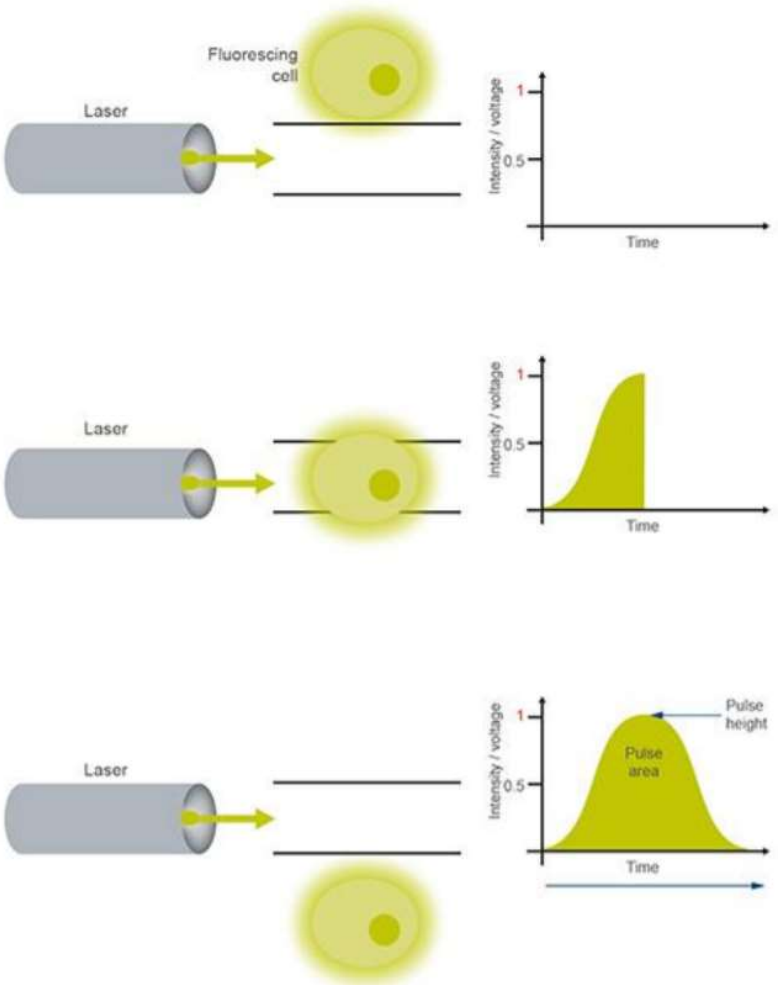

B

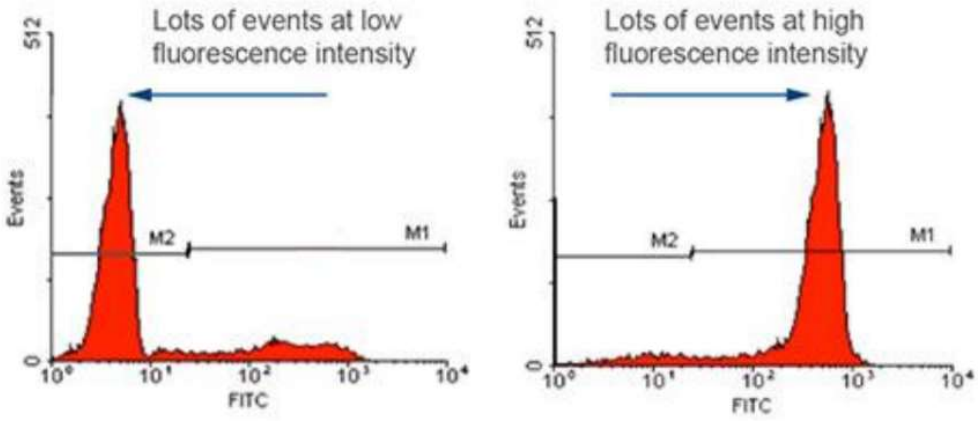

Figure A-2: Flow Cytometer Measurement Principles. A. Detectors in a flow cytometer create voltage over time pulse. Reprinted from [129]. B. Interpretation of flow cytometry histogram. Reprinted from [129].

It is very important to understand that cells autofluoresce when exposed to laser light in the UV to blue range, 355-488nm. This is due to cyclic rind compounds and aromatic amino acids found in the cell. Autofluorescence will emit in the blue to green range, 350-550nm, and can be detected by the flow cytometer fluorescence detectors [130]. For this reason, cells that are untagged by a fluorochrome can still be detected by comparing the forward scatter or side scatter by a fluorescence detector such as FITC. Autofluorescence will always be low intensity, and so will be the peak furthest to the left in a histogram, such as Figure A-2, B.

A.1.3 Gating for the Most Accurate Data

Gates are created in the flow cytometry analysis software to cut down event populations and ensure reasonable data interpretation. Three common gates were used before every flow cytometry experiment in this work: the singles gate, the time gate, and the forward and side scatter gate, in that order.

The first gate applied is the singles gate. From the principles mentioned previously, it should be understood that flow cytometry detection is designed for single cell events and not cells stacked together or in clumps. This will cause incorrect data expression as pulse width and area are affected by multiple cell passage.

To correct for multiple cells, called doublets or triplets, passing at the same time, a singles gate is often used. This is done by comparing a dot plot of the height by area. Figure A-3 is an example from the cell viability experiment. As depicted, there should be a pronounced break in the dot plot where pulse height remains constant or slowly increases but pulse area grows steadily larger, looking like two tails. The larger area

indicates doublets and triplets. The gate is created around the majority of events before the break.

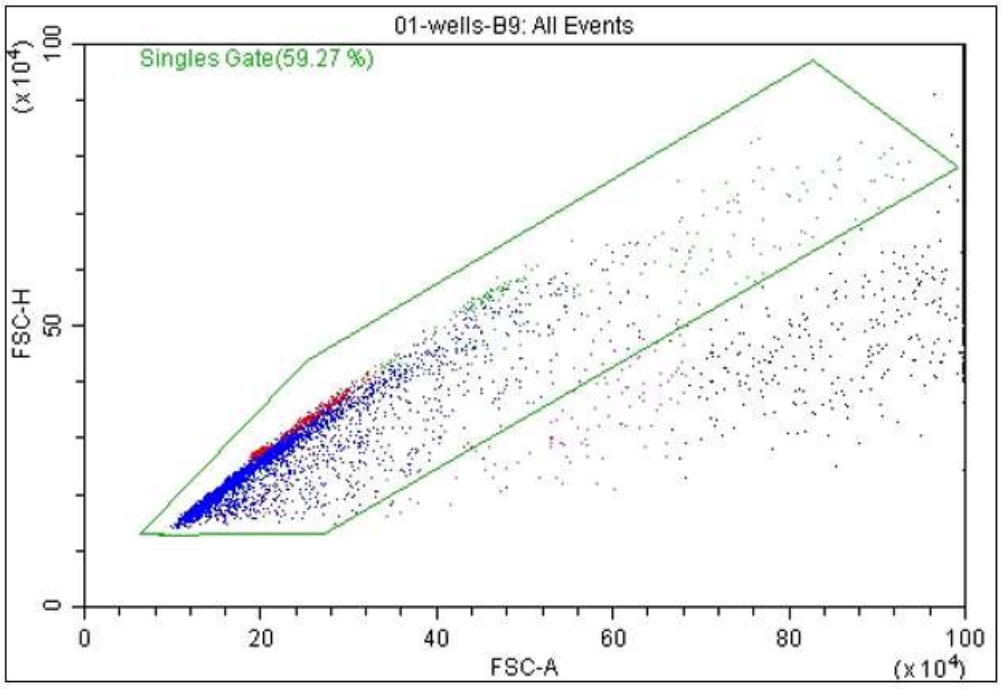

Figure A-3: Singles Gate. Viability experiment day 6-5-2017. Blue represents live cells, red: fluorescing (dying) cells, and green: cells included in the singles gate that were excluded in other gates later.

The next gate applied is the time gate. For the cytometer to work properly, a stable flow of cells in sheath fluid must be established. If flow rate is unstable, the data may be affected with incorrect widths and extended areas. A forward scatter or fluorescence detector versus time dot plot shows the flow of cells during the length of the experiment. Figure A-4 depicts two forward-scatter versus time plots. In A-4, A, the flow is smooth and no time gate is necessary. In A-4, B, the flow has been interrupted at several points during the experiment, bringing results into question. Such an unstable flow should not be used in the cohort.

A.

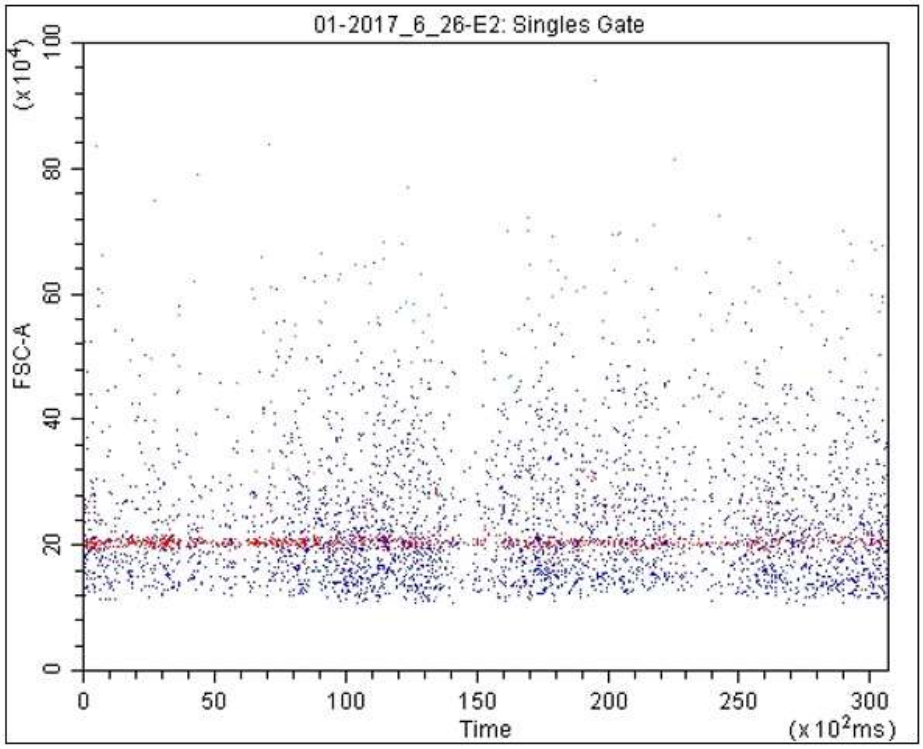

B.

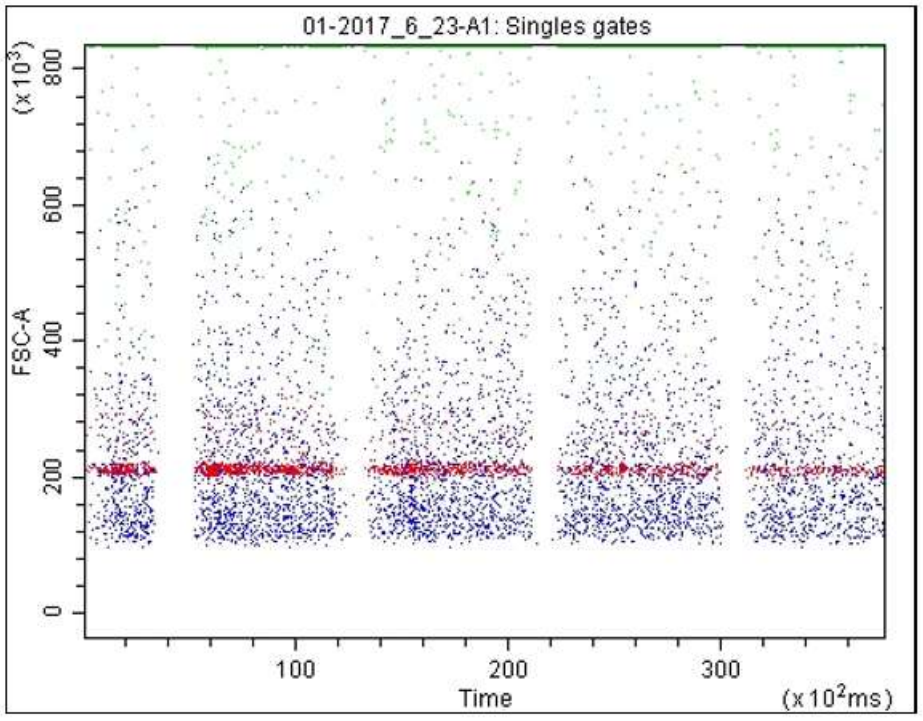

Figure A-4: A. Forward scatter versus time dot plot showing smooth flow rate of cells across detectors. No time gate needed. B. Plot depicting break in flow rate of cells. Reveals questionable data. Time gate necessary.

Finally, the forward and side-scatter gates are used to cut outliers out of the data. Using a contour plot of the forward and side scatter, the events are grouped by pulse area, indicating where the majority intensities lie. Incorporating approximately 90-95% of the data into the F&S gate eliminates the 5-10% that would be outside reasonable intensity range for that data set. Normally, this is a gating strategy used to also exclude autofluorescence. Since we were interested in unmarked and autofluorescing cells, this gate was not made to exclude them. Figure A-5 depicts the forward versus side scatter gate for a cell viability experiment. Only after all three gates have been applied has the remaining data been analyzed for viability.

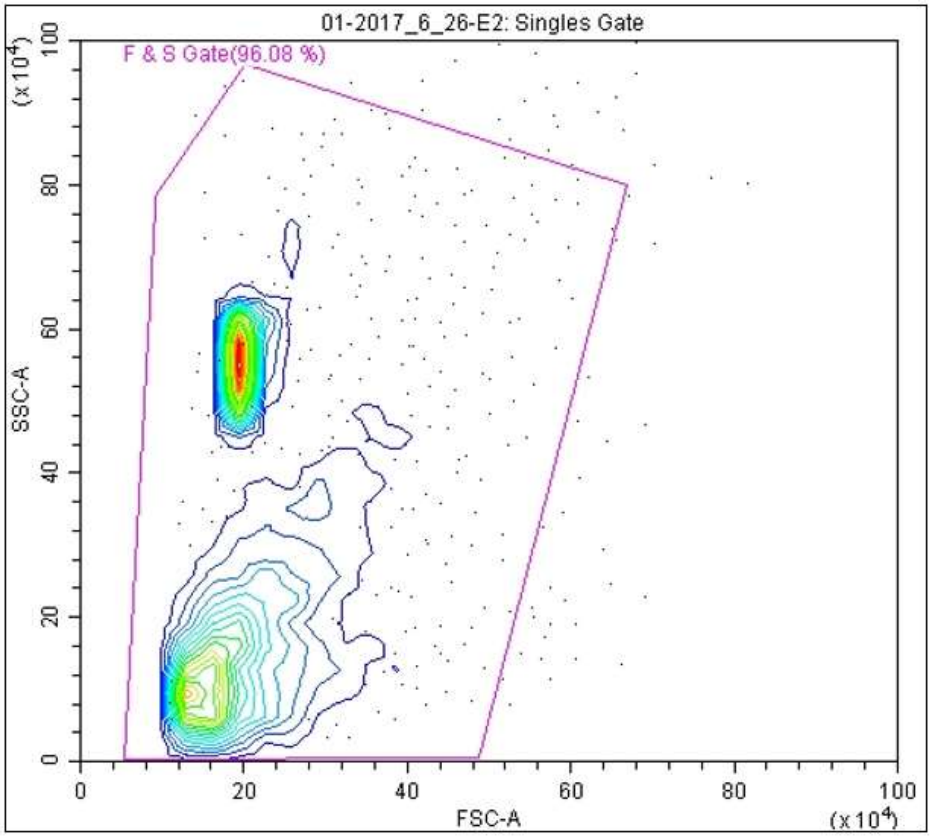

Figure A-5: Side scatter area versus forward scatter area contour plot. Depicts all acquired data. Majority conserved with 90-95% gate. Outliers rejected.

A.1.4. Data Acquisition

For cell viability, the forward scatter area (FSC-A), side scatter area (SSC-A), fluorescein area (FITC-A) and R-phycoerythrin area (PE-A) histograms were employed. A univariate plot (histogram) gives the event count according to the intensity of the scattered light or fluorochrome. The FITC-A channel indicates a low intensity (unmarked) fluorescence peak followed by a high intensity (marked) fluorescence peak.

APPENDIX B

PROTOCOLS

B.1 Protocol for Temperature Test using 3D Warmer

Objective: take a total of three, 24-hour temperature tests at each temp setting: 42˚, 38˚, & 35˚ for both a PLA printed system and an ABS printed system.

To start a test:

1. Make sure pump, tubing and warmer system are on benchtop as originally shown for setup.
2. Before handling any media, make sure have on gloves.
3. From refrigerator, take premade NSC media.
    a. Using pipet aid, put 5mL of NSC media into 35mm dish.

        *Remember, 35mm dishes and pipettes can be found on shelf above setup. If cannot find 35mm dishes, whole box located on second shelf.

    b. Label the top of the dish and place media in benchtop incubator for warming.

    c. Put NSC media back into refrigerator.
4. Make sure all connections are secure and that warmer system is taped down.
    a. Power on t-pump.

    b. Make sure pump is set to correct temperature.

    c. Look at the warmer for a minute or two to make sure there are no visible leaks from any connections.

    d. Temperature readings should begin exactly 15 minutes after pump is turned on, so try to time it that way.
5. Open HP laptop and power on.
    a. Open Arduino Software.

        1. File → Open → Temp_Only

2. Make sure Arduino is plugged into laptop.

3. Press upload on Arduino screen to clear any other programs that may have been used.

c. Open PLX-DAQ from desktop.

1. Click on PLX-DAQ spreadsheet

2. At top, will say security warning (macros)

a. Click Options.

b. Click Enable the content, then okay.

3. Macro will pop up on top of spreadsheet.

4. Rename Simple Data sheet as: 24hr_(temp running at)_(number run)_(date of run begin) Ex: 24hr_42_1_2017_3_15

5. Now click Connect on macro.

* First reading should be immediate.

6. Can click disconnect and clear columns in preparation experiment.

6. At the 15-minute mark, remove media dish from incubator.

a. Place into back well of warmer.

b. Cover warmer with dome.

c. Slide temp probe into the warmer and media.

* Remember, probe needs to be as close to center of dish as possible and needs to be immersed in the media. This will affect readings.**

d. Place 35mm dish cap over top of well.

7. Start temperature recordings by clicking connect on the PLX-DAQ macro.

a. Sit through at least the first two to three readings to ensure is running properly.

b. Place the please do not disturb sign on the warmer.

c. Clean up anything necessary in area.

8. Come in every so often during the day to check that the computer/Arduino/pump are all running smoothly.

   *Always check that the temperature probe is sitting immersed in media when come in. If not, rearrange so that is now immersed in media.

   *If anything is not working properly. Note it. Any changes at all in the experiment will result in a failed experiment that must be run again, so it's important to note if something has gone wrong.

To end a test:

1. Come in a few minutes before time-point end.
2. At time-point end, end the recording by hitting Disconnect on the PLX-DAQ macro.

   a. Save the data under the Experiment Data Folder on the Desktop.

   b. Save as the same name gave the spreadsheet. Ex. from above: 24hr_42_1_2017_3_15

   c. Once data is saved, shutdown the laptop.
3. Power off the t-pump.
4. Disconnect the Arduino from the HP laptop.
5. Remove the 35mm dish lid from the top of the warmer dome and set aside.
6. Remove the temperature probe from dome and clean with ethanol. Set aside.
7. Remove dome.
8. Remove 35mm dish from well.

a. Spray media left in well with Ethanol, then pour down sink with water running.

b. Place 35mm dish and top into biohazard bag.

c. Spray well and warmer dome with Ethanol for cleanliness.

9. Once everything is saved, powered down, and cleaned, you may leave the setup on the benchtop unless otherwise asked to place it back on the microscope.
10. If asked to do so, the warming system needs to be placed back on the microscope and connected to ensure no water leakage before leaving.

B.2 Protocol for Cell Viability Test using 3D Warmer

Objective: To take a total of three each: 2, 5, and 12-hour cell viability tests.

To start a test:

1. Make sure pump, tubing and warmer system are on benchtop as originally shown for setup.
2. Before handling any media, make sure have on gloves.
3. From refrigerator, take premade NSC media.
    a. Using pipet aid, put 5mL of NSC media into 35mm dish.

        *Remember, 35mm dishes and pipettes can be found on shelf above setup. If cannot find 35mm dishes, whole box located on second shelf.

    b. Label the top of the dish and place media in benchtop incubator for warming.

    c. Put NSC media back into refrigerator.
4. Make sure all connections are secure and that warmer system is taped down.
    a. Power on t-pump.

    b. Make sure pump is set to correct temperature.

    c. Look at the warmer for a minute or two to make sure there are no visible leaks from any connections.

    d. Temperature readings should begin at least 15 minutes after pump is turned on, so try to time it that way.
5. Open HP laptop and power on.
    a. Open Arduino software.

        1. File → Open → Temp_Only

        2. Make sure Arduino is plugged into laptop.

3. Press upload on Arduino screen to clear any other programs that may have been used.

c. Open PLX-DAQ from desktop.

1. Click on PLX-DAQ spreadsheet
2. At top, will say security warning (macros)
   a. Click Options.
   b. Click Enable the content, then okay.
3. Macro will pop up on top of spreadsheet.
4. Rename Simple Data sheet as: (hrs running for)hr_viable_(number of round run)_(date of run begin) Ex: 12hr_viable_1_2017_3_15
5. Now click Connect on macro.
   * First reading should be immediate.
6. Can click disconnect and clear columns in preparation experiment.

6. Bring cart upstairs for imaging.

a. Setup Camera by taking out of cart and placing on top of the Nikon Eclipse TS100 camera port. Use the c-mount from the cart for the camera port.

b. Turn on laptop.

1. Plug in camera to laptop
2. Open Amscope app.
3. Click camera to begin connection with laptop.

c. Get cells out of incubator.

d. Image each of the three dishes at least three times in random locations.

1. Be sure to switch from Bino to Photo on the microscope to image.

e. When finished imaging, pick up camera and place back into cart.

7. Place Dish 1 back into the incubator. Take Dishes 2 and 3 down to Room 140.
8. In Room 140.

    a. Check warmer once again for leaks.

    b. Place Dish 2 into front end of warmer and Dish 3 onto benchtop (in Petri Dish is fine).

    c. Place the warmed media dish from earlier into the back end of the warmer.

    d. Place dome pieces over the warmer (making sure that the gas will flow over the cells).

    e. Click dome pieces into place and gently slide down over warmer (make sure that cell dish does not tip. If does, take a pipette tip and gently push inside of dish away from center.)

    f. When warmer top all the way down, place dish top back onto warmer opening.

    g. Push temp probe into place, making sure in media in center of media dish. When temp probe in place, put media dish cap onto warmer opening.

9. Start temperature recordings by clicking connect on the PLX-DAQ macro.
10. Connect gas hose firmly to dome.

    a. Turn on gas, remembering is a two-stop system. Make sure gas is running all the way through the table stand. The table stand stop should read 1.5 bars.

11. Sit through at least the first two to three readings to make sure is running properly.
12. Place the please do not disturb sign on the warmer.
13. Clean up anything necessary in area.

14. Come in every so often during the day to check that the computer/Arduino/pump are all running smoothly.

    *Always check that the temperature probe is sitting immersed in media when come in. If not, rearrange so that is now immersed in media.

    *If anything is not working properly. Note it. Any changes at all in the experiment will result in a failed experiment that must be run again, so it's important to note if something has gone wrong.

To end a test:

1. Come in 30 minutes before time-point end.
2. Bring cart upstairs to setup.

    a. In hood, need two racks, aspirator, Trypan blue, and pipettes/aid.

    b. Warm in 37˚C bath: trypsin, PBS, and media at 15 minutes until experiment end.

    c. Set up camera to take pictures as before.

    d. In common lab, perform preparation for flow cytometry readings.
3. In Room 140: at time-point end, end the recording by hitting Disconnect on the PLX-DAQ macro.

    a. Save the data under the Experiment Data Folder on the Desktop.

    b. Save as the same name gave the spreadsheet. Ex. from above: 12hr_viable_1_2017_3_15
4. Power off the t-pump.
5. Disconnect the Arduino from the HP laptop.
6. Remove the warmer dome.

7. Remove Dish 2 and place cap back onto the dish. Place Dish 2 into Petri dish with Dish 3.
8. Bring Dish 2 & 3 upstairs.
    a. Place Dish 1 into Petri Dish with Dishes 2 & 3.
    b. Reimage all dishes in random locations. (minimum of three images)
9. Remove media from Dishes and place into separate, labelled 50mL conical tubes for pH testing.
10. Wash with 1mL PBS.
11. Add 1mL trypsin and let sit in incubator for four minutes.
12. While cells are in incubator:
    a. Perform pH test on removed media.
    b. Label separate 15mL conical tubes: 1, 2, & 3
    c. When trypsin finished, add 2mL media back to the trypsin.
13. Take up trypsinized cells and media. BE SURE to put each set into the properly labeled conical tube!!!!
14. Wash w/ 1mL media and place into tube.
15. Spin cells @ 160 xg for seven minutes.
    a. Aspirate supernatant.
    b. Resuspend cells in 1mL FACS solution.
16. Perform a Flow cytometry test[1] for each conical tube.
17. Clean everything in hood and bring cart back down.

---

[1] Protocol found in Section B.3 of this appendix.

18. In Room 140:
    a. Remove the temperature probe from dome and clean with ethanol. Set aside.
    b. Remove 35mm dish from well.
    c. Spray media left in well with Ethanol, then pour down sink with water running.
    d. Place 35mm dish and top into biohazard bag. Spray well and warmer dome with Ethanol for cleanliness.
19. Once everything is saved, powered down, and cleaned, you may leave the setup on the benchtop unless otherwise asked to place it back on the microscope.
20. If asked to do so, the warming system needs to be placed back on the microscope and connected to ensure no water leakage before leaving.

B.3 Protocol for Flow Cytometry Live/Dead with PI (Propidum Iodide)

30 minutes prior to cell test ending, in common lab:

1. Start computer and CytoFLEX→Open user →Open CytExpert
2. In the CytExpert program →Cytometer → prime→system startup program → just pipette three wells w/ DI water (Millipore only) approximately eight minutes.
3. Next begin QC → one well only→ start QC (QC means quality control) → chose lot number →eject→make sure plate keyed in place→plate settings→select well→click start→get report (If pass, pass. If fail, fail.)
4. If fail due to prime, there is air in line → go to cytometer → click standby → click prime.
5. Now CytoFLEX is ready for experiment.
6. Prepare experiment: File→New experiment→get blank page→choose your graphic data→ select plate (square box with four dark holes).
7. You are now ready to perform the flow cytometry experiment when the cells are prepared.

Once cells are prepared in 1mL FACS solution:

8. Add 10uL of 100ug/mL PI stock from recommended final concentration of 1ug/mL:
    a. c1=100ug/mL,c2 = 1ug/mL,v2=1mL
    b. v1= (1mL*1ug/mL)/(100ug/mL) = .01mL = 10uL
9. Immediately bring cells into Cyto room.
10. Fill sample wells with 250uL of cell solution.

11. In CytExpert: →select samples (click and drag) →set as sample wells→When ready, click Record for experiment.
12. Cytometer will record data. Save file once finished.

Cleaning at end of experiment:

13. three Daily Clean wells and three DI wells
14. For setting DI and Daily clean wells → go to set well → then click stopping rules → delete events→ set as 130sec → now run Daily Clean→Shut down computer and CytoFLEX.

B.4 Protocol for Tail Vein Injections (Texas Red Dextran, TRD)

1. Prepare the TRD.
    a. Found in the -20˚C Freezer.
    b. Prepare in 1.5 mL Eppendorf Tube with aluminum foil wrapping.
    c. Calculations are:

        1 mL sterile saline to .01g of TRD

        *Use 1 mL syringe for saline instead of graduated cylinder
    d. Saline is kept in the supply closet.

        **Be sure to write non-sterile on the tube, as there will be extra.
    e. Only need 0.1 mL for mouse tail vein injection (TVI)

        ***If not using the standard for TVI, can inject up to 1% of rodent's body weight as maximum.
    f. Vortex TRD well for one minute. TRD does not mix well.

        ***May have to vortex for longer if powder is still chunky.
    g. Keep in fridge wrapped in aluminum.
2. Prepare animal restraint.
3. Prepare warm tap water in waste beaker.
4. Prep 1 mL syringe and 30 (1/2) gauge needle.
5. Pull .1 mL into syringe… will be viscous: Be sure to get out ALL AIR!

    ****Can be fatal if any air bubbles.
6. Put mouse into animal restraint. Hold tail, up to feet, in warm water for one minute.
7. Lay animal in restraint onto table belly side up.

8. Swab the tail with alcohol to prevent infection.
9. Beginning at about mid tail, look for the lateral tail veins. If mouse flips over, right him.

   *****Only lateral tail veins should be used for injection!
10. Begin sliding needle into tail vein. Will be Just Under the skin.

    ****Vein is shallower than you might think. Experts say use 15˚ angle for injection.
11. Slowly, inject the TRD into the vein.
12. *****Will know going into vein because vein becomes darker down the tail. You may have a little blossom, but no puckering of skin.
13. If skin and flesh begin to bubble, then pull out and re-inject further down the tail closer to the base. This means the needle is NOT in the tail vein.

    ******Push syringe very slowly… Do Not want to blow vein!

B. 5 Protocol for Whole-Mount Explant Excision

1. Turn on Germinator 500. Prep surgery tools by placing in cool Germinator 500. When green ready light from Germinator 500 turns on, wait 15 seconds then remove tools.
    a. Tools needed for Explant:
        1. Pair large scissors
        2. Pair medium scissors
        3. Pair fine scissors
        4. Pair curved holders
        5. Scalpel handle
        6. two pair fine curved forceps
        7. Pair fine scissors
        8. Glass petri dish
2. Place tools in Benz-Al for 15 minutes.
3. Prep anesthesia. Use 1 mL Isoflurane for every mouse with sacrifice.
4. Place 15 mL per mouse PBS (or media) in 50 mL conical tube. Put conical tube into 37˚C incubator.
5. Prep stereoscope and light. Plug in light.
6. Take tools from Benz-Al to shop towel to dry.
    a. Place surgical tools on surgery table.
    b. Place microdissection tools next to stereoscope.
7. Acquire TRD from refrigerator and prepare .1mL TRD.
8. Turn on hot water and prepare 500mL plastic beaker for hot water.

9. Choose mouse.
10. Weight mouse and write down weight.
11. Restrain mouse and begin lateral tail vein injection.
12. Place mouse back into carrying cage… Wait three minutes.
13. Take PBS from incubator and place into glass petri dish.
14. Place mouse into anesthesia chamber.
15. Sacrifice and remove brain. Place into warmed PBS.
16. The rest is performed underneath the stereomicroscope.
    a. Remove Olfactory Bulb.
    b. Make a coronal cut across both hemispheres at the posterior-most aspect of the interhemispheric fissure. You should be able to see the caudal hippocampus of both hemispheres from this cut.
    c. Divide the brain into two hemispheres along the interhemispheric fissure.
    d. Grasping one hemisphere with fine forceps, release the hippocampus from the overlying cortex with the scalpel: Insert knife into ventricular space between the cortex and hippocampus dorsally. Cut toward the midline to separate the cortex and cut a small corner of the cortex away from where the hippocampus was released
    e. Release the hippocampus from the lateral wall: After reaching the ventral-most extent of the lateral ventricle at this position, you may either visualize or feel where the cortex again wraps around, this time reflecting back medially, to join the hippocampus. Another cut must be made in this

position to completely release the hippocampus or medial wall of the lateral ventricle from the cortex or lateral wall of the lateral ventricle.

f. Pull the hippocampus away from the cortex, medially and anteriorly. This will peel away easily like opening a book, revealing the inside of the lateral wall.

g. Make two cuts on either side of wall opening to completely release the medial wall section from the wholemount.

h. Proceed to cut away overhanging cortex to get a good view to the lateral wall.

i. Place wholemount tissue into PICS device for imaging.

APPENDIX C

IACUC APPROVAL

INSTITUTIONAL ANIMAL CARE AND USE COMMITTEE
Louisiana Tech University

January 29, 2016

Teresa Murray, Ph.D.
Biomedical Engineering
Louisiana Tech University
Campus Box #58

Dear Dr. Murray:

The Louisiana Tech University's Institutional Animal Care and Use Committee (IACUC) examined your protocol and via the committee review process approved your protocol entitled:

In Vivo Imaging and Neural Electrophysiological Recording in Rodent Brain for Biomedical Research

Your protocol has been assigned the following number: **2016-01**. All changes and procedures have been noted. If changes to your research are necessary, please know you will need prior approval from the IACUC. This protocol will expire **January 29, 2019.**

Please remember that you are required to keep adequate and accurate records of all procedures, results, and the number of animals used in this protocol for three years after termination of the project. These records must be available for review by the IACUC or state and federal animal use agencies. Each year in October you will be required to complete a summary of animals used for the United States Agricultural Agency (USDA). Note, that failure to follow this protocol as approved may result in the termination of research.

If you have any questions concerning the animal part of your research please contact me via email at eborn@latech.edu.

Sincerely,

Emily Born, IACUC Chair
Louisiana Tech University

BIBLIOGRAPHY

[1] "Fact Sheet: BRAIN Initiative | whitehouse.gov." [Online]. Available: https://obamawhitehouse.archives.gov/the-press-office/2013/04/02/fact-sheet-brain-initiative. [Accessed: 18-Oct-2017].

[2] "Mission - The BRAIN Initiative." [Online]. Available: http://www.braininitiative.org/mission/. [Accessed: 18-Oct-2017].

[3] National Academy of Engineering Committee, "NAE Grand Challenges For Engineering," 2008 [Updated 2017].

[4] "Discover 3D Models | NIH 3D Print Exchange." [Online]. Available: https://3dprint.nih.gov/discover?terms=&field_model_category_tag_tid%5B%5D=93&field_model_license_nid=All&sort_by=created&sort_order=DESC&items_per_page=24. [Accessed: 18-Dec-2017].

[5] "Temperature, CO2, and pH in Cell Culture Media." [Online]. Available: http://www.biospherix.com/cytocentric/411-temperature-co2-and-ph-in-cell-culture-media.html. [Accessed: 18-Oct-2017].

[6] Gibco, "CELL CULTURE BASICS Handbook," ThermoFisher Scientific, 2010.

[7] M. Vergara *et al.*, "Differential effect of culture temperature and specific growth rate on CHO cell behavior in chemostat culture," *PLoS One*, vol. 9, no. 4, p. e93865, 2014.

[8] D. C. Fish, J. P. Dobbs, and J. M. Elliott, "Effect of osmotic pressure, Na+/K+ ratio and medium concentration on the enzyme activity and growth of L cells in suspension culture," *In Vitro*, vol. 9, no. 2, pp. 108–113, Sep. 1973.

[9] C. K. Chua, K. F. Leong, and J. An, "Introduction to rapid prototyping of biomaterials," in *Rapid Prototyping of Biomaterials*, R. Narayan, Ed. Elsevier, 2014, pp. 1–15.

[10] I. Gibson, D. Rosen, and B. Stucker, "Introduction and Basic Principles," in *Additive Manufacturing Technologies*, New York, NY: Springer New York, 2015, pp. 1–18.

[11] ASTM International, "Committee F42 on Additive Manufacturing Technologies." [Online]. Available: https://www.astm.org/COMMITTEE/F42.htm. [Accessed: 25-Sep-2017].

[12] F. Calignano *et al.*, “Overview on Additive Manufacturing Technologies,” *Proc. IEEE*, vol. 105, no. 4, pp. 593–612, 2017.

[13] “About - RepRapWiki.” [Online]. Available: http://reprap.org/wiki/About. [Accessed: 26-Sep-2017].

[14] “File:FFF.png - RepRapWiki,” 2012. [Online]. Available: http://reprap.org/wiki/File:FFF.png. [Accessed: 26-Sep-2017].

[15] R. Gordon, “Trends in Commercial 3D Printing and Additive Manufacturing,” vol. 2, no. 2, pp. 89–91, 2015.

[16] D. M. Kulich *et al.*, “Acrylonitrile-Butadiene-Styrene Polymers,” in *Encyclopedia of Polymer Science and Technology*, Hoboken, NJ, USA: John Wiley & Sons, Inc., 2001.

[17] B. Patel and S. Chakraborty, “Biodegradable polymers: Emerging excipients for the pharmaceutical and medical device industries,” *J. Excipients Food Chem.*, vol. 4, no. 4, pp. 126–157, 2013.

[18] R. Suuronen, I. Kallela, and C. Lindqvist, “Bioabsorbable plates and screws: Current state of the art in facial fracture repair,” *J. Craniomaxillofac. Trauma*, vol. 6, no. 1, pp. 19-27-30, 2000.

[19] J. C. Middleton and A. J. Tipton, “Synthetic biodegradable polymers as orthopedic devices,” *Biomaterials*, vol. 21, no. 23, pp. 2335–2346, Dec. 2000.

[20] M. C. Wurm *et al.*, “In-vitro evaluation of Polylactic acid (PLA) manufactured by fused deposition modeling,” *J. Biomed. Eng.*, pp. 1–9, 2017.

[21] “FDM 3D Printing Materials Compared | 3D Hubs.” [Online]. Available: https://www.3dhubs.com/knowledge-base/fdm-3d-printing-materials-compared. [Accessed: 29-Sep-2017].

[22] V. Voziyanov, B. S. Kemp, C. A. Dressel, K. Ponder, and T. A. Murray, “TRIO platform: A novel low profile in vivo imaging support and restraint system for mice,” *Front. Neurosci.*, vol. 10, no. APR, pp. 1–11, 2016.

[23] Parallax Inc., “PLX-DAQ,” 2014. [Online]. Available: https://www.parallax.com/downloads/plx-daq. [Accessed: 06-Oct-2017].

[24] ATCC, “(atcc ® crl-2269 ™) Product Sheet,” Manassas, VA, 2015.

[25] U. S. D. of H. and H. S. National Institutes of Health, “NIH Stem Cell Information Home Page,” *Stem Cell Information*, 2016. [Online]. Available: https://stemcells.nih.gov/info/basics/1.htm. [Accessed: 21-Sep-2017].

[26] P. Ertl, D. Sticker, V. Charwat, C. Kasper, and G. Lepperdinger, “Lab-on-a-chip technologies for stem cell analysis,” *Trends Biotechnol.*, vol. 32, no. 5, pp. 245–53, May 2014.

[27] C. H. Waddington, *The Strategy of the Genes.* Routledge, 1957.

[28] K. Hochedlinger and K. Plath, “Epigenetic reprogramming and induced pluripotency,” *Development*, vol. 136, no. 4, pp. 509–523, 2009.

[29] H. Okano and S. Yamanaka, “iPS cell technologies: significance and applications to CNS regeneration and disease,” *Mol. Brain*, vol. 7, no. 1, p. 22, 2014.

[30] H. Shenghui, D. Nakada, and S. J. Morrison, “Mechanisms of Stem Cell Self-Renewal,” *Annu. Rev. Cell Dev. Biol.*, vol. 25, no. 1, pp. 377–406, Nov. 2009.

[31] S. Date and T. Sato, “Mini-Gut Organoids: Reconstitution of the Stem Cell Niche,” *Annu. Rev. Cell Dev. Biol.*, vol. 31, no. 1, pp. 269–289, Nov. 2015.

[32] “Brain Disorders: By the Numbers,” *McGovern Institute for Brain Research at MIT*, 2014. [Online]. Available: https://mcgovern.mit.edu/brain-disorders/by-the-numbers. [Accessed: 22-Sep-2017].

[33] F. C. Vinas and B. H. Ed. Kopell, “Penetrating Head Trauma,” 2015. [Online]. Available: http://emedicine.medscape.com/article/247664-overview. [Accessed: 21-Sep-2017].

[34] O. Lindvall, Z. Kokaia, and A. Martinez-Serrano, “Stem cell therapy for neurodegenerative disorders-how to make it work.” Nature Publishing Group, pp. S43–S50, 2004.

[35] G.-L. Ming and H. Song, “Adult neurogenesis in the mammalian brain: significant answers and significant questions,” *Neuron*, vol. 70, no. 4, pp. 687–702, May 2011.

[36] J. Altman and G. D. Das, “Autoradiographic and histological evidence of postnatal hippocampal neurogenesis in rats,” *J. Comp. Neurol.*, vol. 124, no. 3, pp. 319–335, Jun. 1965.

[37] P. Rakic, “Limits of neurogenesis in primates,” *Science*, vol. 227, no. 4690, pp. 1054–1056, 1985.

[38] M. B. Luskin, “Restricted proliferation and migration of postnatally generated neurons derived from the forebrain subventricular zone,” *Neuron*, vol. 11, no. 1, pp. 173–89, Jul. 1993.

[39] C. Lois and a Alvarez-Buylla, “Proliferating subventricular zone cells in the adult mammalian forebrain can differentiate into neurons and glia.,” *Proc. Natl. Acad. Sci. U. S. A.*, vol. 90, no. 5, pp. 2074–2077, 1993.

[40] P. S. Eriksson *et al.*, “Neurogenesis in the adult human hippocampus,” *Nat. Med.*, vol. 4, no. 11, pp. 1313–1317, Nov. 1998.

[41] D. A. Lim, A. D. Tramontin, J. M. Trevejo, D. G. Herrera, J. M. García-Verdugo, and A. Alvarez-Buylla, “Noggin antagonizes BMP signaling to create a niche for adult neurogenesis,” *Neuron*, vol. 28, no. 3, pp. 713–26, Dec. 2000.

[42] D. G. Herrera, J. M. Garcia-Verdugo, and A. Alvarez-Buylla, “Adult-derived neural precursors transplanted into multiple regions in the adult brain,” *Ann. Neurol.*, vol. 46, no. 6, pp. 867–877, Dec. 1999.

[43] F. T. Merkle, A. D. Tramontin, J. M. García-Verdugo, and A. Alvarez-Buylla, “Radial glia give rise to adult neural stem cells in the subventricular zone,” *Proc. Natl. Acad. Sci. U. S. A.*, vol. 101, no. 50, pp. 17528–32, 2004.

[44] T. Miyata, A. Kawaguchi, K. Saito, M. Kawano, T. Muto, and M. Ogawa, “Asymmetric production of surface-dividing and non-surface-dividing cortical progenitor cells,” *Development*, vol. 131, no. 13, pp. 3133–45, Jul. 2004.

[45] C. Englund *et al.*, “Pax6, Tbr2, and Tbr1 Are Expressed Sequentially by Radial Glia, Intermediate Progenitor Cells, and Postmitotic Neurons in Developing Neocortex,” *J. Neurosci.*, vol. 25, no. 1, pp. 247–251, 2005.

[46] R. James, Y. Kim, P. E. Hockberger, and F. G. Szele, “Subventricular zone cell migration : lessons from quantitative two-photon microscopy,” *Front. Neurosci.*, vol. 5, no. March, pp. 1–11, 2011.

[47] F. H. Gage, “Mammalian Neural Stem Cells,” *Science (80-.).*, vol. 287, no. February, pp. 1433–1438, 2000.

[48] G. E. Goings, V. Sahni, and F. G. Szele, “Migration patterns of subventricular zone cells in adult mice change after cerebral cortex injury,” *Brain Res.*, vol. 996, no. 2, pp. 213–226, Jan. 2004.

[49] B. Jablonska *et al.*, “Chordin-induced lineage plasticity of adult SVZ neuroblasts after demyelination,” vol. 13, no. 5, pp. 541–550, 2010.

[50] B. A. MacVicar and E. A. Newman, “Astrocyte Regulation of Blood Flow in the Brain,” *Cold Spring Harb. Perspect. Biol*, vol. 7, pp. 1–15, 2015.

[51] A. Alvarez-Buylla and D. A. Lim, “For the long run: maintaining germinal niches in the adult brain,” *Neuron*, vol. 41, no. 5, pp. 683–6, Mar. 2004.

[52] C. M. Morshead *et al.*, “Neural stem cells in the adult mammalian forebrain: a relatively quiescent subpopulation of subependymal cells,” *Neuron*, vol. 13, no. 5, pp. 1071–82, Nov. 1994.

[53] M. Tavazoie *et al.*, “A Specialized Vascular Niche for Adult Neural Stem Cells,” pp. 279–288, 2008.

[54] Z. Mirzadeh, F. T. Merkle, M. Soriano-navarro, and J. M. Garcia-verdugo, “Article Neural Stem Cells Confer Unique Pinwheel Architecture to the Ventricular Surface in Neurogenic Regions of the Adult Brain,” pp. 265–278, 2008.

[55] I. Kazanis *et al.*, “Quiescence and Activation of Stem and Precursor Cell Populations in the Subependymal Zone of the Mammalian Brain Are Associated with Distinct Cellular and Extracellular Matrix Signals,” *J. Neurosci.*, vol. 30, no. 29, pp. 9771–9781, 2010.

[56] B. A. Reynolds and S. Weiss, “Generation of neurons and astrocytes from isolated cells of the adult mammalian central nervous system,” *Science*, vol. 255, no. 5052, pp. 1707–10, Mar. 1992.

[57] H. Azari, M. Rahman, S. Sharififar, and B. A. Reynolds, “Isolation and Expansion of the Adult Mouse Neural Stem Cells Using the Neurosphere Assay,” p. 2010, 2010.

[58] Z. Mirzadeh, F. Doetsch, K. Sawamoto, H. Wichterle, and A. Alvarez-buylla, “The Subventricular Zone En-face : Wholemount Staining and Ependymal Flow,” no. May, pp. 1–8, 2010.

[59] F. H. Gage and S. Temple, “Neural stem cells: Generating and regenerating the brain,” *Neuron*, vol. 80, no. 3, pp. 588–601, 2013.

[60] J. B. Lennington, Z. Yang, and J. C. Conover, “Neural stem cells and the regulation of adult neurogenesis,” vol. 7, pp. 1–7, 2003.

[61] C. Wang *et al.*, “Identification and characterization of neuroblasts in the subventricular zone and rostral migratory stream of the adult human brain,” *Nat. Publ. Gr.*, vol. 21, no. 11, pp. 1534–1550, 2011.

[62] M. E. Van Strien, S. A. Van Den Berge, and E. M. Hol, “Migrating neuroblasts in the adult human brain : a stream reduced to a trickle,” *Nat. Publ. Gr.*, vol. 21, no. 11, pp. 1523–1525, 2011.

[63] Q. Shen *et al.*, “Article Adult SVZ Stem Cells Lie in a Vascular Niche : A Quantitative Analysis of Niche Cell-Cell Interactions,” pp. 289–300, 2008.

[64] E. H. Chang, I. Adorjan, M. V Mundim, B. Sun, and M. L. V Dizon, “Traumatic Brain Injury Activation of the Adult Subventricular Zone Neurogenic Niche,” vol. 10, no. August, 2016.

[65] C. C. Young, K. J. Brooks, A. M. Buchan, and F. G. Szele, “Cellular and Molecular Determinants of Stroke-Induced Changes in Subventricular Zone Cell Migration,” vol. 14, no. 10, 2011.

[66] M. E. Dailey, G. S. Marrs, and D. Kurpius, “Maintaining Live Cells and Tissue Slices in the Imaging Setup,” *Cold Spring Harb Protoc*, 2011.

[67] R. Fiorelli, K. Azim, B. Fischer, and O. Raineteau, “Adding a spatial dimension to postnatal ventricular-subventricular zone neurogenesis,” pp. 2109–2120, 2015.

[68] N. Kaneko *et al.*, “New Neurons Clear the Path of Astrocytic Processes for Their Rapid Migration in the Adult Brain,” vol. 67, no. 2, pp. 213–223, 2010.

[69] J. Khlghatyan and A. Saghatelyan, “Time-lapse Imaging of Neuroblast Migration in Acute Slices of the Adult Mouse Forebrain,” *J. Vis. Exp.*, no. 67, 2012.

[70] D. D. Wang, D. D. Krueger, and A. Bordey, “GABA depolarizes neuronal progenitors of the postnatal subventricular zone via GABA A receptor activation,” pp. 785–800, 2003.

[71] S. Preibisch, S. Saalfeld, and P. Tomancak, “Globally optimal stitching of tiled 3D microscopic image acquisitions,” *Bioinformatics*, vol. 25, no. 11, pp. 1463–1465, Jun. 2009.

[72] B. S. Meldrum, “Glutamate as a neurotransmitter in the brain: review of physiology and pathology,” *J. Nutr.*, vol. 130, no. 4S Suppl, p. 1007S–15S, 2000.

[73] Y. Zhou and N. C. Danbolt, “Glutamate as a neurotransmitter in the healthy brain,” *J. Neural Transm.*, vol. 121, no. 8, pp. 799–817, 2014.

[74] L. Birnbaumer *et al.*, “The naming of voltage-gated calcium channels,” *Neuron*, vol. 13, no. 3, pp. 505–6, Sep. 1994.

[75] N. C. Danbolt, “Glutamate uptake,” *Prog. Neurobiol.*, vol. 65, no. 1, pp. 1–105, Sep. 2001.

[76] R&D Systems, “Synaptic Neurotransmission Pathways: Glutamatergic Excitation.” [Online]. Available: https://www.rndsystems.com/pathways/synaptic-neurotransmission-pathways-glutamatergic-excitation. [Accessed: 12-Oct-2017].

[77] S. M. Robert and H. Sontheimer, “Glutamate Transporters in the Biology of Malignant Gliomas,” vol. 71, no. 10, pp. 1839–1854, 2014.

[78] R. J. Vandenberg and R. M. Ryan, “Mechanisms of Glutamate Transport,” *Physiol. Rev.*, vol. 93, no. 4, pp. 1621–1657, 2013.

[79] T. Storck, S. Schulte, K. Hofmann, and W. Stoffel, “Structure, expression, and functional analysis of a Na(+)-dependent glutamate/aspartate transporter from rat brain,” *Proc. Natl. Acad. Sci. U. S. A.*, vol. 89, no. 22, pp. 10955–9, 1992.

[80] G. Pines *et al.*, “Cloning and expression of a rat brain L-glutamate transporter,” *Nature*, vol. 360, no. 6403, pp. 464–467, Dec. 1992.

[81] Y. Kanai and M. A. Hediger, “Primary structure and functional characterization of a high-affinity glutamate transporter,” *Nature*, vol. 360, no. 6403, pp. 467–471, Dec. 1992.

[82] M. Flores-Méndez, O. G. Mendez-Flores, and A. Ortega, “Glia plasma membrane transporters: Key players in glutamatergic neurotransmission,” *Neurochem. Int.*, vol. 98, pp. 46–55, 2016.

[83] M. B. Robinson and J. G. Jackson, “Astroglial glutamate transporters coordinate excitatory signaling and brain energetics,” *Neurochem. Int.*, vol. 98, pp. 56–71, 2016.

[84] C. Grewer, N. Watzke, M. Wiessner, and T. Rauen, “Glutamate translocation of the neuronal glutamate transporter EAAC1 occurs within milliseconds,” *Proc. Natl. Acad. Sci. U. S. A.*, vol. 97, no. 17, pp. 9706–11, 2000.

[85] C. Mim, P. Balani, T. Rauen, and C. Grewer, “The glutamate transporter subtypes EAAT4 and EAATs 1-3 transport glutamate with dramatically different kinetics and voltage dependence but share a common uptake mechanism,” *J. Gen. Physiol.*, vol. 126, no. 6, pp. 571–89, 2005.

[86] J. S. Diamond and C. E. Jahr, “Transporters buffer synaptically released glutamate on a submillisecond time scale,” *J. Neurosci.*, vol. 17, no. 12, pp. 4672–4687, 1997.

[87] L. M. Levy, O. Warr, and D. Attwell, “Stoichiometry of the glial glutamate transporter GLT-1 expressed inducibly in a Chinese hamster ovary cell line selected for low endogenous Na+-dependent glutamate uptake,” *J. Neurosci.*, vol. 18, no. 23, pp. 9620–9628, 1998.

[88] C. Grewer and T. Rauen, “Electrogenic glutamate transporters in the CNS: Molecular mechanism, pre-steady-state kinetics, and their impact on synaptic signaling,” *J. Membr. Biol.*, vol. 203, no. 1, pp. 1–20, 2005.

[89] E. M. Rose, J. C. P. Koo, J. E. Antflick, S. M. Ahmed, S. Angers, and D. R. Hampson, “Glutamate transporter coupling to Na,K-ATPase,” *J. Neurosci.*, vol. 29, no. 25, pp. 8143–55, 2009.

[90] D. E. Bergles, A. V. Tzingounis, and C. E. Jahr, “Comparison of Coupled and Uncoupled Currents during Glutamate Uptake by GLT-1 Transporters,” *J. Neurosci.*, vol. 22, no. 23, pp. 10153–10162, 2002.

[91] W. H. Oldenziel, G. Dijkstra, T. I. F. H. Cremers, and B. H. . Westerink, “In vivo monitoring of extracellular glutamate in the brain with a microsensor,” *Brain Res.*, vol. 1118, no. 1, pp. 34–42, Nov. 2006.

[92] F. Pomerleau, B. K. Day, P. Huettl, J. J. Burmeister, and G. A. Gerhardt, “Real time in vivo measures of L-glutamate in the rat central nervous system using ceramic-based multisite microelectrode arrays,” *Ann. N. Y. Acad. Sci.*, vol. 1003, pp. 454–7, Nov. 2003.

[93] S. Tucci, P. Rada, M. J. Sepúlveda, and L. Hernandez, “Glutamate measured by 6-s resolution brain microdialysis: capillary electrophoretic and laser-induced fluorescence detection application,” *J. Chromatogr. B. Biomed. Sci. Appl.*, vol. 694, no. 2, pp. 343–9, Jul. 1997.

[94] A. Belay, A. Collins, T. Ruzgas, P. T. Kissinger, L. Gorton, and E. Csöregi, “Redox hydrogel based bienzyme electrode for L-glutamate monitoring,” *J. Pharm. Biomed. Anal.*, vol. 19, no. 1–2, pp. 93–105, Feb. 1999.

[95] E. Mikeladze *et al.*, “Redox Hydrogel-Based Bienzyme Microelectrodes for Amperometric Monitoring ofL-Glutamate,” *Electroanalysis*, vol. 14, no. 6, pp. 393–399, Mar. 2002.

[96] B. Westerink and J. J. Justice, “Microdialysis compared with other in vivo release models,” in *Microdialysis in the Neurosciences: Techniques in the Behavioral and Neural Sciences*, vol. 7, T. Robinson and J. Justice, Eds. Elsevier, 1991, pp. 23–43.

[97] U. Ungerstedt, “Introduction to intracerebral microdialysis,” in *Microdialysis in the Neurosciences: Techniques in the Behavioral and Neural Sciences*, vol. 7, Elsevier, 1991, pp. 3–22.

[98] J. Georgieva, J. Luthman, B. Mohringe, and O. Magnusson, “Tissue and microdialysate changes after repeated and permanent probe implantation in the striatum of freely moving rats,” *Brain Res. Bull.*, vol. 31, no. 5, pp. 463–470, Jan. 1993.

[99] L. M. Borland and A. C. Michael, “An Introduction to Electrochemical Methods in Neuroscience,” in *Electrochemical Methods for Neuroscience*, 2007.

[100] P. T. Kissinger, J. B. Hart, and R. N. Adams, “Voltammetry in brain tissue--a new neurophysiological measurement.,” *Brain Res.*, vol. 55, no. 1, pp. 209–13, May 1973.

[101] M. L. Huffman and B. J. Venton, “Carbon-Fiber Microelectrodes for In Vivo Applications,” *Analyst.*, vol. 134, no. 1, pp. 18–24, 2010.

[102] E. R. Hascup *et al.*, “Histological studies of the effects of chronic implantation of ceramic-based microelectrode arrays and microdialysis probes in rat prefrontal cortex.,” *Brain Res.*, vol. 1291, pp. 12–20, Sep. 2009.

[103] R. F. Vreeland *et al.*, “Biocompatible PEDOT:Nafion composite electrode coatings for selective detection of neurotransmitters in vivo,” *Anal. Chem.*, vol. 87, no. 5, pp. 2600–2607, 2015.

[104] J. J. Burmeister and G. A. Gerhardt, “Self-referencing ceramic-based multisite microelectrodes for the detection and elimination of interferences from the measurement of L-glutamate and other analytes,” *Anal. Chem.*, vol. 73, no. 5, pp. 1037–1042, 2001.

[105] K. D. Wise, J. B. Angell, and A. Starr, “An Integrated-Circuit Approach to Extracellular Microelectrodes,” *IEEE Trans. Biomed. Eng.*, vol. BME-17, no. 3, pp. 238–247, 1970.

[106] J. J. Burmeister, K. Moxon, and G. A. Gerhardt, “Ceramic-based multisite microelectrodes for electrochemical recordings,” *Anal. Chem.*, vol. 72, no. 1, pp. 187–192, 2000.

[107] F. Fonnum, “Glutamate: a neurotransmitter in mammalian brain,” *J. Neurochem.*, vol. 42, no. 1, pp. 1–11, Jan. 1984.

[108] M. J. During and D. D. Spencer, “Extracellular hippocampal glutamate and spontaneous seizure in the conscious human brain,” *Lancet*, vol. 341, no. 8861, pp. 1607–1610, Jun. 1993.

[109] K. Tanaka *et al.*, “Epilepsy and Exacerbation of Brain Injury in Mice Lacking the Glutamate Transporter GLT-1,” *Science*, vol. 276, no. 5319, pp. 1699–1702, 1997.

[110] A. S. Bryant, B. Li, M. P. Beenhakker, and J. R. Huguenard, “Maintenance of thalamic epileptiform activity depends on the astrocytic glutamate-glutamine cycle,” *J. Neurophysiol.*, vol. 102, no. 5, pp. 2880–8, 2009.

[111] Z. C. Ye, J. D. Rothstein, and H. Sontheimer, “Compromised glutamate transport in human glioma cells: reduction-mislocalization of sodium-dependent glutamate transporters and enhanced activity of cystine-glutamate exchange,” *J. Neurosci.*, vol. 19, no. 24, pp. 10767–77, 1999.

[112] CenMeT Service Center, “Ceramic Based - Microelectrode Arrays - R1.” [Online]. Available: http://www.ukycenmet.com/r1/. [Accessed: 18-Nov-2017].

[113] H. Zhang, S. C. Lin, and M. A. L. Nicolelis, “Acquiring local field potential information from amperometric neurochemical recordings,” *J. Neurosci. Methods*, vol. 179, no. 2, pp. 191–200, 2009.

[114] E. M. Miller, J. E. Quintero, and F. Pomerleau, “Simultaneous glutamate recordings in the frontal cortex network with multisite biomorphic microelectrodes: New tools for ADHD research,” *J. Neurosci. Methods*, vol. 252, pp. 75–79, Aug. 2015.

[115] A. Weltin, J. Kjenjinger, and B. Enderle, “Polymer-based, flexible glutamate and lactate microsensors for in vivo applications,” *Biosens. Bioelectron.*, vol. 61, pp. 192–199, Nov. 2014.

[116] R. E. Ozel, C. Ispas, M. Ganesana, J. C. Leiter, and S. Andreescu, “Glutamate oxidase biosensor based on mixed ceria and titania nanoparticles for the detetion of glutamate in hypoxic environments,” *Biosens. Bioelectron.*, vol. 52, no. 3, pp. 397–402, 2014.

[117] L. C. Daws and G. M. Toney, “High-Speed Chronoamperometry to Study Kinetics and Mechanisms for Serotonin Clearance In Vivo,” in *Electrochemical Methods for Neuroscience*, A. C. Michael and L. M. Borland, Eds. CRC Press/Taylor & Francis, pp. 63–82, 2007.

[118] J. M. Pearce, “Return on investment for open source scientific hardware development,” *Sci. Public Policy*, vol. 43, no. 2, pp. 192–195, 2016.

[119] M. Coakley and D. E. Hurt, “3D Printing in the Laboratory: Maximize Time and Funds with Customized and Open-Source Labware,” *J. Lab. Autom.*, vol. 21, no. 4, pp. 489–495, 2016.

[120] “Orbital Shaker | NIH 3D Print Exchange.” [Online]. Available: https://3dprint.nih.gov/discover/3dpx-000684. [Accessed: 22-Dec-2017].

[121] A. M. S. Ibrahim, R. R. Jose, A. N. Rabie, T. L. Gerstle, B. T. Lee, and S. J. Lin, “Three-dimensional Printing in Developing Countries,” *Plast. Reconstr. Surg. Glob. Open*, vol. 3, no. 7, p. e443, 2015.

[122] “How a Medical Clinic in the Bolivian Rainforest Might Use 3D Printing.” [Online]. Available: https://3dprintingindustry.com/news/medical-clinic-bolivian-rainforest-might-use-3d-printing-23735/. [Accessed: 22-Dec-2017].

[123] T. Baden, A. M. Chagas, G. Gage, T. Marzullo, L. L. Prieto-Godino, and T. Euler, “Open Labware: 3-D Printing Your Own Lab Equipment,” *PLoS Biol.*, vol. 13, no. 3, pp. 1–12, 2015.

[124] S. Tual-Chalot, K. R. Allinson, M. Fruttiger, and H. M. Arthur, “Whole Mount Immunofluorescent Staining of the Neonatal Mouse Retina to Investigate Angiogenesis,” *J. Vis. Exp.*, no. 77, pp. 6–11, 2013.

[125] A. Sargoy, S. Barnes, N. C. Brecha, and L. Perez De Sevilla Muller, "Immunohistochemical and Calcium Imaging Methods in Wholemount Rat Retina," *J. Vis. Exp.*, no. 92, p. e51396, 2014.

[126] E. Ivanova, A. H. Toychiev, C. W. Yee, and B. T. Sagdullaev, "Optimized Protocol for Retinal Wholemount Preparation for Imaging and Immunohistochemistry," *J. Vis. Exp.*, no. 82, pp. 1–7, 2013.

[127] M. P. Parsons, M. P. Vanni, C. L. Woodard, R. Kang, T. H. Murphy, and L. A. Raymond, "Real-time imaging of glutamate clearance reveals normal striatal uptake in Huntington disease mouse models," *Nat. Commun.*, vol. 7, p. 11251, 2016.

[128] Beckman Coulter, "CytoFLEX Features." [Online]. Available: https://www.beckman.com/coulter-flow-cytometers/cytoflex/features. [Accessed: 26-Oct-2017].

[129] Abcam, "Introduction to Flow Cytometry," 2014.

[130] Expert Cytometry, "12 Flow Cytometry Terms And Definitions Most Scientists Get Wrong." [Online]. Available: https://expertcytometry.com/12-flow-cytometry-terms-and-definitions-most-scientists-get-wrong/. [Accessed: 26-Oct-2017].